ABSTRACT

Electro-magnetic Physics Studies at RHIC:
Neutral Pion Production, Direct Photon HBT, Photon Elliptic Flow in Au+Au Collisions at $\sqrt{s_{NN}} = 200$ GeV and the Muon Telescope Detector Simulation

Guoji Lin
Yale University
December 2009

Electro-magnetic (E&M) probes such as direct photons and muons (μ) are important tools to study the properties of the extremely hot and dense matter created in heavy ion collisions at the Relativistic Heavy Ion Collider (RHIC). In this thesis, several topics of E&M physics will be addressed, including neutral pion (π^0) production, direct photon HBT, and photon elliptic flow (v_2) in Au+Au collisions at $\sqrt{s_{NN}} = 200$ GeV. A discussion on the simulation study of the new Muon Telescope Detector (MTD) will also be presented.

The π^0 production is a fundamental measurement of hadron production and prerequisite for the background study of direct photons. Neutral pions are reconstructed using the photons detected by the STAR Barrel Electro-magnetic Calorimeter (BEMC) and the Time Projection Chamber (TPC). Spectra of π^0 are measured at transverse momentum $1 < p_T < 12$ GeV/c near mid-rapidity ($0 < \eta < 0.8$) in 200 GeV Au+Au collisions. The spectra and nuclear modification factors R_{CP} and R_{AA} are compared to earlier $\pi^{\pm}$ and π^0 results.

Direct photon Hanbury-Brown and Twiss (HBT) correlations can reveal information of the system size throughout the whole collision. A first attempt of direct photon HBT study at RHIC in 200 GeV Au+Au collisions is done using photons detected by the STAR BEMC and TPC. An unknown correlation at small Q_{inv} is observed, whose magnitude is much larger than the expected HBT signal, and possible causes of the correlation will be discussed.

Direct photon elliptic flow (v_2) at intermediate to high p_T is sensitive to the source of direct photon production. Results of inclusive photon v_2 in 200 GeV Au+Au collisions are presented. The v_2 of π^0 decay photons is calculated from the previously published π results. The comparison between inclusive and decay photon v_2 indicates that direct photon v_2 is small.

A new large-area Muon Telescope Detector at mid-rapidity at RHIC is proposed and under investigation, using the Long-strip Multi-Gap Resistive Plate Chamber (Long-MRPC). Simulations indicate that the MTD can effectively identify μ and reject hadron backgrounds, and it can serve as a μ trigger. A beam test result of the Long-MRPC at Fermi National Accelerator Laboratory (FNAL) is also discussed.

Electro-magnetic Physics Studies at RHIC: Neutral Pion Production, Direct Photon HBT, Photon Elliptic Flow in Au+Au Collisions at $\sqrt{s_{NN}} = 200$ GeV and the Muon Telescope Detector Simulation

A Dissertation
Presented to the Faculty of the Graduate School
of
Yale University
in Candidacy for the Degree of
Doctor of Philosophy

By
Guoji Lin

Dissertation Director: Prof. Jack Sandweiss

December 2009

Acknowledgements

First of all I would like to thank my advisor, Prof. Jack Sandweiss. I have learned so much from Jack's lectures in Electromagnetic Theory and Classical Field Theory, and received countless help from him during his five year's supervision in my Ph.D. research. His tremendous knowledge and enormous enthusiasm for physics deeply impress me. He presents me the professional attitude and responsibility which I should always follow in my future career.

All my group members deserve my most sincere acknowledgment. Special thanks are given to Evan Finch, who carefully went over my thesis and made all the corrections. I truly enjoy the fruitful discussions and valuable working experience with Alexei Chikanian, Evan Finch, Richard Majka, graduate student Ke Han, and former member Fei Du. I also would like to thank Rochelle Lauer for setting up the computer system, and secretaries Lillian Vinston, Teena Marie Griggs, and Carole DeVore for their help.

I am expressing my gratitude to all members of the STAR Collaboration and the T963 beam test. I sincerely thank Haibin Zhang who helped me start my research at RHIC, Zhangbu Xu and Aihong Tang who guided me in different research projects. I will never forget the remarkable collaboration with Marco van Leeuwen, Lijuan Ruan, Bedanga Mohanty, and many others in the former HBT, EbyE, high-pT, spectra, and computing groups. I highly appreciate your help and advice.

I would like to thank the members of my thesis committee, Prof. Helen Caines, Prof. David DeMille, Prof. John Harris, Prof. Jack Sandweiss, Prof. Witold Skiba, and my outside reader Prof. Thomas Ullrich at Brookhaven National Laboratory for their careful reading and important corrections.

I would like to thank my beloved parents and Xiao Pan for their support in both my research and life. It was impossible for me to overcome so many difficulties without them. I would like to share the excitement of graduation with all my friends, especially those at Yale who have brought so much fun to my life in New Haven.

Thank you very much for all your help and support.

Contents

Acknowledgements **iii**

1 Introduction **1**

1.1 QGP from Heavy Ion Collisions 1

1.1.1 QGP phase transition 1

1.1.2 Relativistic heavy-ion collisions 4

1.1.3 Glauber model 5

1.2 QGP signatures in Heavy Ion Collision 9

1.2.1 Jet quenching for light quarks 9

1.2.2 Direct photon HBT 12

1.2.3 Direct photon elliptic flow 17

1.2.4 Muon probes 23

2 STAR Experiment **27**

2.1 RHIC 27

2.2 STAR 30

2.2.1 Overview 30

2.2.2 Trigger system 32

2.2.3 Time Projection Chamber 34

2.2.4 Forward TPC 39

2.2.5 Barrel Electromagnetic Calorimeter 41

3 Neutral Pion Production **45**

3.1 Neutral pion reconstruction techniques 45

3.1.1 Data set . . . 45
3.1.2 BEMC photon reconstruction . . . 49
3.1.3 TPC conversion photon reconstruction . . . 51
3.1.4 Di-photon invariant mass . . . 55
3.1.5 Prescale factor . . . 60
3.2 Efficiency calculation . . . 63
3.2.1 Embedding procedure . . . 63
3.2.2 Geometry correction . . . 67
3.2.3 BEMC acceptance correction . . . 71
3.2.4 Efficiency . . . 72
3.3 Systematic errors . . . 74
3.3.1 Cut study . . . 74
3.3.2 Yield extraction . . . 75
3.3.3 BEMC energy scale . . . 76
3.3.4 Geometry correction . . . 79
3.3.5 Summary of systematic errors . . . 80
3.4 Results . . . 81
3.4.1 STAR π^0 spectra . . . 81
3.4.2 Nuclear modification factors R_{CP} and R_{AA} . . . 83
3.4.3 Future analysis with run7 data . . . 87
3.4.4 Summary . . . 87

4 Direct Photon HBT **89**
4.1 Photon reconstruction techniques . . . 89
4.1.1 Data set . . . 89
4.1.2 Photon reconstruction . . . 90
4.1.3 Photon HBT correlation function . . . 90
4.2 Results . . . 92
4.2.1 Photon Q_{inv} correlation function . . . 92
4.2.2 Study of the low Q_{inv} peak . . . 93
4.2.3 Summary . . . 97

4.3 Future upgrades . . . 99
4.3.1 DAQ Upgrade . . . 99
4.3.2 Photon converter . . . 99
4.3.3 Shashlyk calorimeter . . . 101
4.3.4 Simulation results . . . 102

5 Photon Elliptic Flow **104**
5.1 Photon v_2 measurement techniques . . . 104
5.1.1 Data set . . . 104
5.1.2 Photon reconstruction . . . 105
5.1.3 Event plane measurement from TPC and FTPC . . . 105
5.1.4 Scalar product method . . . 107
5.1.5 v_2 correction for charged particle veto cut . . . 112
5.2 Decay photon v_2 . . . 115
5.2.1 STAR BEMC's response to high-p_T π^0 . . . 115
5.2.2 Decay photon v_2 from π^0 embedding . . . 117
5.2.3 Other backgrounds . . . 120
5.3 Results . . . 122
5.3.1 Inclusive photon v_2 . . . 122
5.3.2 Decay photon v_2 . . . 123
5.3.3 Decay photon spectrum . . . 126
5.3.4 Summary . . . 128

6 Muon Telescope Detector **129**
6.1 MTD simulation . . . 129
6.1.1 MTD geometry . . . 129
6.1.2 Muon identification and hadron rejection . . . 130
6.1.3 Muon and high-p_T hadron trigger . . . 137
6.1.4 Upsilon Simulation . . . 140
6.2 Long-MRPC beam test at FNAL . . . 143
6.2.1 Long-MRPC . . . 143
6.2.2 Beam test setup . . . 144

6.2.3 Beam test results 146
6.2.4 Summary 155

Bibliography **157**

List of Tables

3.1 The definition of different centrality bins in 200 GeV Au+Au collisions with their reference multiplicity ranges and N_{bin} calculated in the Glauber model. 46
3.2 Cuts used to select e^+/e^- tracks and photon candidates. 53
3.3 Ratio of BEMC acceptance between embedding and real data in BEMC tower, SMD η, and SMD ϕ strips in different data samples. 72
3.4 Variation of TPC photon reconstruction cuts used to evaluate systematic uncertainty of π^0 spectra. 74
3.5 Summary of major sources of systematic uncertainties on the π^0 yields in 200 GeV Au+Au collisions. 80
4.1 Number of central Au+Au events required to perform a 3-D HBT analysis in different p_T ranges. 103
5.1 Cuts used to select TPC and FTPC charged tracks for event plane calculation. 107
6.1 The number of MTD hits per central Au+Au HIJING event when using different online muon trigger requirements. 139
6.2 The comparison between MRPC modules used in the TOF and MTD. 144
6.3 Performance tests on two Long-MRPC modules at FNAL. 146

List of Figures

1.1 Summary of the QCD running coupling constant α_s as a function of the energy scale Q where the measurement was carried out, compared to the lattice QCD calculation. 3

1.2 Lattice QCD calculation results for the pressure (left) and energy density (right) divided by T^4 of strongly interacting matter as a function of temperature. 4

1.3 Schematic QCD phase diagram in chemical potential and temperature. 4

1.4 A schematic picture of the evolution of a relativistic heavy ion collision. 6

1.5 Schematic representation of the optical Glauber model geometry, with transverse (a) and longitudinal (b) views. 6

1.6 p_T dependence of nuclear modification factors R_{AA} and R_{CP} of hadrons in Au+Au collisions at $\sqrt{s_{NN}}$=200 and 62.4 GeV. Data are compared to calculations from radiative and collisional energy loss scenarios. [15] 11

1.7 Di-hadron azimuthal correlations at high p_T in p+p, central d+Au and central Au+Au collisions (background subtracted) from STAR. 12

1.8 Integrated photon emission spectra from central Au+Au collisions at RHIC [24]. 13

1.9 Schematic view of an intensity interference experiment using two detectors in electronic coincidence. 14

1.10 The two-photon correlation function with average photon momenta 100< K_T <200 MeV/c (top) and 200< K_T <300 MeV/c (bottom) fitted with a Gaussian source shape from the WA98 Collaboration at SPS energy [34]. 17

1.11 Schematic view of two nuclei colliding with impact parameter b. . . . 18
1.12 v_2 vs. p_T for identified particles from minimum bias Au+Au collisions at RHIC compared to hydro calculations. 19
1.13 Identified particle v_2 scaled by the number of constituent quarks (n) from minimum bias Au+Au collisions. Bottom panel is the ratio of v_2/n to the fitted curve. 20
1.14 Direct photon v_2 as a function of p_T for Au+Au collisions at RHIC considering photons from jets. The dotted lines show v_2 for primary hard photons and jet fragmentation only; the solid and dashed lines show all direct photons with and without energy loss of jets taken into account. 21
1.15 $v_2(p_T)$ for thermal photons from off-central 200 GeV Au+Au collisions at b=7 fm (red solid curve). Quark (blue dotted curve) and hadronic matter (red dashed curve) contributions are shown separately, and the v_2 of π (upper blue solid curve) and ρ (lower blue solid curve) mesons are shown for comparison. 22
1.16 PHENIX direct photon v_2 as a function of p_T in minimum bias Au+Au collisions at $\sqrt{s_{NN}}$=200 GeV. Proton and π^0 v_2 are plotted for comparison. 23
1.17 Opposite-sign di-muon invariant mass spectrum in Pb-Pb collisions at 158 GeV/nucleon. The lines are fit results of different components. . 24
1.18 Schematic depiction of the relative flux of different components of the inclusive muon candidate yield as a function of flight path into the PHENIX muon arm absorber. [51] 25
1.19 Left: Mass squared distribution $m^2 = (p/\beta/\gamma)^2$ from the Time-of-Flight (TOF) detector. Right: p_T distributions of invariant yields for D^0, charm-decayed prompt μ and non-photonic electron in different centralities of 200 GeV Au+Au collisions. Solid curves are power-law combined fit for D^0 and leptons. Dashed curves are blast-wave fit. The gray bands are bin-to-bin systematic uncertainties. 26
2.1 The RHIC accelerator complex. 28

2.2 Perspective view of the STAR detector, with a cutaway for viewing inner detector systems. 30
2.3 Cutaway side view of the STAR detector as configured in 2004. . . . 31
2.4 Correlation between the summed pulse heights from the ZDC and the CTB for events with a primary collision vertex successfully reconstructed from tracks in the TPC. 33
2.5 The schematic overview of the STAR TPC. 35
2.6 The anode pad plane with one full sector shown. The inner subsector is on the right and it has small pads arranged in widely spaced rows. The outer subsector is on the left and it is densely packed with larger pads. 35
2.7 The pion tracking efficiency in STAR for Au+Au events at $\sqrt{s_{NN}}$ = 130 GeV at RHIC. Tracks with $|y|$ <0.7 are used and the magnetic field is set to 0.25 T. 37
2.8 The energy loss per unit length distribution for primary and secondary particles in the STAR TPC as a function of primary momentum. The magnetic field is 0.25 T. 38
2.9 Schematic diagram of an FTPC for the STAR experiment. 40
2.10 Side view of a calorimeter module showing the projective nature of the towers. 41
2.11 Side view of a STAR BEMC tower. The location of the two layers of shower maximum detector at a depth of approximately $5X_0$ from the front face at η=0 is also shown. 42
2.12 Schematic illustration of the double layer STAR BEMC SMD. 43
3.1 The uncorrected reference multiplicity distribution for MB, central, and HT triggered Au+Au collision at $\sqrt{s_{NN}}$=200 GeV. The three centrality regions used in this analysis are shown. 47
3.2 The vertex position distribution in z axis after the event cut from MB Au+Au collisions at $\sqrt{s_{NN}}$=200 GeV. 47
3.3 The distribution of the ratio of $R = \frac{E_{BEMC}}{E_{BEMC}+E_{TPC}}$ in 200 GeV Au+Au collisions. 48

3.4 The distribution of towers as a function of η in the BEMC with photon p_T >5 GeV/c and $3 < p_T < 5$ GeV/c. Beam background contamination can be seen at $\eta \sim 1$. 48
3.5 Energy distribution of towers with different numbers of tracks intersected inside the BEMC but not directly hit by any track. 50
3.6 Photon conversion probability vs. p_T from simulation. 52
3.7 Schematic view of a photon conversion in the xy-plane and rz-plane. Figure is taken from Ref. [64]. 52
3.8 Left: Conversion point spatial distribution inside the STAR detector. Right: Conversion point radial distribution. 55
3.9 Left: Di-photon same- and mixed-event distributions normalized in the region of [0.5, 1.0] GeV/c^2. Right: Ratio of same- over mixed-event distributions. 56
3.10 π^0 invariant mass distribution in 0-20% Au+Au collisions at $\sqrt{s_{NN}}$ = 200 GeV. (a) EMC-TPC method in MB events at $1.2 < p_T < 1.5$ GeV/c; (b) EMC-TPC method in MB events at $3.5 < p_T < 5$ GeV/c; (c) EMC-TPC method in HT events at $7 < p_T < 9$ GeV/c; (d) EMC-EMC method in HT events at $9 < p_T < 12$ GeV/c. Solid lines are fit results of a Gaussian peak plus a 3rd order polynomial (panel a and b) or linear (panel c and d) background function. The residual backgrounds are shown as dotted lines. 58
3.11 π^0 invariant mass peak position and peak width as a function of p_T in 0-80% 200 GeV Au+Au collisions. The results from π^0 embedded simulation are also shown for comparison. The dotted line is the π^0 mass value from PDG. The legends apply for both figures. 60
3.12 The number of equivalent MB events for one HT event in different centralities in Au+Au 200 GeV collisions. A larger number on the x axis represents more central collisions. 62
3.13 Left: Reference multiplicity distribution of embedding data before weighting. Right: Reference multiplicity distribution of embedding data after weighting. 64

3.14 Left: p_T distribution of input MC π^0's. Right: p_T distribution of MC π^0's after weighting is shown as a curve. The PHENIX π^0 spectrum is shown as data points for comparison. 64
3.15 Left: η (left) and ϕ (right) distributions of MC π^0 and reconstructed EMC photons. 65
3.16 Left: $\frac{N_{fit}}{N_{poss}}$ distributions in e^+/e^- selection from data and embedding. Right: Dip angle difference α_{dip} in TPC photon selection from data and embedding. Distributions from embedding show reconstructed tracks with associated MC counterparts, and with spectra weighting applied as mentioned above. 65
3.17 Reconstructed π^0 signal in embedding data analysis from EMC-TPC method in MB events (left) and from EMC-EMC method in HT events (right). Each reconstructed π^0 can be associated with a MC π^0. Results from Gaussian fit are also shown. 66
3.18 Photon conversion radius distributions from real data and MC simulation in 200 GeV Au+Au collisions. Two distributions are normalized in the TPC gas region at $60 < r < 100$ cm. 68
3.19 Left: z coordinate distributions of conversions in the SVT area ($10 < r < 20$ cm) from data and simulation, after normalization in the TPC gas area ($60 < r < 100$ cm). Right: Ratio of combined simulation over data result in the left panel. 69
3.20 Left: z coordinate distributions of conversions in the SSD area ($20 < r < 40$ cm) from data and simulation, after normalization in the TPC gas area ($60 < r < 100$ cm). Right: Ratio of combined simulation over data result in the left panel. 69
3.21 Conversion probability correction factor for TPC photons (left) and π^0's (right) as a function of p_T. 70
3.22 Event-averaged energy deposited in BEMC towers in different days of run. The "SoftId" is STAR's internal label for each BEMC tower. . . 71

3.23 Event-averaged energy deposited in SMD η (left) and ϕ (right) strips in different days of run. The "SoftId" is STAR's internal label for each SMD strip. 72
3.24 Total π^0 detection efficiency for three methods as a function of p_T in different centrality bins in 200 GeV Au+Au collisions. 73
3.25 Ratio of π^0 spectra from tight/loose TPC photon reconstruction cuts over original cuts for different centrality bins using EMC-TPC method in MB (left) and HT (right) event samples. 75
3.26 Change of π^0 spectra from varied EMC photon reconstruction cuts and original cuts for different centrality bins in MB (left) and HT (right) event samples. 76
3.27 Change of π^0 spectra from different fit ranges for different centrality bins in MB (left) and HT (right) event samples. 77
3.28 Change of π^0 spectra from different fit functions (3rd order polynomial vs. linear function) for different centrality bins in MB event samples. 77
3.29 Change of π^0 spectra from different normalization factors used in mixed-event background subtraction for different centrality bins in MB (left) and HT (right) event samples. The bin-by-bin normalization is discussed in section 3.1.4. In HT events, the same-event di-photon invariant mass distribution is fit either with or without the mixed-event background subtracted. 78
3.30 Change of π^0 spectra from different BEMC energy scale offsets for different centrality bins in MB (left) and HT (right) event samples. . 78
3.31 Geometry correction factor as a function of conversion radius applied in the embedding analysis. 79
3.32 Change of π^0 spectra from different geometry correction methods for different centrality bins in MB (left) and HT (right) event samples. . 80

3.33 Invariant yield distribution of STAR π^0 as a function of p_T at mid-rapidity for different centrality bins in 200 GeV Au+Au collisions. Spectra for different centralities are scaled for clarity. Statistical errors are shown as vertical lines and point to point systematic errors are shown as bars. 82
3.34 The ratio of STAR charged π (left) and PHENIX π^0 spectra over their fitting results for different centrality bins. 83
3.35 The ratios of STAR π^0 spectra over $\pi^{\pm}$ from STAR [71] (solid dot) and π^0 from PHENIX [16] (open cross) as a function of p_T for different centrality bins in 200 GeV Au+Au collisions. Statistical errors are shown as vertical lines and point to point systematic errors are shown as bands. 84
3.36 The nuclear modification factor R_{CP} as a function of p_T of STAR π^0 compared to STAR $\pi^{\pm}$ [71] in 200 GeV Au+Au collisions. Statistical errors are shown as vertical lines and point to point systematic errors are shown as horizontal lines. The shaded band on the right demonstrates the uncertainty of N_{bin}. The solid curves are jet quenching theoretical calculation [72]. 85
3.37 The nuclear modification factor R_{AA} as a function of p_T of STAR π^0 compared to PHENIX π^0 [16] in 200 GeV Au+Au collisions. Statistical errors are shown as vertical lines and point to point systematic errors are shown as horizontal lines. The shaded band on the right demonstrates the uncertainties of N_{bin} and the normalization error in p+p collisions. The solid curves are theoretical calculations in 0-10% Au+Au collisions [74]. 86
3.38 π^0 invariant mass distributions using 200 GeV Au+Au data in run7 express stream data sample for EMC-TPC (left) and EMC-EMC (right) methods. 88
4.1 The photon HBT correlation function using EMC-TPC photon pairs in 200 GeV Au+Au collisions. 92

4.2 The photon HBT correlation function using TPC-TPC photon pairs in 200 GeV Au+Au collisions. 93
4.3 Left: The TPC photon energy distribution in different Q_{inv} regions for the same- and mixed-event photon pairs. Right: The ratios of the energy distributions. 94
4.4 Left: The EMC photon energy distribution in different Q_{inv} regions for the same- and mixed-event photon pairs. Right: The ratios of the energy distributions. 94
4.5 The ratio of the opening angle distributions of the same-event over the mixed-event photon pairs in different Q_{inv} regions. 95
4.6 The photon HBT correlation functions using EMC (left) and TPC (right) photons from different energy ranges. 95
4.7 Photon HBT correlation function when using TPC photons with different decay lengths. 96
4.8 Photon HBT correlation function when only using TPC photons converted at the inner field cage. 97
4.9 Layout of the photon converter and an example of photon converting at the converter. 100
4.10 TPC conversion photon detection efficiency as a function of photon energy and incident angle (upper left). TPC photon reconstructed angular resolution as a function of photon energy and incident angle (lower left). TPC photon reconstructed energy resolution in different photon energy ranges (right). 101
4.11 Expected 1-D HBT correlation function for photons as a function of Q_{osl} for 50×10^6 central Au+Au events. The black histogram is the same simulation done with HBT turned off. 102
5.1 The comparison of four terms of charged particle v_2 using Q-vectors calculated from FTPC tracks. 109
5.2 The comparison of charged particle v_2 from FTPC method to v_2 from two- and four-particle cumulant methods in different centralities bins. 110

5.3 Azimuthal correlations in Au+Au collisions as a function of centrality compared to minimum bias azimuthal correlations in p+p collisions [80]. 111
5.4 Azimuthal correlations between inclusive photons and charged particles in the TPC in 40-50% Au+Au and MB p+p collisions as a function of p_T. 113
5.5 Left: The comparison of photon v_2 after applying the charged particle veto cut to the input v_2 in simulation. Their difference is also shown. Right: the average v_2 correction for the charged particle veto cut as a function of centrality in Au+Au collisions. Here a larger number in the x axis represents more central collisions. 114
5.6 Ratio of reconstructed photon p_T over MC photon p_T (left) and π^0 p_T (right) for two photon reconstruction algorithms. 115
5.7 The $\pi^{\pm}$ v_2 measured by the FTPC method in different centralities in 200 GeV Au+Au collisions. The solid curves are fitting results. 118
5.8 Inclusive photon v_2 as a function of p_T for centrality 20-60% and 5-20% in 200 GeV Au+Au collisions. Results from two photon reconstruction algorithms and two v_2 calculating methods are shown for comparison. Only statistical errors are shown. 122
5.9 Decay photon v_2 as a function of p_T in different centrality bins using two photon identification algorithms, compared to the input π^0 v_2. Here only the v_2 values are shown without any error bars. 123
5.10 The π^0 decay photon v_2 as a function of p_T using both photon identification algorithms in centrality bins of 20-60% and 5-20%. The inclusive photon v_2 is shown for comparison. Only statistical errors are shown. 125
5.11 The π^0 decay photon spectra in different centralities compared to the inclusive photon spectra from the cluster algorithm. 126
5.12 The π^0 decay photon spectra in different centralities compared to the inclusive photon spectra from the single tower algorithm. 127
6.1 The schematic view of the MTD geometry. The MTD is shown as a blue layer outside the magnet return bars. 130

6.2 Examples of 5 MC muons (left) and pions (right) generated with $2 < p_T < 5$ GeV/c and propagated through the STAR detectors in GEANT. 131
6.3 Efficiency of reconstructing muons (left) and pions (right) at the MTD as a function of p_T requiring only one hit on the MTD. 132
6.4 MTD hit distribution with respect to the layer center in the azimuthal direction in pion simulations. 132
6.5 The DCA vs. MC track p_T distributions for muons (left) and pions (right). 133
6.6 The most probable DCA and the width of the DCA distribution for muons as a function of p_T 134
6.7 TOF difference between MC tracks and the MTD hits for muons (left) and pions (right). 134
6.8 Energy loss of muons (left) and pions (right) in the MTD. 135
6.9 The detection efficiencies for muons and hadrons in the MTD. 136
6.10 The detection efficiencies for pions in the MTD at $2 < p_T < 5$ GeV/c. MTD hits from primary pions and decay muons are also presented. . 136
6.11 An example of a central HIJING event propagated in GEANT (left) in STAR and the p_T distribution of the charged tracks in 100 HIJING events (right). 138
6.12 The detection efficiency for pions in the MTD as a function of p_T after requiring $TOF < 20$ ns. 139
6.13 Di-muon invariant mass distribution assuming a nominal TPC primary track momentum resolution of $\delta p/p = 0.0087 + 0.0045p$, and a ratio of 1S:2S:3S=9:1.8:1 for 3 states of Υ from CDF. 140
6.14 Di-muon invariant mass distributions at different p_T ranges from Υ simulation. The lower right figure shows the Υ invariant mass peaks using the fitting results (gaussian peak positions and widths) at $0 < p_T < 5$ GeV/c, and the ratio of states used in the toy model. 142
6.15 Schematic layout of a Long-MRPC module. 143
6.16 Experiment setup of the Long-MRPC beam test at FNAL. 145

6.17 The ADC (upper panels) and TDC (lower panels) signal distributions from two Long-MRPC modules. For TDC it is 50 ps/channel. 147
6.18 The ADC distribution of the Tsinghua module after using 7% SF_6 as working gas. 148
6.19 The efficiency of two Long-MRPC modules as a function of strength of electric field inside the modules. Both trigger methods using the scintillator and the other module are used. 149
6.20 Timing resolution of both Long-MRPC modules as a function of strength of electric field. 151
6.21 The correlation between the Long-MRPC two-end TDC difference and the beam position from the GEM chamber (left) and MWPC (right) for the Tsinghua module. 151
6.22 The correlation between the peak of Long-MRPC two-end TDC difference distribution and the beam position from the GEM chamber (left) and MWPC (right) for the Tsinghua module. The straight line is a linear fit. 152
6.23 The distribution of the difference between the beam position calculated from the ΔTDC of the Long-MRPC and the position given by the GEM chamber (left) and the MWPC (right) for the Tsinghua module. The curve is a gaussian fitting. 153
6.24 The width of ΔTDC distribution as a function of beam incident position provided by the GEM chamber (left), and the MWPC (right) for the USTC module. A constant number fit is shown as the solid lines. 154
6.25 The correlation between the peak of Long-MRPC two-end TDC difference distribution and the beam position from the MWPC for the USTC module. The left panel is for incident angle of 0° and the right panel for 32.8°. The straight line is a linear fit to the data. 154
6.26 The time-of-flight distribution of proton rich sample for the Tsinghua (left) and USTC module (right). 155

Chapter 1

Introduction

1.1 QGP from Heavy Ion Collisions

It is well known that four fundamental forces govern the universe: gravitation, electromagnetism, the weak interaction, and the strong interaction. Interestingly, each force has their own realm where one force dominates the others. Unlike the gravitation, which rules the massive celestial bodies, and the electromagnetism, which dominates on the atomic level, the strong interaction hides inside a nucleus, binding the most fundamental particles together.

1.1.1 QGP phase transition

The strong interaction can be described by Quantum Chromodynamics (QCD), which characterizes the interaction between quarks by exchange of gluons. QCD is a non-abelian gauge theory with gauge group SU(3), coupled to fermions (quarks) in the fundamental representation. The gauge invariant Lagrangian of the QCD can be written as [1]:

$$\begin{aligned}\mathcal{L}_{\mathrm{QCD}} &= \bar{\psi}_i(i\gamma^\mu(D_\mu)_{ij} - m\delta_{ij})\psi_j - \frac{1}{4}G^a_{\mu\nu}G^{\mu\nu}_a \\ &= \bar{\psi}_i(i\gamma^\mu\partial_\mu - m)\psi_i - gG^a_\mu\bar{\psi}_i\gamma^\mu T^a_{ij}\psi_j - \frac{1}{4}G^a_{\mu\nu}G^{\mu\nu}_a,\end{aligned} \tag{1.1}$$

and

$$G^a_{\mu\nu} = \partial_\mu G^a_\nu - \partial_\nu G^a_\mu - g f^{abc} G^b_\mu G^c_\nu, \tag{1.2}$$

where $\psi_i(x)$ are the quark fields; $G^a_\mu(x)$ are the gluon fields; $G^a_{\mu\nu}$ represents the gluon field strength tensor; γ^μ are the Dirac matrices; T^a_{ij} are the Gell-Mann matrices; f^{abc} are the structure constants of SU(3); m and g represent the quark mass and coupling constants of the theory.

As the binding force between quarks, the strong interaction instead of diminishing, becomes stronger when two quarks move away from each other. It takes infinite amount of energy to separate two quarks. Until now no free quarks have been found, and this is called quark confinement. The quark confinement has not yet been analytically proven, but can be demonstrated in lattice QCD [2].

In contrast, it has been discovered that in very high energy interactions or at short distances quarks and gluons interact much more weakly. This is called asymptotic freedom [3]. It can be understood by calculating the beta-function $\beta(g)$ that describes the variation of the coupling constant g with momentum exchange. For sufficiently short distances or large exchanges of momentum, and to the lowest order, the beta-function in an SU(3) gauge theory with n_f kinds of quark-like particles is

$$\beta(g) = \mu \frac{\partial g}{\partial \mu} = -(11 - \frac{2n_f}{3}) \frac{g^3}{16\pi^2}, \tag{1.3}$$

where μ is the energy scale of a given physical process. The beta-function is negative and the theory is asymptotically free if there are 16 or fewer flavors of quarks. The running coupling constant decreases logarithmically as

$$\alpha_s(\mu^2) \equiv \frac{g^2(\mu^2)}{4\pi} \approx \frac{1}{\beta_0 \ln(\mu^2/\Lambda^2)}, \tag{1.4}$$

where Λ is an overall scale defined by

$$\Lambda^2 = \mu_0^2 \exp[-\frac{1}{\beta_0} \frac{1}{\alpha_s(\mu_0^2)}]. \tag{1.5}$$

Here μ_0 is a constant scale and β_0 is the one-loop contribution to the expansion of beta-function. The value of α_s as a function of energy in different experimental measurements can be found in Figure 1.1 [4].

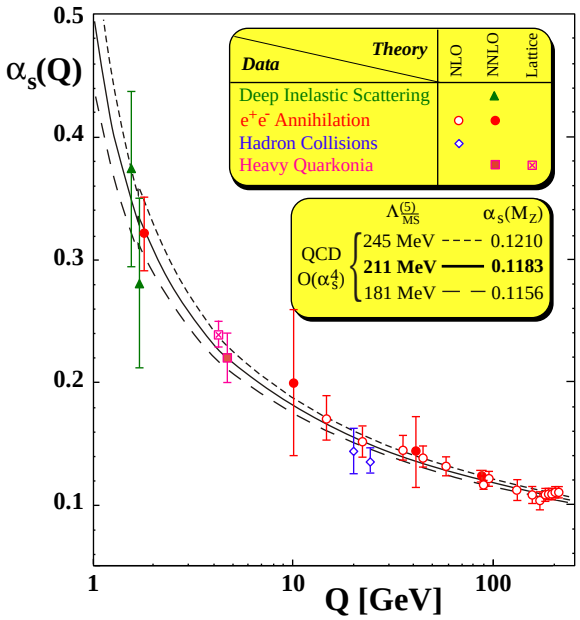

Figure 1.1: Summary of the QCD running coupling constant α_s as a function of the energy scale Q where the measurement was carried out, compared to the lattice QCD calculation.

At extremely high temperature and/or density the nucleons start to melt down due to the weaker interaction. Instead of being confined inside a nucleon, quarks and gluons are deconfined and dissolve into a new state of matter called "Quark Gluon Plasma" (QGP). The existence of the QGP and such a phase transition between a hadronic and a QGP phase is predicted by the lattice QCD calculation. For zero chemical potential the phase transition is expected to happen at temperature T_c ~170 MeV [5].

Figure 1.2 shows the pressure and energy density divided by T^4 as a function of temperature in lattice QCD calculations. Both variables rise at T_c. They indicate a significant change in the number of degrees of freedom (DOF) above T_c, and a possible formation of the QGP [5]. Quoted from the STAR white paper [6], the QGP is defined as "a (locally) thermally equilibrated state of matter in which quarks and gluons are deconfined from hadrons, so that color degrees of freedom become manifest over nuclear, rather than merely nucleonic volumes".

A schematic QCD phase diagram can be found in Figure 1.3 [7]. Experiments at

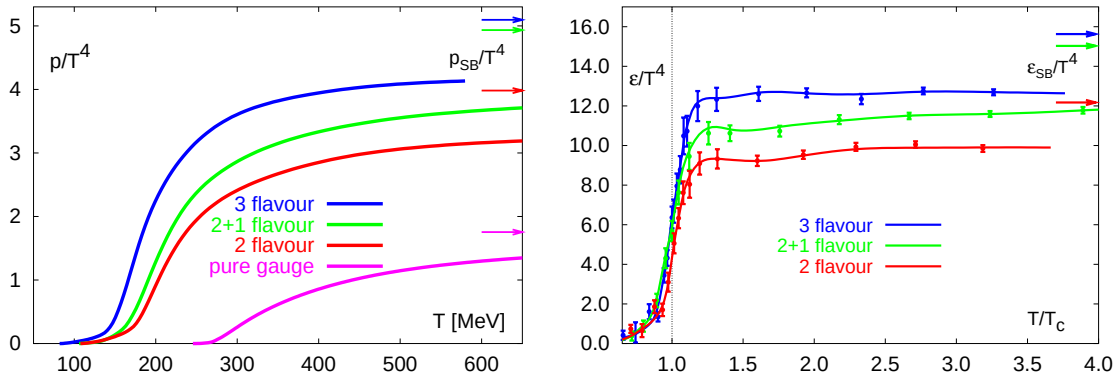

Figure 1.2: Lattice QCD calculation results for the pressure (left) and energy density (right) divided by T^4 of strongly interacting matter as a function of temperature.

top energy heavy-ion collisions at RHIC are expected to explore the phase transition at $\mu \simeq 0$.

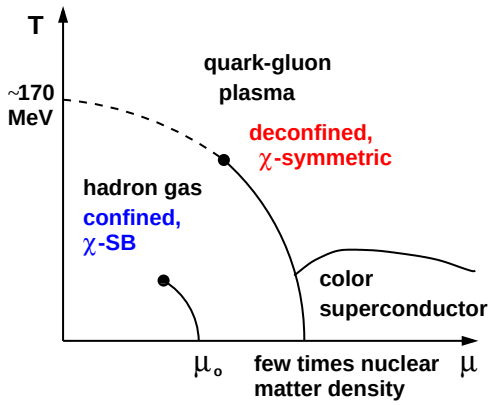

Figure 1.3: Schematic QCD phase diagram in chemical potential and temperature.

1.1.2 Relativistic heavy-ion collisions

To search for the QGP, an extreme condition of high temperature and/or density is required to produce the phase transition from hadronic matter to the QGP. The relativistic heavy-ion collision is an ideal tool to achieve it. Relativistic heavy-ion collision experiments have been carried out since 1980's at BNL-AGS and CERN-SPS, where fixed target experiments with beam energy ranging from 10-160 GeV/c

per nucleon were performed. The Relativistic Heavy Ion Collider (RHIC) at BNL [8] is currently the largest active heavy-ion collider in heavy-ion collisions. It is designed to perform collisions between heavy ions with energy up to $\sqrt{s_{NN}}$=200 GeV, and between nucleons up to 500 GeV. Since the first RHIC run was performed in 2000, RHIC has completed 8 physics runs by 2008. The Large Hadron Collider (LHC) at CERN [9] is expected to start its first physics run in the upcoming future and will be able to perform heavy-ion collisions at $\sqrt{s_{NN}}$=5.5 TeV.

The evolution of a relativistic heavy-ion collision is shown schematically in Figure 1.4. Due to the Lorentz contraction the two nuclei can be described as two thin disks and approach each other at near the speed of light. At the collision, protons and neutrons in the overlapping region of two nuclei experience strong multiple scattering and the longitudinal kinetic energy is transformed into the local energy concentrated at the collision point with extremely high temperature. Nucleons will dissolve at such an high temperature and quarks and gluons are set free. The strong interaction between quarks and gluons is expected to be sufficient to lead to local thermal and chemical equilibrium after a very short time, and the QGP is formed. At this stage the partonic scatterings with high momentum transfer are dominant and high energy leptons and jets are created, such as $q\bar{q}$ pairs, gluons, and direct photons. As the QGP expands rapidly and cools down, mesons and baryons start to be created by fragmentation and quark coalescence. The fireball then reaches chemical freeze-out, evolving into an strongly interacting hadronic gas. As it continues to cool down, it reaches kinetic freeze-out and particles stop interacting. The collision ends at this point.

1.1.3 Glauber model

The dynamic of a nucleus-nucleus collision can be described by the Glauber model [10, 14] of multiple collision processes. It provides a quantitative consideration of the geometrical configuration of the nuclei when they collide. The Glauber model views the collision of two nuclei in terms of the individual interactions of the constituent nucleons.

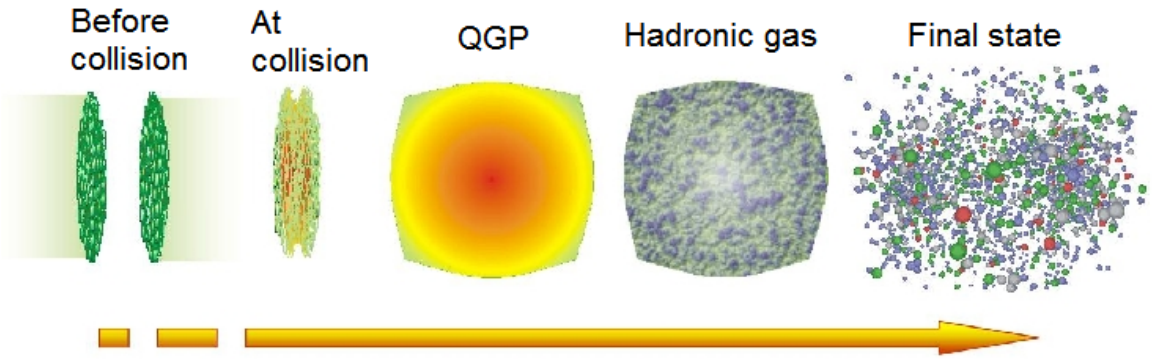

Figure 1.4: A schematic picture of the evolution of a relativistic heavy ion collision.

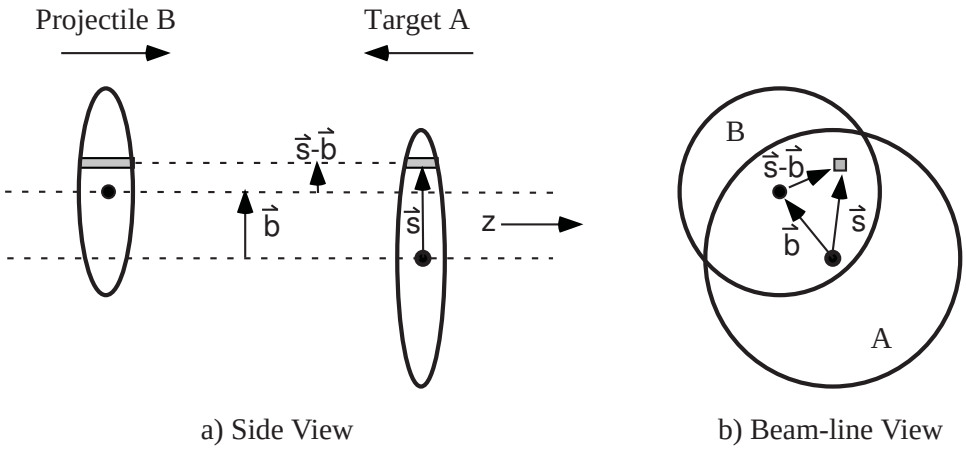

Figure 1.5: Schematic representation of the optical Glauber model geometry, with transverse (a) and longitudinal (b) views.

Figure 1.5 shows a schematic view of two heavy ions, target A and projectile B, colliding at relativistic speeds with impact parameter b. For the two flux tubes located at a displacement $\mathbf{s}$ with respect to the center of the target nucleus and a distance $\mathbf{s}-\mathbf{b}$ from the center of the projectile, they overlap during the collision. The probability per unit transverse area of a given nucleon being located in the target flux tube is $\hat{T}_A(\mathbf{s}) = \int \hat{\rho}_A(\mathbf{s}, z_A)dz_A$, where $\hat{\rho}_A(\mathbf{s}, z_A)$ is the probability per unit volume, normalized to unity, for finding the nucleon at location $(\mathbf{s}, z_A)$. A similar expression follows for the projectile nucleon. The product $\hat{T}_A(\mathbf{s})\hat{T}_B(\mathbf{s}-\mathbf{b})d^2s$ then gives the joint probability per unit area of nucleons being located in the respective overlapping target and projectile flux tubes of differential area d^2s. Integrating this product over all values of $\mathbf{s}$ defines the thickness function $\hat{T}(\mathbf{b})$, with

$$\hat{T}_{AB}(\mathbf{b}) = \int \hat{T}_A(\mathbf{s})\hat{T}_B(\mathbf{s}-\mathbf{b})d^2s. \tag{1.6}$$

It is interpreted as the effective overlap area for which a specific nucleon in A can interact with a given nucleon in B. The probability of an interaction occurring is then $\hat{T}(\mathbf{b})\sigma_{\text{inel}}^{\text{NN}}$, where $\sigma_{\text{inel}}^{\text{NN}}$ is the nucleon-nucleon inelastic cross section. Elastic processes lead to very little energy loss and are consequently not considered in the Glauber model calculations. Then the probability of having n such interactions between nucleus A (with A nucleons) and B (with B nucleons) is given as a binomial distribution,

$$P(n, \mathbf{b}) = \begin{pmatrix} AB \\ n \end{pmatrix} \left[\hat{T}_{AB}(\mathbf{b})\sigma_{\text{inel}}^{\text{NN}}\right]^n \left[1 - \hat{T}_{AB}(\mathbf{b})\sigma_{\text{inel}}^{\text{NN}}\right]^{AB-n} \tag{1.7}$$

where the first term is the number of combinations for finding n collisions out of AB possible nucleon-nucleon interactions, the second term the probability for having exactly n collisions, and the last term is the probability of exactly $AB-n$ misses.

Based on this probability distribution, the total probability of an interaction between A and B is

$$\frac{d^2\sigma_{\text{inel}}^{\text{A+B}}}{db^2} \equiv p_{\text{inel}}^{\text{A+B}}(b) = \sum_{n=1}^{AB} P(n, \mathbf{b}) = 1 - \left[1 - \hat{T}_{AB}(\mathbf{b})\sigma_{\text{inel}}^{\text{NN}}\right]^{AB}. \tag{1.8}$$

The vector impact parameter can be replaced by a scalar distance if the nuclei are

not polarized. In this case, the total cross section can be found as

$$\sigma_{\rm inel}^{\rm A+B} = \int_0^\infty 2\pi b db \left\{ 1 - \left[1 - \hat{T}_{AB}(b)\sigma_{\rm inel}^{\rm NN} \right]^{AB} \right\}. \tag{1.9}$$

Two important parameters of heavy-ion collisions can be calculated using the Glauber model. The total number of nucleon-nucleon collisions N_{bin} is calculated as

$$N_{bin}(b) = \sum_{n=1}^{AB} nP(n,b) = AB\hat{T}_{AB}(b)\sigma_{\rm inel}^{\rm NN}, \tag{1.10}$$

using the result for the mean of a binomial distribution. Note that at time T_{AB} is used instead of $\hat{T}_{AB}$, where $T_{AB} = AB\hat{T}_{AB}$. The number of nucleons in the target and projectile nuclei that interact is called the number of participants N_{part}. The N_{part} at impact parameter b is given by [11]

$$\begin{aligned} N_{part}(\mathbf{b}) = A \int \hat{T}_A(\mathbf{s}) \left\{ 1 - \left[1 - \hat{T}_B(\mathbf{s}-\mathbf{b})\sigma_{\rm inel}^{\rm NN} \right]^B \right\} d^2s \\ + B \int \hat{T}_B(\mathbf{s}-\mathbf{b}) \left\{ 1 - \left[1 - \hat{T}_A(\mathbf{s})\sigma_{\rm inel}^{\rm NN} \right]^A \right\} d^2s. \end{aligned} \tag{1.11}$$

There are two practical methods to calculate N_{bin} and N_{part}: the optical and Monte Carlo Glauber approaches [12]. The Optical Glauber approach is based on a smooth nuclear matter distribution and numerical evaluation of the analytic Glauber integrals. The Monte Carlo approach is based on the random distribution of nucleons according to the Woods-Saxon density $\rho_A(r) = \frac{\rho_0}{1+e^{(r-r_0)/a}}$, with nuclear collisions at a given impact parameter modeled by the incoherent interaction of all nucleon pairs. Comparison between data and calculation demonstrates that the Glauber approach provides a sound basis for modeling geometric effects in nuclear collisions at RHIC energies [13].

1.2 QGP signatures in Heavy Ion Collision

As part of their efforts to searching for and studying the QGP, both theoretically and experimentally, physicists have proposed and investigated in depth a number of possible signatures or properties of this new state of matter. They include several traditional ones, such as di-lepton production, J/Ψ suppression, direct photons, anisotropic flow, and strangeness enhancement [14]; and some newer ones such as jet quenching, heavy quark energy loss. In this section several topics relevant to later chapters will be briefly reviewed.

1.2.1 Jet quenching for light quarks

One of the most striking discoveries of the RHIC experiments is the suppression of high p_T particles in central nucleus-nucleus collisions relative to primary proton-proton (p+p) collisions [15, 16]. This effect is absent in earlier, lower energy, SPS collisions. Jet quenching refers to the energy loss of high p_T partons via both radiative and collisional channels when they are traveling through the QGP. For light partons, the radiative energy loss is expected to be dominant. Theoretically there are four major models in calculating the in-medium modification of light partons, including the Gyulassy-Levai-Vitev (GLV) [17], Armesto- Salgado-Wiedemann (ASW) [18], Arnold-Moore-Yaffe (AMY) [19], and higher-twist [20] approaches. We will briefly discuss the GLV approach here.

The GLV approach assumes the medium to be composed of heavy, almost static, color scattering centers (with Debye screened Yukawa potentials) which are well separated in the sense that the mean free path of a parton $\lambda \gg 1/\mu$, the color screening length of the medium. The opacity of the medium $\overline{n}$ quantifies the number of scattering centers seen by a parton as it passes through the medium, *i.e.*, $\overline{n} = L/\lambda$, where L is the thickness of the medium. At leading order in opacity, a hard parton, produced locally in such a plasma with a large forward energy $E \gg \mu$, scatters off one such potential and in the process radiates a soft gluon. Multiple such interactions in a Poisson approximation are considered to calculate the probability for the parton to lose a finite amount of its energy. To the first order, the total radiative energy loss is

given by

$$\Delta E^{(1)} = \frac{C_R \alpha_s}{N(E)} \frac{L^2 \mu^2}{\lambda_g} \log \frac{E}{\mu} \tag{1.12}$$

where E is jet energy; C_R is the Casimir of the (spin 1/2) jet in the d_R dimensional color representation; L is the plasma depth; μ is the typical transverse momentum transfer; λ_g is the radiated gluon mean free path; and N is the number of gluons emitted. The energy loss is predicted to be proportional to the gluon density $\frac{dN_g}{dy}$. This effect results in significant amount of energy loss for high p_T partons traveling through the QGP, and thus a suppression of high p_T hadron production in heavy-ion collisions. As a result, by comparing experimental results of hadron production suppression to theoretical calculations with different $\frac{dN_g}{dy}$, we can reveal important information about the QGP.

Experimentally, jet quenching is observed in two ways: the suppression of inclusive hadron yield at high p_T [15, 16] and the suppression of away-side yields associated with a high p_T trigger hadron [21] in central heavy-ion collisions. For the inclusive hadron yield, the suppression is quantified by the observables of nuclear modification factors R_{AA} and R_{CP}, which are defined as the hadron yield relative to the peripheral nucleus-nucleus and p+p collisions:

$$R_{CP}(p_T) = \frac{[d^2N/p_T dy dp_T/\langle N_{bin}\rangle]^{central}}{[d^2N/p_T dy dp_T/\langle N_{bin}\rangle]^{peripheral}} \tag{1.13}$$

$$R_{AA}(p_T) = \frac{d^2N_{AA}/dy dp_T/\langle N_{bin}\rangle}{d^2\sigma_{pp}/dy dp_T/\sigma_{pp}^{inel}} \tag{1.14}$$

Where $\langle N_{bin}\rangle$ is the centrality dependent average number of binary nucleon-nucleon collisions per heavy-ion event from a Glauber calculation [22], as described in Section 1.1.3. The σ_{pp}^{inel} is taken to be 42 mb and 36 mb for $\sqrt{s_{NN}}$=200 GeV and 62.4 GeV, respectively [23].

Figure 1.6 shows the STAR results for π and proton R_{AA} and R_{CP} as a function of p_T in Au+Au collisions at $\sqrt{s_{NN}}$=200 and 62.4 GeV [15]. In central Au+Au collisions, hadron yields indicate up to a factor of 5 suppression relative to p+p and peripheral Au+Au collisions at high p_T. The π^0 yield measured by the PHENIX experiment shows a similar result, indicating a roughly constant suppression factor

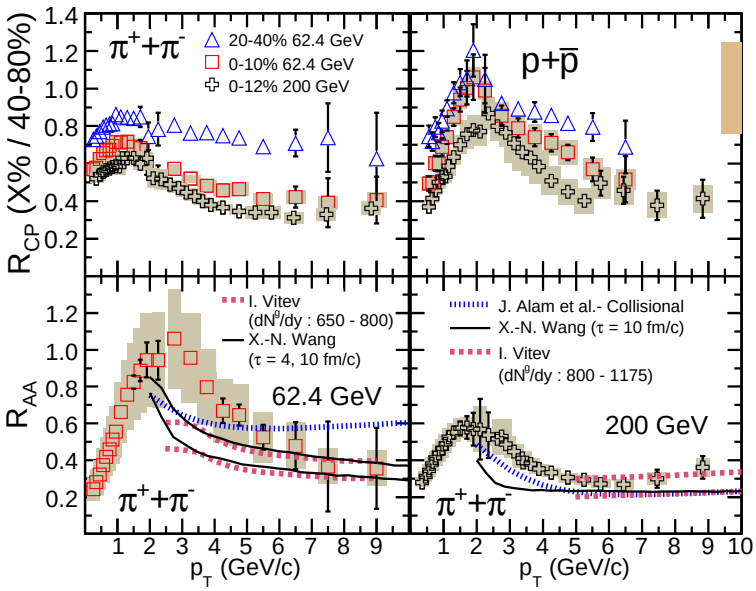

Figure 1.6: p_T dependence of nuclear modification factors R_{AA} and R_{CP} of hadrons in Au+Au collisions at $\sqrt{s_{NN}}$=200 and 62.4 GeV. Data are compared to calculations from radiative and collisional energy loss scenarios. [15]

up to 20 GeV/c [16]. Theoretical calculations based on gluon radiation describe the data of light quark energy loss well, as suggested in Figure 1.6.

The di-hadron correlation measures the azimuthal angular correlation between a high p_T trigger particle and other lower p_T associated particles. Figure 1.7 shows STAR measurements of azimuthal correlations between high p_T hadrons in p+p, central d+Au, and central Au+Au collisions, with trigger hadron $p_T^{trig} > 4$ GeV/c and associated hadron 2 GeV/$c < p_T^{asso} < p_T^{trig}$. In Au+Au collisions the contribution from elliptic flow correlation has been subtracted, assuming that the di-hadron correlation consists of contributions from jets and elliptic flow only [21]

$$D^{di-hadron} = D^{jet} + B[1 + 2v_2^2 \cos(2\Delta\phi)]. \tag{1.15}$$

All collision systems show an enhanced correlation at $\Delta\phi \approx 0$ of hadron pairs from a single jet, with similar correlation strengths and widths. However, correlations of hadron pairs from back-to-back dijets on the away side ($\Delta\phi \approx \pi$) are only observed in p+p and d+Au collisions, but strikingly absent in central Au+Au collisions [6].

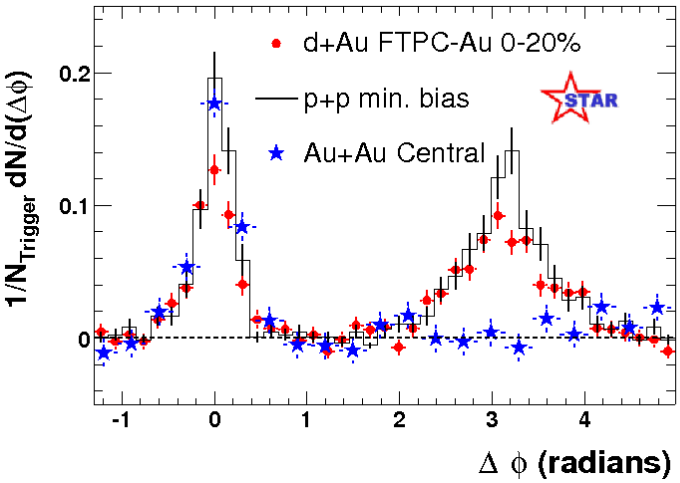

Figure 1.7: Di-hadron azimuthal correlations at high p_T in p+p, central d+Au and central Au+Au collisions (background subtracted) from STAR.

For peripheral Au+Au collisions the correlation appears quite similar to that seen in p+p and d+Au collisions. It suggests that high p_T jets lose significant amount of energy when traveling through the medium and dissolve into the bulk. A variable similar to R_{AA} defined as $I_{AA} = Y_{AA}^{away}/Y_{pp}^{away}$ is used to quantify the away-side yield suppression, where $Y_{AA(pp)}^{away}$ is the away-side associated particle yield in di-hadron correlation in heavy-ion and p+p collisions, respectively. I_{AA} of di-hadron correlation shows similar magnitude of suppression as the single hadron yields.

In this thesis, the first STAR results on π^0 production over an extended p_T-range from $\sqrt{s_{NN}}$=200 GeV Au+Au collisions will be presented in Chapter 3.

1.2.2 Direct photon HBT

In relativistic heavy-ion collisions "direct photons" is used to mean photons not coming from hadron decays. Direct photons are created throughout the whole lifetime of a heavy-ion collision. A model calculation of direct photon components at RHIC energy from Turbide *et al.* is shown in Figure 1.8 [24]. At energies below 1 GeV, the major source of direct photons is expected to be thermal photons from the later stage of the hadron gas; at high energy above 3 GeV the spectrum is dominated by prompt pQCD photons from very early hard scatterings such as $q\bar{q}$ annihilation and

Compton scattering; at intermediate energy the QGP thermal photons stand out. An additional calculation also demonstrates that photons from high p_T jets interacting with the plasma, such as bremsstrahlung photons and jet-photon conversions [25], can contribute significantly in the intermediate energy range. The production of direct photons is proportional to the temperature of the system, so measuring the direct photon yields helps to reveal properties of different stages of the fireball. Therefore direct photons carry substantial information about the history of the collision. Due to their electro-magnetic interaction, direct photons do not interact with the medium, and thus preserve such information until the final state [26]. This superiority of direct photons over hadrons makes the direct photon HBT a unique tool to understand the collision.

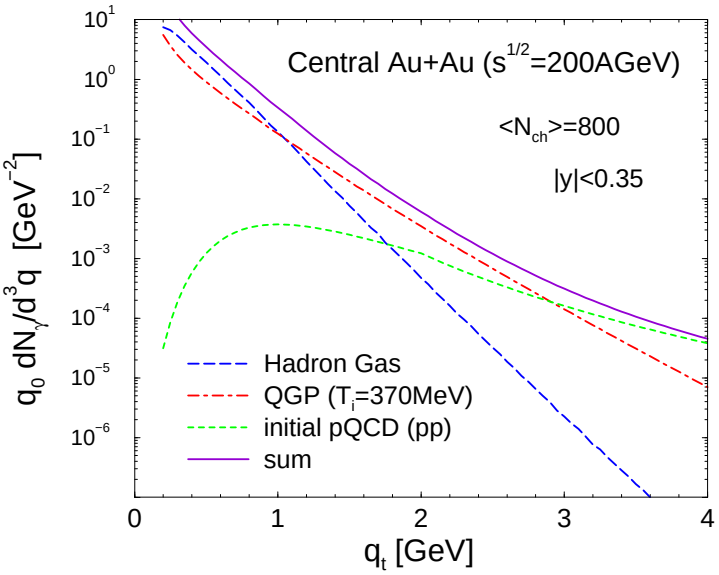

Figure 1.8: Integrated photon emission spectra from central Au+Au collisions at RHIC [24].

The technique of HBT interferometry was first introduced by Hanbury-Brown and Twiss to measure the angular size of stars in 1950s [27]. Later this technique was borrowed and widely used in nuclear physics and heavy-ion collisions. Unlike the amplitude interference, such as the Young two-slit experiment, the HBT interferometry

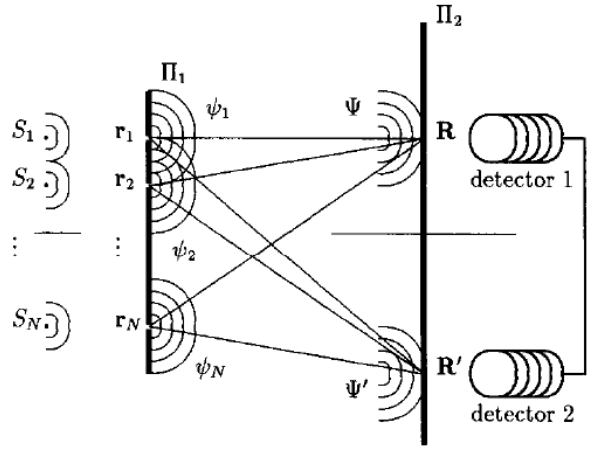

Figure 1.9: Schematic view of an intensity interference experiment using two detectors in electronic coincidence.

is a second-order intensity interference. Figure 1.9 shows a simple example of intensity interference experiment using two detectors in coincidence measuring intensity of photons from N chaotic light sources whose distance from two detectors is L. The correlation function is defined as [28]

$$C_{12}(\boldsymbol{R}, \boldsymbol{R}') = \frac{I(\boldsymbol{R}, \boldsymbol{R}')}{I(\boldsymbol{R})I(\boldsymbol{R}')} = \frac{\langle|\Psi|^2|\Psi'|^2\rangle}{\langle|\Psi|^2\rangle\langle|\Psi'|^2\rangle} \tag{1.16}$$

$$\Psi = \sum_{i=1}^{N} \varphi_i \psi_i, \quad \psi_i = \exp\{ik \cdot (\boldsymbol{R} - \boldsymbol{r}_i)\} \tag{1.17}$$

where φ_i represents the phase of the source at $\boldsymbol{r}_i$. The final correlation function is

$$C_{12}(\boldsymbol{q}) = 1 + \frac{2}{N^2} \sum_{i,j=1;j>i}^{N} \cos\{\boldsymbol{q} \cdot (\boldsymbol{r}_i - \boldsymbol{r}_j)\} = 1 + \frac{2}{N^2} \sum_{i,j=1;j>i}^{N} \cos(k\alpha_{ij}L) \tag{1.18}$$

where $\boldsymbol{q} = \boldsymbol{k}_1 - \boldsymbol{k}_2$. So it depends on the Fourier transform of the source distribution. For a star with a light source distribution $\rho(r)$, the correlation function becomes

$$C_{12} = 1 + |\varrho(k\alpha L)|^2 \tag{1.19}$$

where $\varrho(x)$ is the normalized Fourier transform of $\rho(r)$. Therefore, if the correlation function C_{12} is measured, the source profile can be unfolded.

In relativistic heavy-ion collisions the expression for the correlation function of two photons is derived as [29]

$$C_2(q,K) = 1 + \lambda \frac{|\int d^4x S(x,K) e^{iqx}|^2}{|\int d^4x S(x,K)|^2} \tag{1.20}$$

where $q = k_1 - k_2$ is the relative momentum of the photon pair; $K = (k_1 + k_2)/2$ is half of the total pair momentum; $S(x,K)$ is the Wigner density of the photon source; and λ is the strength of the correlation, equal to 1 for a fully chaotic source and 0 for a fully coherent source. For photons $\lambda = \frac{1}{2}$ taking into account the photon spin [30].

The most commonly used source parameterisation is Gaussian:

$$\begin{aligned} \rho(r) &= \rho_0 \exp(-x^2/2R_x^2 - y^2/2R_y^2 - z^2/2R_z^2 - t^2/2\tau^2) \\ \varrho(q) &= \exp(-q_x^2 R_x^2/2 - q_y^2 R_y^2/2 - q_z^2 R_z^2/2 - q_0^2\tau^2/2) \end{aligned} \tag{1.21}$$

which is expressed in Cartesian coordinates in the lab frame. A more popular choice of coordinate axes is the Pratt-Bertsch parameterisation [31], where the correlation function can be written as

$$C_2(q,K) = 1 + \exp(-R_s^2 q_s^2 - R_o^2 q_o^2 - R_l^2 q_l^2 - 2R_{ol}^2 q_o q_l) \tag{1.22}$$

where l denotes the longitudinal direction along the beam, o the outward direction along the transverse pair momentum vector K, and s the third Cartesian direction. These HBT radii mix spatial and temporal information on the source in a non-trivial way. The cross term vanishes in Au+Au collisions at RHIC where the source is symmetric under $x_l \to -x_l$ [32]. When statistics is limited and a multiple dimension analysis is impossible, a one-dimension projected correlation function is often used, although it only contains averaged information about the source's space-time dimensions.

$$\begin{aligned} C_2(Q) &= 1 + \lambda \exp(-Q^2 R_Q^2) \\ Q &= \sqrt{\boldsymbol{q}^2 - q_0^2} \end{aligned} \tag{1.23}$$

For photons Q corresponds to the invariant mass $m_{inv} = \sqrt{p_0^2 - \boldsymbol{p}^2}$. As a result, the di-photon invariant mass distribution is actually used to calculate the one-dimension correlation function.

It is expected that photons with higher energy are created in the earlier stage of the collision. As a result, it is assumed that a study of the p_T dependence of direct photon HBT can give a picture of the dynamical evolution of system size, energy density, and temperature.

Experimentally, the direct photon HBT analysis is very challenging due to the very small fraction of direct photons among photons in the final state. Most of the background photons are from hadron decays (π^0, η, ω...). The typical correlation strength λ is proportional to $(\frac{N_{direct\gamma}}{N_{inclusive\gamma}})^2$ which is on the order of 10^{-3}. As a result, direct photon HBT is statistically demanding and requires very tight control of systematics. Fortunately, the direct photon HBT signal can be disentangled from the correlation of decay photons, which only contribute to the invariant mass peak region of hadrons [29]. For example, the photon correlation due to π^0 decay kinematics produces a peak at 135 MeV/c^2, well separated from the HBT signal. Photons from π^0 decays will not produce a detectable HBT peak either. The typical distance between two π^0 decay photons is 2.5×10^7 fm, so the peak in relative momentum of two photons is 4 μeV/c^2 wide. However, the residual correlation of decay photons due to the π^0 HBT correlation should be carefully dealt with, but can be removed [29].

In relativistic heavy-ion collisions HBT interferometry using hadrons has produced fruitful results [33]. In contrast, results of direct photon HBT are relatively rare. One of the few results is from the WA98 Collaboration at SPS energy [34]. Figure 1.10 shows the two-photon correlation function in two K_T bins. The HBT signal is fitted and the radius parameter R_Q as in Equation 1.23 is extracted. From the strength of the correlation the $\frac{N_{direct\gamma}}{N_{inclusive\gamma}}$ ratio can be calculated. It is valuable to know the direct photon yield at very low p_T where other statistical subtraction methods fail. Recent direct photon HBT results from the PHENIX Collaboration have been reported at the Quark Matter 2006 conference [35].

The first attempt of measuring direct photon HBT interferometry in STAR will be presented in Chapter 4.

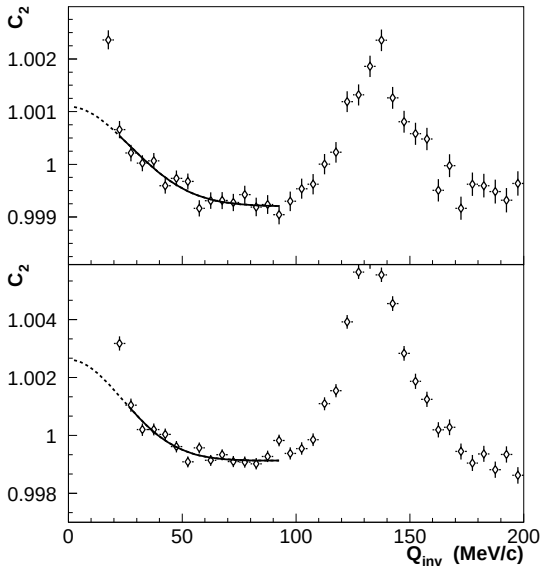

Figure 1.10: The two-photon correlation function with average photon momenta 100< K_T <200 MeV/c (top) and 200< K_T <300 MeV/c (bottom) fitted with a Gaussian source shape from the WA98 Collaboration at SPS energy [34].

1.2.3 Direct photon elliptic flow

The discovery of strong anisotropic flow is another very important achievement at RHIC. Anisotropic flow results in the anisotropic distribution of particles in the azimuthal plane with respect to the reaction plane. When two nuclei collide with non-zero impact parameter b, the overlapping area has an almond shape (shown in Figure 1.11). The impact parameter defines the reaction plane together with the beam direction. After the collision, such a geometrical anisotropy results in different pressure gradients in different azimuthal directions, with the steepest gradient along the impact parameter vector. As the fireball expands, the rapid thermalization in the QGP creates collective movement of particles. They gain more momentum and thus pushes more particles in the reaction plane direction. So the anisotropy in coordinate space is transformed into anisotropy in momentum space.

The anisotropic flow can be parameterized by a Fourier expansion of the azimuthal

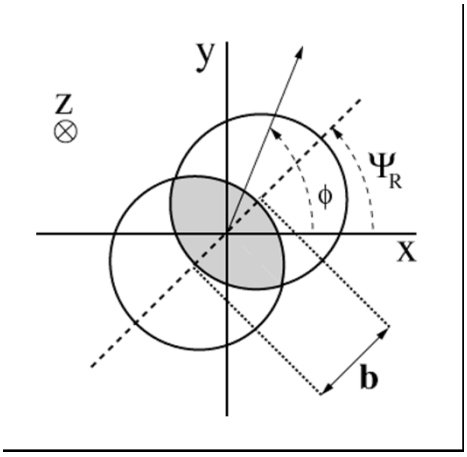

Figure 1.11: Schematic view of two nuclei colliding with impact parameter b.

distribution of final state particles [36]:

$$E\frac{d^3N}{dp^3} = \frac{1}{2\pi}\frac{d^2N}{p_T dp_T dy}\{1 + \sum_{n=1}^{\infty} 2v_n \cos[n(\phi - \Psi_r)]\} \tag{1.24}$$

where Ψ_r denotes the true reaction plane angle. The sine terms vanish due to the reflection symmetry with respect to the reaction plane. The first two non-constant terms of the expansion are of most importance. They are called direct flow (v_1) and elliptic flow (v_2).

In real events, however, the true direction of reaction plane is unknown. We estimate its direction by studying the distribution of charged tracks in different pseudorapidity ranges, or the distribution of surviving neutrons from the heavy-ion beams in the very forward direction. The estimated reaction plane is called the event plane. In STAR, charged tracks in the TPC and FTPC, and neutron signals in the Zero Degree Calorimeter (ZDCSMD) are used to measure the event plane. More details about the event plane determination can be found in Chapter 5.

A number of methods have been developed to calculate v_2, including the event plane method [36], the scalar product method [37], the η-subevent method [38], the cumulant method [39], and the Lee-Yang zero method [40]. These methods have different sensitivities to non-flow effects and v_2 event-by-event fluctuations. The non-flow effects are correlations not associated with the reaction plane, including resonance decay, HBT correlations, final state interactions, and jets. A more detailed comparison between different methods can be found in Ref. [38].

Elliptic flow is sensitive to the initial state of the collision and the mechanism of the interaction. As a result, it can provide stringent tests on different models. Many v_2 results from RHIC experiment have been published [41, 38, 37] and two of the most well established model types are hydrodynamic [42] and quark coalescence models [43]. In the hydrodynamic framework, one assumes zero mean free path and local thermalization. Therefore particles with different masses will have the same speed, which predicts a mass dependence of v_2 shape as a function of p_T: heavier particles have smaller v_2 at low p_T. In the coalescence model, it assumes that hadrons are formed by coalescence or recombination of constituent quark at intermediate p_T. Assuming an anisotropy of constituent quarks prior to hadronization, it predicts that v_2 approximately scale with the number of constituent quarks (n), with v_2/n vs. p_T/n for all hadrons falling on a universal curve.

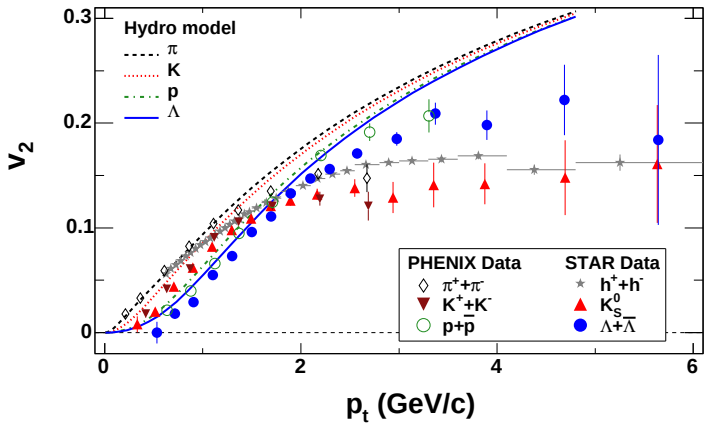

Figure 1.12: v_2 vs. p_T for identified particles from minimum bias Au+Au collisions at RHIC compared to hydro calculations.

Figure 1.12 and 1.13 shows the identified particle v_2 results at RHIC [41] compared to two model calculations. At low p_T, the hydrodynamic models successfully describe the rising trend of v_2 and the mass dependence of the v_2 shape. However, the data show that v_2 starts to saturate at $p_T \sim 2$ GeV/c, while the hydro prediction keeps rising. At intermediate p_T, the universal constituent quark number scaling is supported by the data. Such agreement provides evidence for local thermalization and partonic degrees of freedom, and thus strongly supports the existence of the QGP.

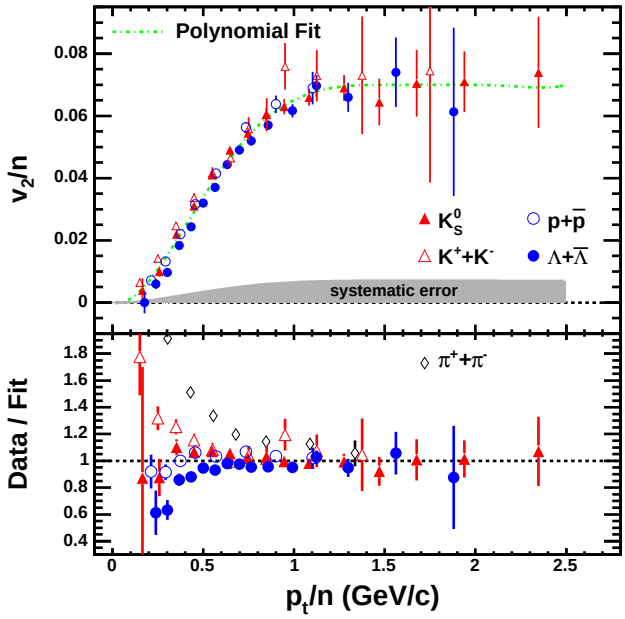

Figure 1.13: Identified particle v_2 scaled by the number of constituent quarks (n) from minimum bias Au+Au collisions. Bottom panel is the ratio of v_2/n to the fitted curve.

The collisions at RHIC energies are dominated by very strongly interacting matter with very short constituent mean free path, and is essentially a "perfect liquid" [6].

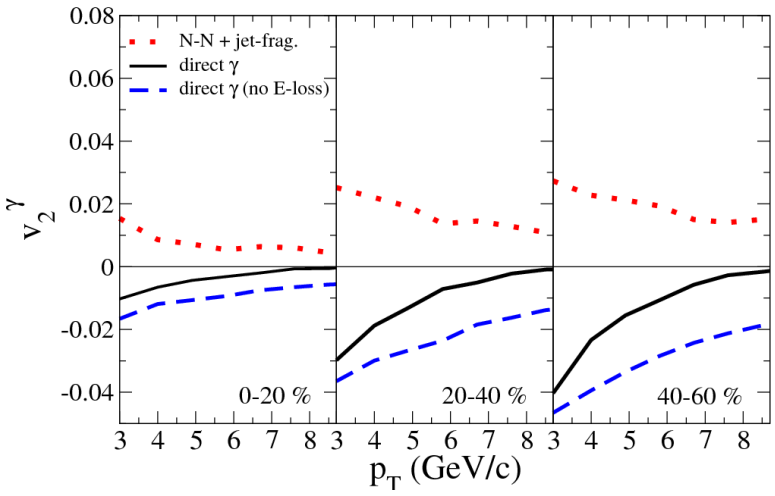

Figure 1.14: Direct photon v_2 as a function of p_T for Au+Au collisions at RHIC considering photons from jets. The dotted lines show v_2 for primary hard photons and jet fragmentation only; the solid and dashed lines show all direct photons with and without energy loss of jets taken into account.

As discussed in the last section, direct photons are a unique probe in heavy-ion collisions, and direct photon v_2 is another useful tool. QGP thermal radiation is expected to be one of the major sources of direct photons from RHIC collisions in the intermediate and high p_T ranges [24, 44]. Other sources include initial hard scattering [24], jet fragmentation, in-medium bremsstrahlung and jet-photon conversion [25]. Direct photons from different mechanisms are expected to have different v_2 values [45], resulting in rich structures as predicted by different model calculations [45, 46]. Figure 1.14 and 1.15 shows two model predictions of direct photon and thermal photon v_2. One eye-catching prediction is that in the intermediate p_T range of 3-8 GeV/c direct photons can have negative v_2 due to the significant contribution of in-medium bremsstrahlung, jet quark thermal quark annihilate ($q + \bar{q} \rightarrow \gamma + g$), and jet-photon conversion ($q(\bar{q}) + g \rightarrow q(\bar{q}) + \gamma$) [45]. The probability that these processes happen increases with the path length d of the jet going through the plasma.

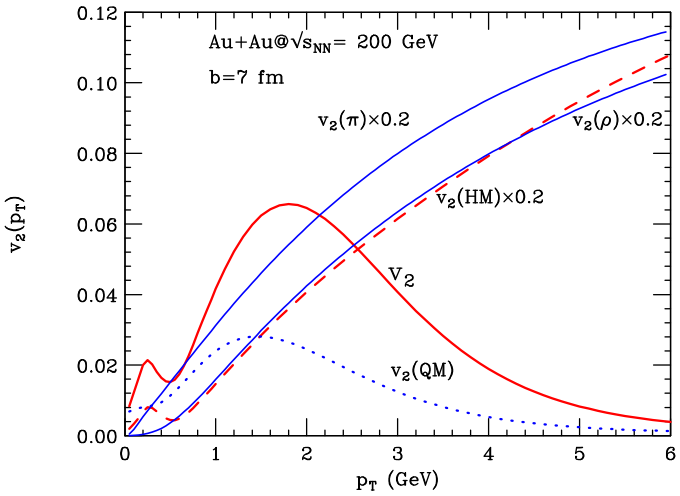

Figure 1.15: $v_2(p_T)$ for thermal photons from off-central 200 GeV Au+Au collisions at b=7 fm (red solid curve). Quark (blue dotted curve) and hadronic matter (red dashed curve) contributions are shown separately, and the v_2 of π (upper blue solid curve) and ρ (lower blue solid curve) mesons are shown for comparison.

Therefore, photons from these processes are preferentially emitted in the off-reaction-plane direction where the medium is thicker, which leads to a negative v_2.

On the other hand, photons from the QGP and hadronic gas thermal radiation are also of great interest [46]. At low p_T a reduction of thermal photon v_2 around p_T ~0.4 GeV is predicted due to a transition of the thermal photon production mechanism from $\rho \rightarrow \pi\pi\gamma$ and $\pi\pi \rightarrow \rho\gamma$ to collision-induced conversions of vector mesons into photons such as $\pi\rho \rightarrow \pi\gamma$. At $p_T < 0.4$ GeV/c, hadronic photon elliptic flow tracks the v_2 of π, while at $p_T > 0.4$ GeV/c, it tracks the v_2 of other vector mesons such as ρ, which have less elliptic flow due to heavier masses and cause the reduction of thermal photon v_2. At higher p_T the thermal photon v_2 is expected to keep decreasing but remains positive, reflecting the absence of transverse flow during the earliest, hottest stage of the QGP. As a summary, studying the v_2 of direct photons can help establish the existence of the QGP and provide a stringent test to the mechanism of direct photon production.

Similar to the direct photon HBT study, measuring direct photon v_2 is difficult due to a large number of background photons from meson decays. Direct photon v_2

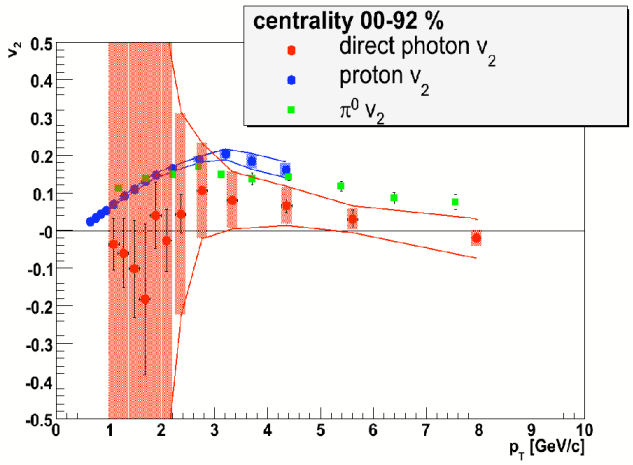

Figure 1.16: PHENIX direct photon v_2 as a function of p_T in minimum bias Au+Au collisions at $\sqrt{s_{NN}}$=200 GeV. Proton and π^0 v_2 are plotted for comparison.

can be obtained by statistically subtracting the contributions of decay photons from the inclusive photon v_2. The PHENIX Collaboration reported results of direct photon v_2, which is shown in Figure 1.16 [47]. With large systematic error bars, direct photon v_2 is consistent with $v_2^{\gamma}(p_T) = 0$, but more likely to be positive. So far at RHIC there is no strong evidence for the significant contribution of direct photons induced by high energy jets.

The STAR results on inclusive photon v_2 and the approach to direct photon v_2 in 200 GeV Au+Au collisions will be presented in Chapter 5.

1.2.4 Muon probes

Muon probes are another important signature for the QGP and are sensitive to much interesting physics. Similar to direct photons, muons do not suffer from strong interactions so they serve as a penetrating probe of the QGP. The di-muon spectra is helpful in studying di-muons from the QGP thermal radiation, quarkonia production such as J/Ψ and Υ, Drell-Yan, and light vector meson production [48]. Figure 1.17 shows the rich structure of the di-muon spectra from the NA50 Collaboration in Pb-Pb collisions at 158 GeV/nucleon [49]. In addition, single muons can be used to study

heavy quark hadrons via the semi-leptonic decay channel, and $e-\mu$ correlations can distinguish lepton pair production and heavy quark decay such as $c+\bar{c} \rightarrow e+\mu(e)$ and $B \rightarrow e(\mu)+c \rightarrow e+\mu(e)$.

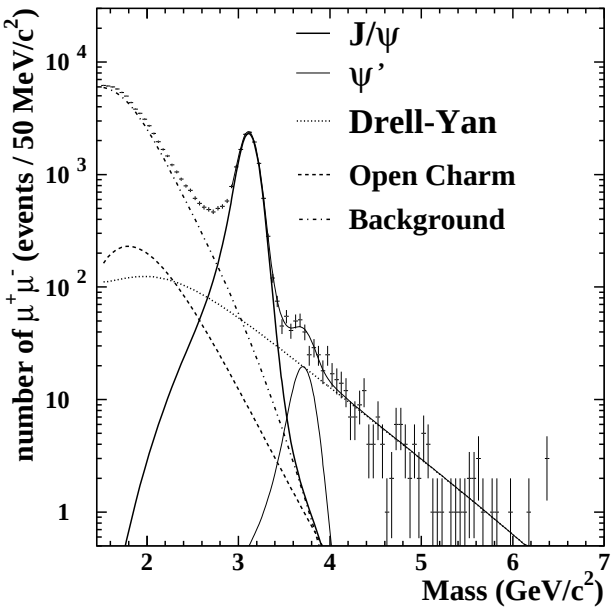

Figure 1.17: Opposite-sign di-muon invariant mass spectrum in Pb-Pb collisions at 158 GeV/nucleon. The lines are fit results of different components.

Although some of these analyses can be performed using electrons too, muons are superior in several aspects. 1. Signal-to-background ratio: The biggest drawback of electrons is the very large background from γ conversions in detector materials, and from π^0 and η Dalitz decays. Muons do not suffer from such contaminations, although they have an additional background from charged pion decays. 2. Trigger: Due to the high signal-to-background ratio in muon detectors, it is possible to set up a muon trigger even in central nucleus-nucleus collisions. 3. Energy loss: Muons experience much less radiative energy loss in detector materials and thus can provide much higher momentum resolution, which significantly improves the mass resolution of vector mesons.

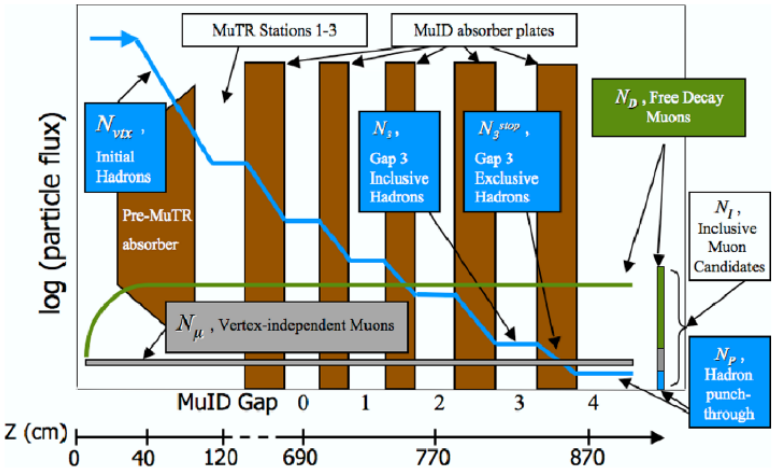

Figure 1.18: Schematic depiction of the relative flux of different components of the inclusive muon candidate yield as a function of flight path into the PHENIX muon arm absorber. [51]

A typical muon detector places heavy and thick masses (ion, copper, or lead) between the particle source and detectors as a hadron absorber. After the absorber only muons and a few high energy punch-through hadrons survive. Conventional muon detectors usually rely on multiple tracking stations to measure the muon momentum and provide particle identification ability [50]. Figure 1.18 shows an example of the PHENIX muon detector [51].

At RHIC the PHENIX Collaboration has a muon detector measuring muons at forward rapidity over $1.2< |\eta| <2.4$. Results on single muon [51] and J/Ψ [52] spectra have been reported. STAR currently does not have a muon detector. Using the energy loss in the TPC and the Time-of-Flight (TOF) detectors we can separate muons from electrons and other hadrons at low p_T at mid-rapidity (particle ID in the TPC and details of detectors can be found in Chapter 2). Single muons at low p_T from heavy flavor decays play an important role in measuring the total charm cross section [53]. Figure 1.19 shows the muon identification in STAR and its yield, which heavily constrains the fit to obtain the total charm cross section. However, at higher p_T the energy loss separation between muon and pion is reduced to 0.5σ, so this method is no longer usable. As a result, it is crucial to include muon detection to the STAR upgrade program.

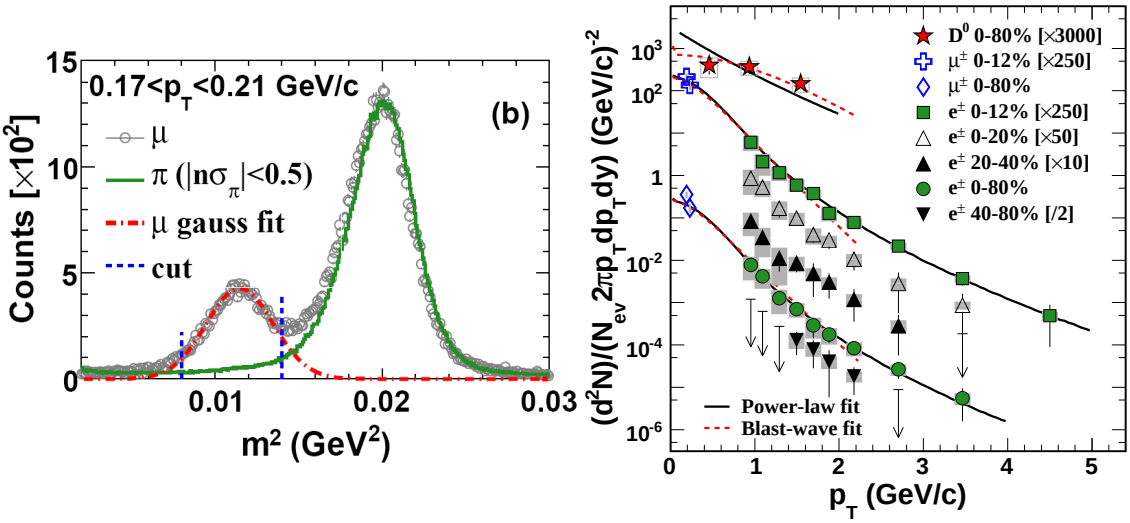

Figure 1.19: Left: Mass squared distribution $m^2 = (p/\beta/\gamma)^2$ from the Time-of-Flight (TOF) detector. Right: p_T distributions of invariant yields for D^0, charm-decayed prompt μ and non-photonic electron in different centralities of 200 GeV Au+Au collisions. Solid curves are power-law combined fit for D^0 and leptons. Dashed curves are blast-wave fit. The gray bands are bin-to-bin systematic uncertainties.

In Chapter 6 the simulation of a large-area Muon Telescope Detector (MTD) at mid-rapidity for RHIC collisions will be presented. The beam test results of the MTD prototype, the long-strip MRPC module will also be discussed.

Chapter 2

STAR Experiment

2.1 RHIC

The Relativistic Heavy Ion Collider (RHIC) at the Brookhaven National Laboratory (BNL) is currently the world's highest energy heavy-ion accelerator and the world's first and only polarized proton collider. Figure 2.1 shows the schematic view of the RHIC accelerator complex [55]. RHIC with the injector chain consist of the Tandem van de Graaff pre-accelerator, the Booster Synchrotron, the Alternating Gradient Synchrotron (AGS), the interconnecting beam transfer lines, and two independent, concentric acceleration and storage rings with a circumference of 3.8 km. Beams in the two rings are called yellow and blue beams, with the yellow beam going counter-clockwise and the blue beam going clock-wise. Storage ring magnets are superconducting. There are six intersection points of the two rings, four of which have been instrumented with experiments, STAR, PHENIX, PHOBOS, and BRAHMS. Currently PHOBOS and BRAHMS have ceased operating, and only the two bigger experiments of STAR and PHENIX are taking data.

The primary accelerating capability of RHIC [54] is heavy-ion collisions at energies up to 100 GeV/n per beam. With the magnet system set at $B\rho$=839.5 Tm for 100 GeV/n Au beams, the operational momentum increases with the charge-to-mass ratio, resulting in kinetic energies of 125 GeV/n for lighter ions and 250 GeV for protons. In other words, the top collision energy for the heaviest nuclear beams is $\sqrt{s_{NN}}$=200

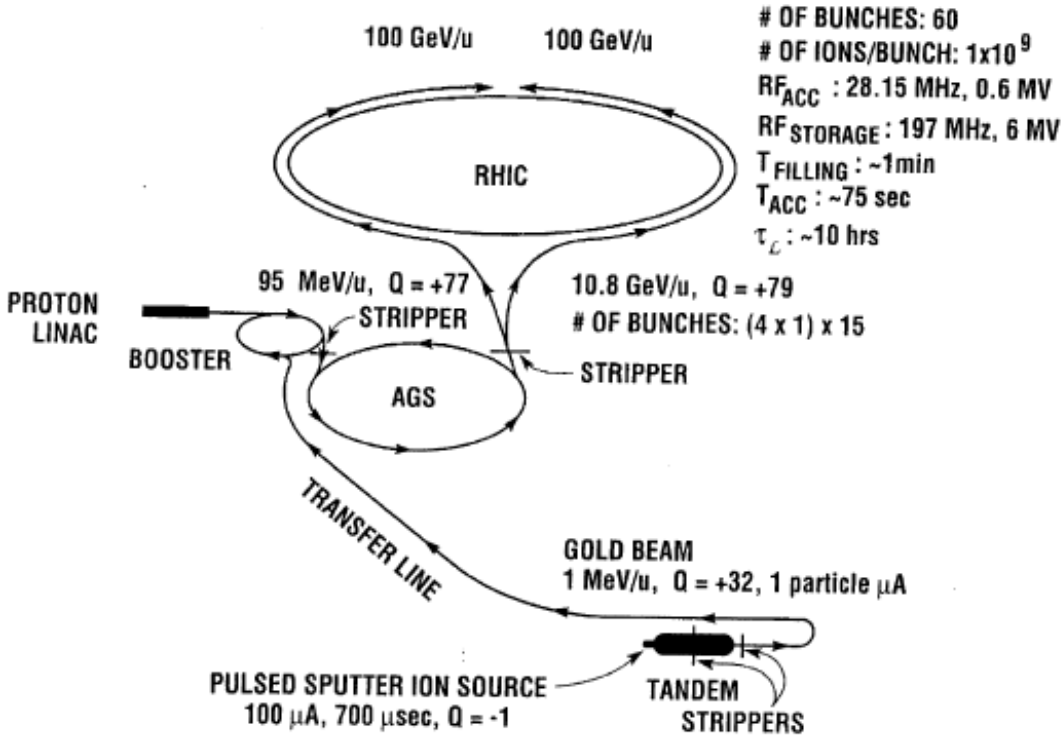

Figure 2.1: The RHIC accelerator complex.

GeV/nucleon pair, while for p+p it is $\sqrt{s}$=500 GeV. The luminosity (the number of interactions per unit time per unit cross-section) is 2×10^{26} cm^{-2}s^{-1} for 100 GeV/n Au+Au collisions averaged over the nominal 10-hour storage time.

RHIC is a very versatile accelerator which provides features unique among other hadron colliders. Firstly, thanks to the two independent ring design, it is able to collide beams of unequal species, such as protons or light ions with heavy-ions. Secondly, it provides collisions between beams of heavy-ions over a wide energy range from top energy down to injection so as to connect to previous experimental results. The luminosity is energy dependent and is approximately proportional to the operating energy. Full liminosity and lifetime requirements are specified only for energies above 30×30 GeV/n.

The acceleration scenario of the RHIC accelerator can also be seen in Figure 2.1. Here the Au beam is used as an example. Au beams originate in a pulsed sputter ion source and are accelerated by the Tandem Van de Graaff accelerator to the kinetic energy of $\sim$1 MeV/n and with Q_T=+12 charge state. When exiting from the Van de Graaff the Au-ions are further stripped to a charge state of +32. They are then transferred to the Booster synchrotron, where beams are captured into bunches and accelerated to 95 MeV/n. A foil at the Booster exit strips all atomic electrons but two tightly bound K-shell electrons. Then the Au-ion beam is filled into the AGS, de-bunched and re-bunched into final bunches, and then accelerated to 8.86 GeV/n and fully stripped. After exiting from the AGS the beam is transported to the RHIC storage rings. In the storage ring beam is stored and accelerated utilizing two Radio-Frequency (RF) systems. One, at 28 MHz, captures the AGS bunches and accelerates them to top energy, the other one, at 197 MHz, provides a short collision diamond ($\sigma_L \sim 25$ cm) to efficiently utilize the luminosity. At its required energy the yellow and blue beams are cogged (two beams are adjusted to meet at the center of detectors) and the collisions start. When the luminosity declines to an unacceptable level, typically after several hours of operation, the beam is dumped.

2.2 STAR

This section briefly reviews the design and performance of the Solenoidal Tracker at RHIC (STAR). Several detectors relevant to the analyses of this thesis are discussed, including the Time Projection Chamber (TPC), the Forward Time Projection Chamber (FTPC), and the Barrel Electro-Magnetic Calorimeter (BEMC).

2.2.1 Overview

STAR is one of the two large detector systems at RHIC. It was constructed to investigate the behavior of strongly interacting matter at high energy density and to search for signatures of the QGP. Thanks to its large acceptance and comprehensive design, STAR is able to measure many observables simultaneously and provide a most detailed and precise picture of a nucleus-nucleus collision [56]. Figure 2.2 and 2.3 show the layout and a cutaway side view of the STAR detector as configured in year 2004 RHIC run.

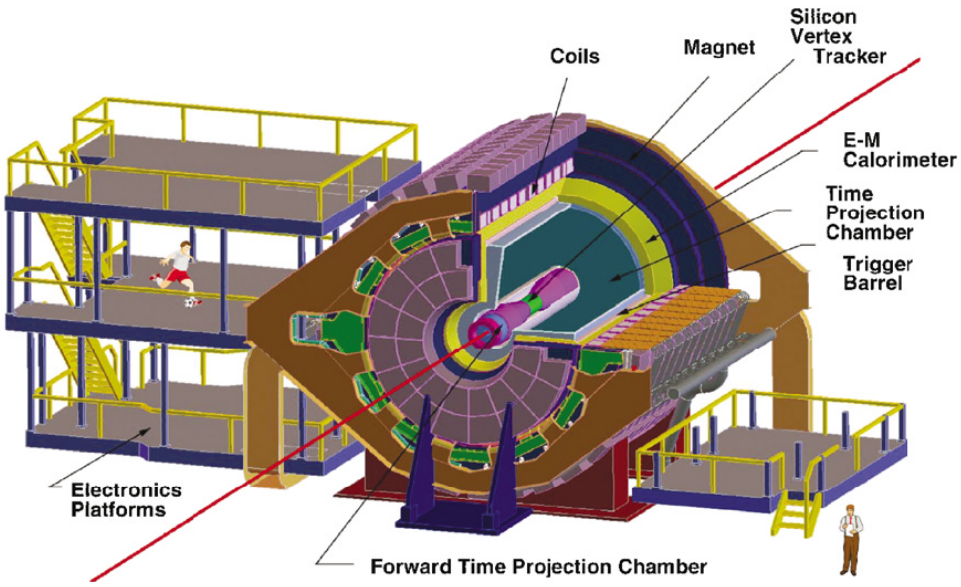

Figure 2.2: Perspective view of the STAR detector, with a cutaway for viewing inner detector systems.

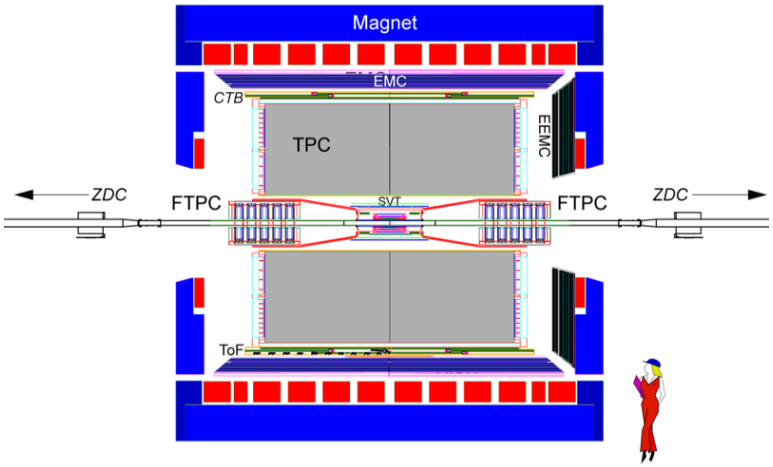

Figure 2.3: Cutaway side view of the STAR detector as configured in 2004.

From the beam pipe outward, at mid-rapidity the STAR detector system consists of the Silicon Vertex Tracker (SVT), Silicon Strip Detector (SSD), Time Projection Chamber (TPC), Central Trigger Barrel (CTB), Time of Flight detector(TOF), Barrel Electro-Magnetic Calorimeter (BEMC), and the magnet system. At forward rapidity are the Forward Time Projection Chamber (FTPC), Endcap Electro-Magnetic Calorimeter (EEMC), Photon Multiplicity Detector (PMD), Beam-Beam Counters (BBC), and Zero-Degree Calorimeter (ZDC). Details about these detectors can be found in Ref. [56].

The STAR magnet system is a room temperature solenoidal magnet wrapping most of the STAR detectors. It provides a uniform magnetic field of maximum value 0.5 T along the beam line, which curves charged particles traversing the field to allow momentum measurement. Until now, both full field (0.5 T) and half field (0.25 T) data with either magnetic field direction have been collected.

Closest to the beam pipe, the SVT and SSD provide tracking near the primary vertex covering a pseudo-rapidity range $|\eta| \leq 1$ and a complete azimuthal symmetry ($\Delta\phi = 2\pi$). Silicon tracking close to the interaction allows precision localization of the primary interaction vertex and identification of secondary vertices from weak decays, such as Λ, Ξ, and Ω.

Outside the SVT and SSD, a large volume TPC for charged particle tracking and

identification is located at a radius from 50 to 200 cm from the beam axis. The TPC is 4 m long and covers a pseudo-rapidity range $|\eta| \leq 1.8$ for tracking with complete azimuthal symmetry ($\Delta\phi = 2\pi$) apart from the gaps between the TPC 12 sectors. The TPC identifies particles via ionization energy loss dE/dx with a energy loss resolution of 7% (σ). The p_T dependent primary track momentum resolution at full field is roughly $\delta p_T/p_T = 0.0087 + 0.0045 * p_T$, with higher resolution at low p_T as the number of hit points along the track increases. To extend the tracking at forward rapidity, a radial-drift FTPC is installed covering $2.5 < |\eta| < 4$ and $\Delta\phi = 2\pi$. To further extend the particle identification capability a TOF detector covering $|\eta| < 1$ and $\Delta\phi = 2\pi$ is proposed and partially installed outside the TPC. As of 2008, 48 TOF trays are operating and a full barrel TOF will be taking data in 2009-2010 RHIC run [57]. The TOF can distinguish π from K up to 1.6 GeV/c, and protons from mesons up to 3 GeV/c. Combined with the TPC, π and proton can be identified up to 10 GeV/c and K up to 3 GeV/c [58].

Outside the TPC is a full coverage ($|\eta| < 1$, $\Delta\phi = 2\pi$) BEMC which measures electro-magnetic showers created by photons and electrons. The BEMC includes a Shower Maximum Detector (SMD) to help distinguish high momentum single photons from photon pairs from meson decays. An EEMC is installed covering $1 < \eta < 2$ to measure E&M showers in the forward direction. Another photon detector PMD is installed behind the FTPC measuring photon multiplicity at $2.5 < \eta < 3.5$.

2.2.2 Trigger system

The purpose of the STAR trigger system is to control event selection for the much slower tracking detectors, based on input from fast detectors. The STAR trigger system is divided into different layers with level 0 being the fastest and levels 1 and 2 slower but applying more sophisticated constraints. A level 3 trigger performs online reconstruction of events and provides a real time event display. It is able to process central Au-Au collisions at a rate of up to 50 Hz, including simple analysis of physics observables such as particle momentum and energy loss.

The primary fast trigger detectors of the STAR trigger system are the CTB, ZDC,

BBC, BEMC, and EEMC. The CTB is located at the same radius of the TOF and will eventually be replaced by the TOF. It consists of 240 scintillator slats in four cylindrical bands each covering 1/2 unit of pseudo-rapidity. It provides triggers based on the flux of charged particles at mid-rapidity. The ZDCs are placed in the forward direction with an acceptance of $|\theta|$ <2 mrad behind the DX magnets, which guide the yellow and blue beams away from the ZDC. They are used to determine the remaining energy of neutrons in the forward direction.

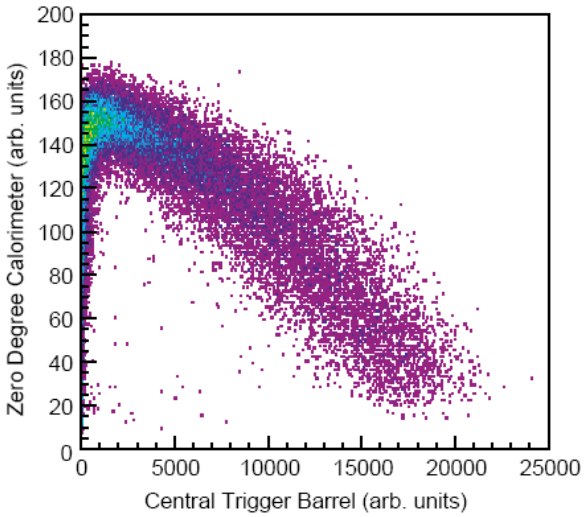

Figure 2.4: Correlation between the summed pulse heights from the ZDC and the CTB for events with a primary collision vertex successfully reconstructed from tracks in the TPC.

Figure 2.4 shows the correlation between the summed ZDC pulse height and that of the CTB for events with a primary collision vertex successfully reconstructed from tracks in the TPC for Au+Au 200 GeV events. Peripheral collisions with large impact parameters show large ZDC values and small CTB values, which indicates that they leave a large amount of energy in the forward direction into the ZDC and produce a small amount of energy and particles in the transverse direction, except the most peripheral collisions where the ZDC value gets small again. In contrast, central collisions with small impact parameters have only a small fraction of surviving neutrons, so they have less energy deposited in the forward direction and more sideward. The correlation between the CTB and ZDC can be used to provide a trigger for centrality

of the collision. A minimum bias trigger is obtained by selecting events with a pulse height larger than that of one neutron in each of the forward ZDCs, which corresponds to 95% of the geometrical cross-section. A trigger corresponding to a smaller impact parameter, which is called a central trigger, is implemented by selecting events with less energy in the forward ZDCs but with sufficient CTB signal, so as to eliminate the second branch at low CTB values.

The minimum bias and central triggers are the most commonly used triggers. Using additional fast detectors more sophisticated triggers can be implemented to enhance the collection of events with exotic particles such as high-p_T direct photons, leptons, and quarkonia. A most important trigger is the high tower trigger. It requires that one tower of the BEMC or EEMC should have energy deposited above a threshold, typically between 3 and 8 GeV. Other more complex triggers such as J/Ψ and Υ triggers have been successfully implemented.

2.2.3 Time Projection Chamber

The TPC is the central component of the STAR detector system. Covering $|\eta| < 1$ and $\Delta\phi = 2\pi$, it is the primary tracking device that reconstructs the trajectory of particles, measures their momenta, and identifies their species by measuring their ionization energy loss (dE/dx). Particles are identified over a momentum range from 100 MeV/c to greater than 1 GeV/c, and their momentum is measured over a range of 100 MeV/c to 30 GeV/c.

The STAR TPC is shown schematically in Figure 2.5. It is 4.2m long and 4m in diameter sitting in the solenoidal magnet. Filled with P10 gas (10% methane and 90% argon), it is in a uniform electric field of $\simeq$ 135 V/cm along the beam line.

The paths of primary charged particles passing through the gas are reconstructed with high precision by the released secondary electrons drifted by the electric field to the readout endcaps at the end of the chamber. The TPC readout system is based on Multi-Wire Proportional Chambers (MWPC) with readout pads. It is divided into 24 sectors, 12 one each side, with each one covering $\pi/6$ azimuthal angle. Each sector is equipped with an anode pad plane. The schematic structure of an anode pad

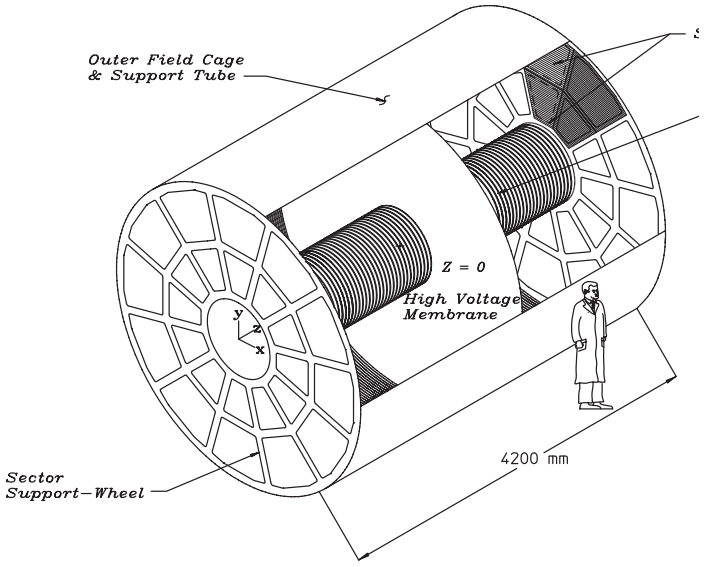

Figure 2.5: The schematic overview of the STAR TPC.

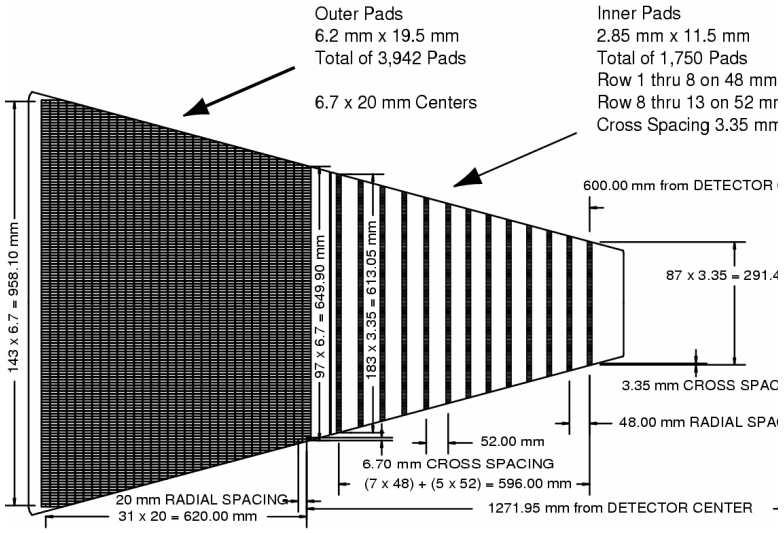

Figure 2.6: The anode pad plane with one full sector shown. The inner subsector is on the right and it has small pads arranged in widely spaced rows. The outer subsector is on the left and it is densely packed with larger pads.

plane is shown in Figure 2.6. It implements different designs in the outer and inner subsector. The outer subsectors have continuous pad coverage to optimize the dE/dx resolution; and the inner subsectors have small pads arranged in widely spaced rows. Each pad plane has three wire planes with optimized width to give the best centroid reconstructing. The wire direction is set to best determine the momentum of the highest p_T tracks, which are nearly straight radial lines from the interaction point.

The track of a particle with infinitely high momentum passing through the TPC at mid-rapidity will be sampled by 45 pad rows. Tracks with finite momenta may cross fewer pad rows, depending on the curvature of the track, pseudo-rapidity, fiducial cut near sector boundaries, and other details of the particle's trajectory. A track is reconstructed by finding ionization clusters along it. The clusters are found separately in $x+y$ and in z spaces. Here the local x-axis is along the direction of the pad row, and y-axis extends from the beamline outward through the middle of, and perpendicular to the pad rows. The z-axis is along the beam line.

The x and y coordinates are determined by the charges measured on adjacent pads in a single pad row. A Gaussian approximation or a weighted mean algorithm is used. The z coordinate of a point inside the TPC is determined by measuring the time of drift of a secondary electron cluster from its origin (assumed to occur at the beam crossing time) to the endcap, multiplied by the average drift velocity. The drift velocity, which is typically 5.45 cm/μs, is measured independently every few hours using tracks created by laser beams. The energy collected by all pads is summed to give the total ionization in the cluster. The position resolution depends on the drift distance and momentum. Typical position resolution in z direction is 0.5-3 mm with best resolution for small drift distance and small dip angle between the track momentum and drift direction.

After the hits are reconstructed, the tracking software associates space points to reconstruct tracks and fits those points with a tracking model to extract information such as momentum. To first order the tracking model is a helix, and to second order the energy loss in the gas and detector materials is included. The tracking efficiency depends on the TPC acceptance, momentum, and track multiplicity. To estimate the tracking efficiency, we embed TPC hits associated with simulated tracks inside

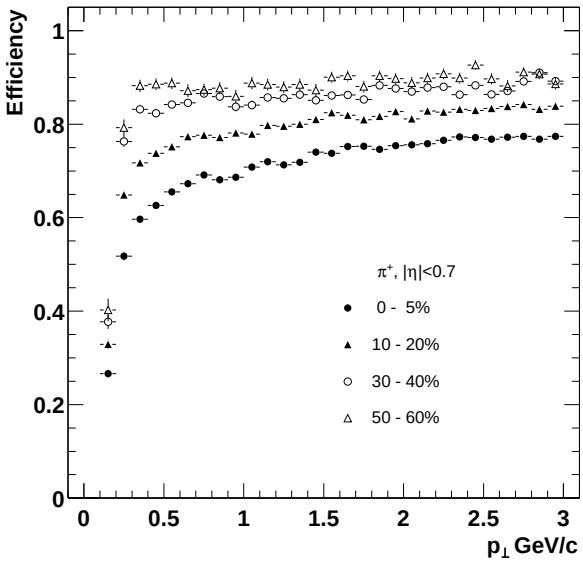

Figure 2.7: The pion tracking efficiency in STAR for Au+Au events at $\sqrt{s_{NN}} = 130$ GeV at RHIC. Tracks with $|y|$ <0.7 are used and the magnetic field is set to 0.25 T.

real events and measure the fraction of these tracks which are reconstructed by the tracking software. The technique allows us to take into account detector effects and the loss due to high track density and energy loss. Figure 2.7 shows the π^+ tracking efficiency within $|y|$ <0.7 and B=0.25 T in different centralities of Au+Au collisions. In central events with highest multiplicity it reaches a plateau of 80% for high p_T particles. Efficiency goes up to ∼90% for more peripheral events.

The primary vertex for an event is calculated by considering all the tracks reconstructed in the TPC for that event and extrapolating them back to the beam line. The global average is the estimate of the vertex position. The resolution scales with the square root of the number of tracks used in the calculation. A resolution of 350 μm is achieved when there are more than 1000 tracks.

The p_T of a primary track is determined by fitting a circle through the primary vertex and points along the projection of the track on the $x + y$ plane. Using the primary vertex significantly improves the p_T resolution due to the precise determination of the primary vertex. For particles from secondary decays, the circle fit is done without reference to the primary vertex. At low p_T, charged particles suffer from multiple Coulomb scattering; and at high p_T, resolution is limited by the strength of

the magnetic field and the TPC spatial resolution. The best relative p_T resolution falls between these two extremes and is ∼2% for pions at p_T ∼400 MeV/c.

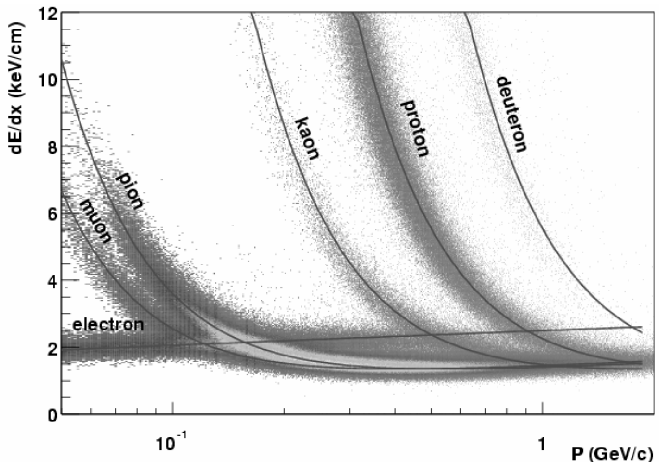

Figure 2.8: The energy loss per unit length distribution for primary and secondary particles in the STAR TPC as a function of primary momentum. The magnetic field is 0.25 T.

Energy loss in the TPC gas is a valuable tool for identifying particles. It works well for low momentum particles, but dE/dx becomes less mass dependent as particle energy rises, so that it is hard to separate particles with velocity $v > 0.7c$. The relative dE/dx resolution of the TPC is 7%, and we are able to separate π and proton up to 1 GeV/c. The dE/dx is extracted from energy loss measured by up to 45 pad-rows, where the most probable energy loss is obtained. One method of averaging is by removing the largest 30% ionization clusters to avoid the high-end fluctuations of energy loss. Another way is to fit the dE/dx distribution including all clusters associated to a given track. Figure 2.8 shows the energy loss for particles in the TPC as a function of momentum. The 70% truncated mean is used, and the magnetic field is 0.25 T. The resolution is 8% for a track crossing 40 pad-rows. At 0.5 T the dE/dx resolution improves to 7% due to smaller transverse diffusion. Here bands of different particles are well separate at low momentum, which provides useful PID information in various analyses.

One of the most useful parameters is $N_{\sigma x}$ which describes the deviation from the

mean energy loss assuming particle type x. In case of π it is defined as

$$N_{\sigma\pi} = [\frac{dE}{dx}\Big|_{meas.} - \langle\frac{dE}{dx}\rangle_{\pi}]/[\frac{0.55}{\sqrt{N}}\frac{dE}{dx}\Big|_{meas.}], \tag{2.1}$$

where N is the number of hits for a track in the TPC, $\frac{dE}{dx}\big|_{meas.}$ is the measured energy loss of a track and $\langle\frac{dE}{dx}\rangle_{\pi}$ is the mean energy loss for $\pi^{\pm}$ described by the Bethe-Bloch formula [59]

$$\begin{aligned} \frac{dE}{dx} &= Kz^2\frac{Z}{A}\frac{1}{\beta^2}[\frac{1}{2}\ln\frac{2m_ec^2\beta^2\gamma^2T_{max}}{I^2} - \beta^2 - \frac{\delta(\beta\gamma)}{2}] \\ K &= 4\pi N_A r_e^2 m_e c^2, \end{aligned} \tag{2.2}$$

where N_A is the Avogadro's number; $r_e = \frac{e^2}{4\pi\epsilon_0 m_e c^2}$ is the classical electron radius; m_e is electron mass; z is the charge of incident particle; Z and A are the atomic number and mass of absorber; $\beta = v/c$ and $\gamma = \frac{1}{\sqrt{1-\beta^2}}$ are the velocity parameters of incident particle; T_{max} is the maximum kinetic energy which can be imparted to a free electron in a single collision; I is the mean excitation energy; and $\delta(\beta\gamma)$ is the density effect correction to ionization energy loss. Similar parameters can be defined for K, p, and e. By cutting a range of the $N_{\sigma x}$ we can select particles with a purity that depends on momentum.

2.2.4 Forward TPC

The FTPC was constructed to extend the acceptance of the STAR experiment, covering $2.5 < |\eta| < 4$ and $\Delta\phi = 2\pi$. The increased acceptance improves the general event characterization in STAR and also allows the study of asymmetric systems such as $p + A$ collisions.

A schematic view of the FTPC is shown in Figure 2.9. The FTPC is a cylindrical structure 75 cm in diameter and 120 cm long. It has a radial drift field and readout chambers located in five rings on the outer cylinder surface. Each ring has two pad-rows and is subdivided azimuthally into six readout chambers. The radial drift configuration is chosen to improve the two track separation close to the beam pipe where particle density is highest. In addition, curved readout chambers are used to keep the radial field as ideal as possible. Thanks to these two features, a two-track

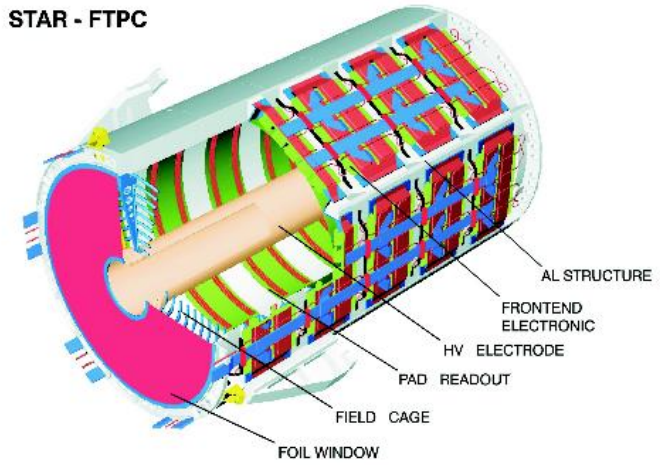

Figure 2.9: Schematic diagram of an FTPC for the STAR experiment.

separation of 1-2 mm is measured, which is an order of magnitude better than all previously built TPCs with pad readout. An $Ar/CO_2(50\%/50\%)$ mixture is selected as working gas. A laser calibration system serves to calibrate the drift velocity and correct for spatial distortions.

Each particle trajectory is sampled up to 10 times. The ionization electrons are drifted radially to the anode sense wires, then induced signals on the adjacent cathode surface are read out by part of the 9600 pads in total. The track reconstruction is similar to the TPC. The track points are calculated from the charge distribution measured by the readout electronics. These track points are grouped into tracks. Up to 10 position measurements per track are used to fit the momentum. Based on the prototype measurement and simulation, the FTPC is expected to obtain a position resolution of 100 μm; a two-track-separation of 1 mm; a momentum resolution between 12% and 15%, and an overall reconstruction efficiency between 70% and 80%.

2.2.5 Barrel Electromagnetic Calorimeter

The BEMC is STAR's major detector for measuring E&M signals. STAR utilizes the BEMC to trigger on, and study, rare and high p_T processes such as jets, leading hadrons, direct photons, and heavy quarks. It also provides large acceptance for measuring photons, electrons, π^0 and η mesons in systems spanning from polarized $p+p$ through Au+Au collisions.

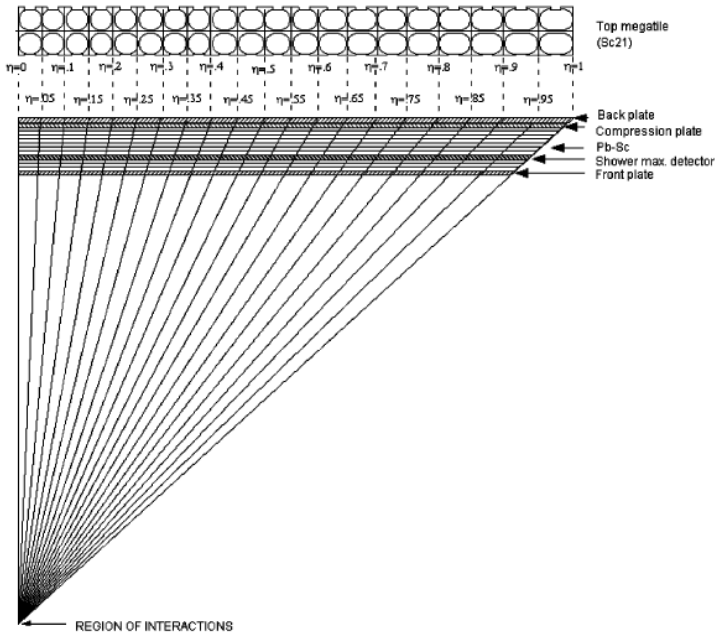

Figure 2.10: Side view of a calorimeter module showing the projective nature of the towers.

Figure 2.10 shows the side view of the STAR BEMC. The STAR BEMC is a lead-scintillator sampling calorimeter. It covers $|\eta| \leq 1.0$ and 2π in azimuthal. The front face is at a radius of 220 cm from, and parallel to, the beam axis. The design includes 120 calorimeter modules, each subtending 6° in $\Delta\phi$ and 1.0 unit in $\Delta\eta$. Modules are mounted 60 in ϕ and by 2 in η. Each module is segmented into 40 towers, 2 in ϕ and 20 in η, with each tower subtending 0.05 in $\Delta\phi$ by 0.05 in $\Delta\eta$.

Figure 2.11 shows the side view of a STAR BEMC tower. It consists of a lead-scintillator stack and a Shower Maximum Detectors (SMD) situated at approximately 5 radiation lengths (X_0) from the front of the stack. There are 20 layers of 5 mm

thick lead, 19 layers of 5 mm thick scintillator, and 2 layers of 6 mm thick scintillator. The latter thick ones are used in the preshower portion of the detector.

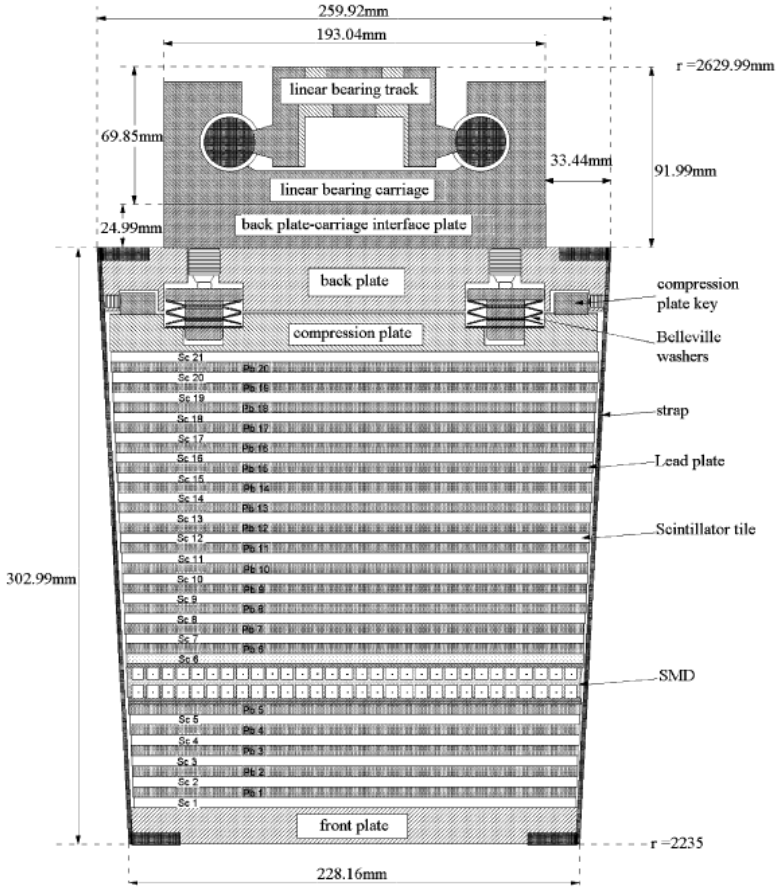

Figure 2.11: Side view of a STAR BEMC tower. The location of the two layers of shower maximum detector at a depth of approximately $5X_0$ from the front face at η=0 is also shown.

The Barrel SMD detector is used to provide fine spatial resolution in the BEMC which has granularity of towers significantly larger than an electromagnetic shower. A STAR BEMC tower has a front-face size of $\sim 10 \times 10$ cm^2 at η=0 and it increases towards η=1. The high spatial resolution provided by the SMD is essential for π^0, direct γ, and electron identification. For example, the separation between two photons from a high p_T π^0 decay can be smaller than the front-face dimension of a BEMC tower. They may hit the same tower, which by itself can not distinguish them, and we

have to rely on the SMD. In this sense, the SMD significantly enhances the versatility of the STAR BEMC.

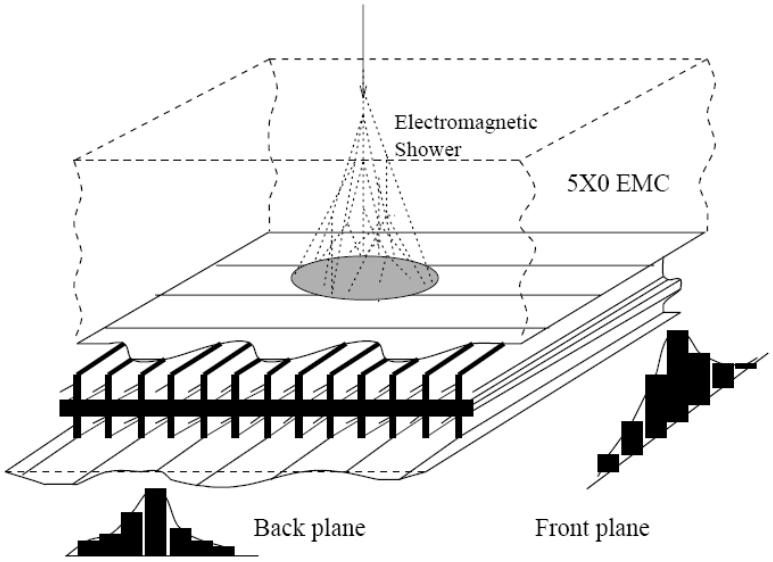

Figure 2.12: Schematic illustration of the double layer STAR BEMC SMD.

The SMD is a wire proportional counter-strip readout detector using gas amplification. Figure 2.12 shows a schematic illustration of the STAR SMD. A unique feature of the STAR SMD is its double layer design. Two planes with strips etched in the η and ϕ directions allow reconstruction of a two-dimensional image of the shower as shown in the figure. There are a total of 36000 strips in the full detector and 120 wire channels. Each of the 1200 distinct areas, approximately 0.1 by 0.1 in $\Delta\eta - \Delta\phi$, has 15 ϕ strips and 15 η strips. So each SMD strip has a width of 0.0067 in $\Delta\phi$ and $\Delta\eta$ directions.

When a photon or an electron enters the BEMC, it creates an electro-magnetic shower. The shower develops on average to its maximum transverse profile at $\sim 5X_0$, whose position is measured by the SMD. As the shower travels through the BEMC tower, it loses energy in the lead layer and is sampled in the scintillator layer, in which roughly 5% of the total energy is lost. Signals from each of 21 active scintillating layers are read out with a wavelength shifting fiber and are transferred and merged onto a single photomultiplier tube (PMT). As a result, the signal magnitude of the PMT

is proportional to the sampled fraction of the shower, which is proportional to the energy of the incident photon or electron. With a well calibrated gain controlled by the high voltage, the particle energy can be precisely measured. Hadrons within a certain momentum range usually deposit minimal ionizing energy into the BEMC towers, which are known as Minimum Ionizing Particles (MIP), but they also possibly create hadronic showers and deposit significant amount of energy. The mean hadronic background energy in any given BEMC tower in a central Au+Au event is in the order of 140 MeV/tower with a standard deviation of 170 MeV. Energy loss from electrons and MIPs are two major ways used to calibrate the BEMC towers. High voltage of each tower is adjusted according to the calibration from early runs and fixed in the remaining time of the data collection, so that the size of the MIP signal in each tower will be roughly the same.

Layer by layer tests of the BEMC optical signal, and full system tests with cosmic rays and the test beams show that an average of 3 photoelectrons per MIP per calorimeter layer are produced from the fully integrated optical system. For these photostatistics, the resolution of an ideal sampling calorimeter is expected to be $\approx 14\%/\sqrt{E}$ plus a 1.5% constant term added in quadrature. In a real sampling calorimeter, transverse and longitudinal non-uniformities within a tower, and cross talk between towers, are the limitations to achieving this limiting resolution. The measured resolution is roughly $16\%/\sqrt{E} \oplus 1.5\%$.

The SMD has also been extensively evaluated in test beams at the AGS. In the energy range from 0.5 to 5 GeV, at a depth of $5X_0$ inside the BEMC it has an approximately linear response versus energy. The ionization at the back plane of SMD is about 10% lower than the front plane. The energy resolution in the front plane is given approximately by $\sigma/E = 12\% + 86\%/\sqrt{E}[GeV]$ with the energy resolution on the back plane being 3-4% worse. The position resolution in the front and back planes of the SMD have been measured in test beams. They are found to be approximately

$$\sigma_{front} = 2.4\text{mm} + 5.6\text{mm}/\sqrt{E}[\text{GeV}]$$

and

$$\sigma_{back} = 3.2\text{mm} + 5.8\text{mm}/\sqrt{E}[\text{GeV}].$$

Chapter 3

Neutral Pion Production

3.1 Neutral pion reconstruction techniques

In this section the π^0 reconstruction techniques at mid-rapidity in STAR are discussed. A π^0 is reconstructed via the di-photon decay channel. Photons are detected directly in the STAR BEMC or reconstructed through their conversion electrons in the TPC. Finally, raw π^0 yields from the di-photon invariant mass distributions are presented.

3.1.1 Data set

The data presented in this analysis are Au+Au events taken during the year 2004 RHIC run at the energy of $\sqrt{s_{NN}} = 200$ GeV using the STAR TPC and BEMC. Events collected with three different triggers are analyzed. After event selection, they include 11×10^6 events selected by a minimum-bias trigger (MB), 17×10^6 events selected by a central trigger, and 2.4×10^6 events selected by a high tower trigger (HT). [1]

In Au+Au collisions, the minimum bias trigger is defined by requiring greater than 75 CTB counts and coincidence between the two ZDCs which measure the spectator neutrons. CTB counts fewer than 75 together with coincidence between two ZDC's defines an Ultra-Peripheral Collision (UPC) trigger. The central trigger corresponds to the top 12% of the total cross section, which requires greater than 3500 CTB

[1] Technical note: The trigger ID's for MB, central, and HT events are 15007, 15105, and 15203, respectively.

Centrality Bin	RefMult	N_{bin}
0-20%	RefMult≥319	765.5±61.5
20-40%	150≤RefMult<319	294.2±40.5
40-80%	14≤RefMult<150	57.1±13.5

Table 3.1: The definition of different centrality bins in 200 GeV Au+Au collisions with their reference multiplicity ranges and N_{bin} calculated in the Glauber model.

counts, plus the sum of east and west ZDC counts less than 130, and the Beam-Beam Counter (BBC) [60] measured vertex position in z axis within ±15 cm. The HT trigger, besides requiring a MB trigger, requires that at least one BEMC tower has energy deposited greater than the HT threshold. Here the HT trigger threshold is $E_T = E * \sin\theta > 3/\sin\theta$ GeV, where θ is the polar angle of the tower with respect to the detector center [61]. The HT trigger setup looks a little bit strange due to a mistake in the HT trigger setup when data was collected, where an additional $\sin\theta$ was introduced.

In STAR the Au+Au data sample is divided into different centrality bins according to the uncorrected reference multiplicity (RefMult), which is defined as the number of charged primary tracks with distance of closest approach (DCA) less than 3 cm from the primary vertex, and with at least 10 TPC fit points in a pseudo-rapidity range of $|\eta| < 0.5$. Figure 3.1 shows the reference multiplicity distribution from MB, central, and HT triggered events. In this π^0 analysis, the data sample is divided into 3 finer 0-20%, 20-40%, and 40-80% centrality bins, with the smaller number representing the more central collisions. Table 3.1 shows the range of reference multiplicity for each centrality bin, as well as the corresponding N_{bin} calculated in the Glauber model [61].

The event primary vertex position has a broad distribution in the z axis. In this analysis, a requirement of vertex position within ±20 cm of the beam center is used. The reason for a tight vertex cut is to avoid the regions of SVT and SSD in the forward direction with complex structures, which are difficult to describe in GEANT detector simulations and may introduce large systematic uncertainty to the calculation of photon conversion probability. After the event vertex cut, the event vertex distribution along the z axis is shown in Figure 3.2.

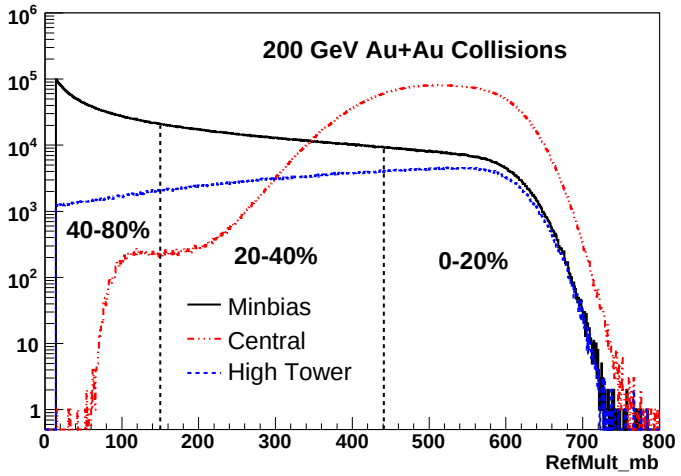

Figure 3.1: The uncorrected reference multiplicity distribution for MB, central, and HT triggered Au+Au collision at $\sqrt{s_{NN}}$=200 GeV. The three centrality regions used in this analysis are shown.

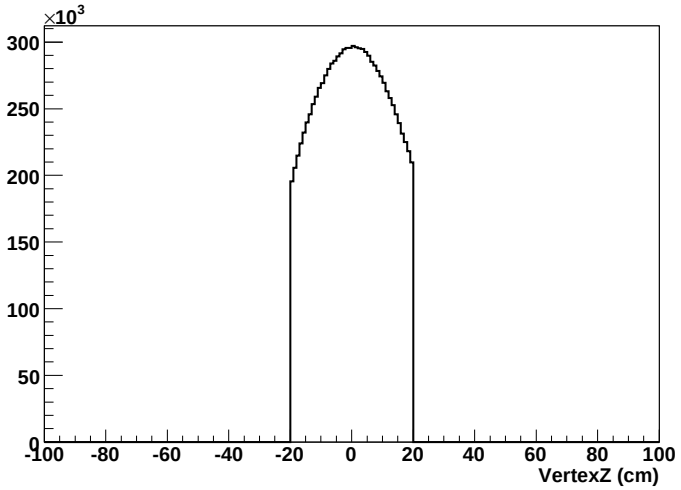

Figure 3.2: The vertex position distribution in z axis after the event cut from MB Au+Au collisions at $\sqrt{s_{NN}}$=200 GeV.

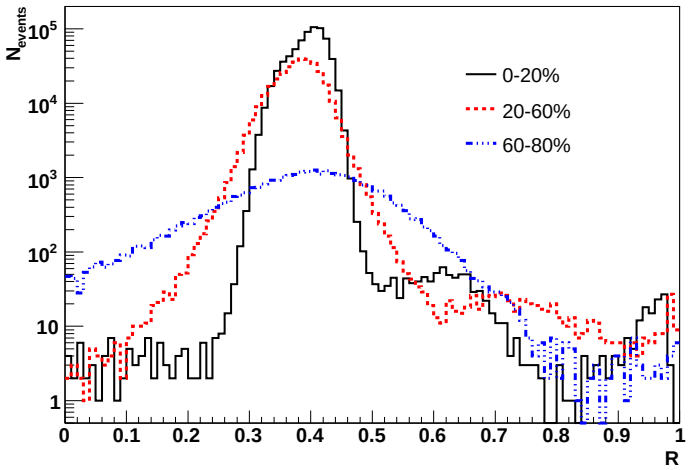

Figure 3.3: The distribution of the ratio of $R = \frac{E_{BEMC}}{E_{BEMC}+E_{TPC}}$ in 200 GeV Au+Au collisions.

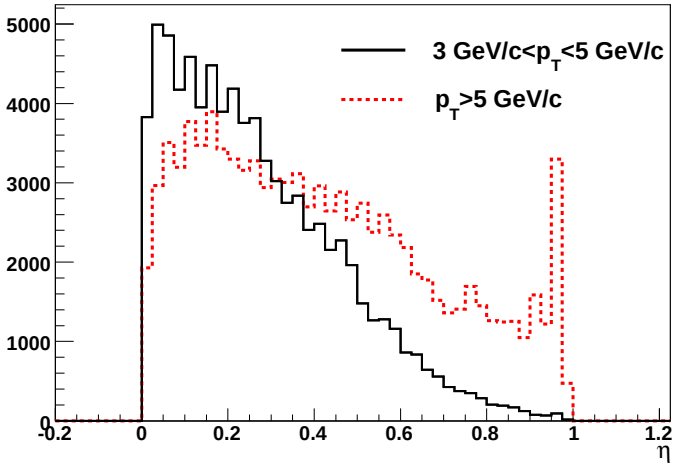

Figure 3.4: The distribution of towers as a function of η in the BEMC with photon p_T >5 GeV/c and $3 < p_T < 5$ GeV/c. Beam background contamination can be seen at η ∼1.

For the HT trigger events, additional cuts are used to remove the beam background. Beam background means events or signals acquired by detectors but not created by real collisions. Firstly, events with high energy deposited in the calorimeter, but almost no signal in the TPC are removed. These fake events especially contaminate the high tower trigger. We require that the ratio $R = \frac{E_{BEMC}}{E_{BEMC}+E_{TPC}}$ is less than 0.8, where E_{BEMC} and E_{TPC} are total particle energy detected in the BEMC and TPC. The distributions of R for different centralities are shown in Figure 3.3. It turns out that it is not a big effect for Au+Au collisions. Secondly, we find that the distribution of high energy towers has an abnormal peak structure in the most forward region, as shown in Figure 3.4, which is possibly created by the beam halo hitting the forward towers. As a result, we only accept photons with $0 < \eta < 0.9$ with respect to the detector center.

3.1.2 BEMC photon reconstruction

In this analysis, neutral pions are reconstructed via their di-photon decay channel. The STAR BEMC is designed to precisely detect the photon signals. In the following, photons reconstructed by the BEMC will be called "EMC photons". With a Moliere radius of about 2 cm for electromagnetic showers in the STAR BEMC and the relatively large BEMC tower size (10×10 cm^2), the photon energy is typically deposited into a single tower. By including neighboring towers we can avoid energy leaking, and in principal, achieve better energy resolution, but it may also introduce background from other particles, which is a more serious problem, especially for low p_T photons. Therefore, EMC photons are reconstructed from a single tower. The photon energies are determined by the tower energies. In MB and central events we only select peak towers as photon candidates, requiring that they have energy of greater than 500 MeV and at least 250 MeV higher than any of their eight neighboring towers. We don't require any SMD hits due to their low efficiency for low energy photons, and it has been found that simulation does not reproduce the SMD response well (the reason is not well understood). The photon position is assumed to be at the tower center. In HT events, SMD hits are required to separate the two close decay photons from a

single π^0 decay. The photon positions are determined from two SMD hits. Each SMD hit is a SMD cluster of 2-5 SMD strips. If multiple photons are found in the same tower, the tower energy is split in proportion to the individual SMD hit energies. Hot towers are removed from EMC photon candidates. A "hot" tower has unusually high event-averaged energy deposition which is due to malfunctioning of electronics. [2]

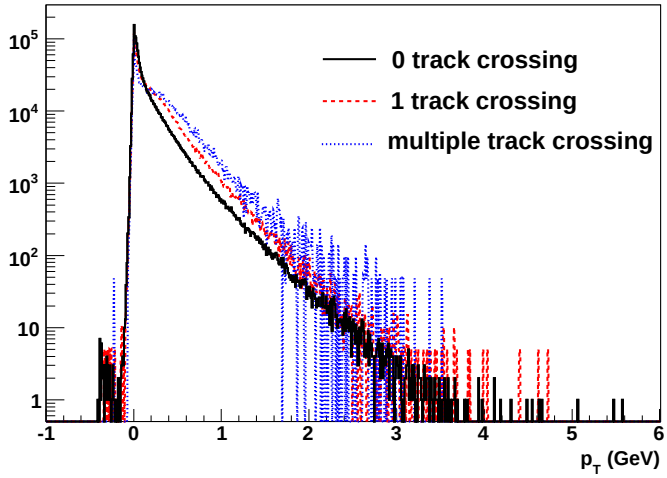

Figure 3.5: Energy distribution of towers with different numbers of tracks intersected inside the BEMC but not directly hit by any track.

Charged particles can also deposit energy into the BEMC by ionization energy loss and hadronic interaction. Such contamination should be removed for π^0 reconstruction. In MB and central events, TPC tracks are projected into the BEMC assuming a helix in the TPC, and a straight line after entering the BEMC. In the BEMC the track is extrapolated from its entering point and momentum. The first two towers intersected by the track are vetoed as contaminated towers. This cut was determined by a GEANT simulation using HIJING event generator [62]. It revealed that if we only veto the first tower hit directly by a charged track, 65% of the energy deposited in the BEMC by charged particles is removed, still leaving a significant amount of residual energy. Vetoing the first two towers can raise the percentage to 85%, but further increasing the number of towers vetoed does not significantly help removing

[2]Technical note: The list of hot towers with soft tower id is {875, 897, 1400, 1420, 2219, 2339}.

more contamination [63]. Studies using real data also indicate the necessity of this cut. Figure 3.5 shows the tower energy distributions for towers not directly hit but intersected by different numbers of TPC tracks. Charged particle contamination is clearly seen by the bump at $\sim$0.4 GeV/c when a tower is intersected by tracks inside the BEMC, even though not directly hit. Removing these towers helps suppress the fake photon signals. For central Au+Au collisions, this charged particle veto cut rejects roughly 50% of all towers.

In HT triggered events, different veto cuts are applied to photons with different energies. For a photon with energy below the HT threshold, we require that no TPC track is projected into an area of $\pm$ 0.05 in η and $\pm$ 0.05 in ϕ around the photon candidate, again assuming a charged track as a helix in the TPC. For a photon above the HT threshold, we loosen the cut so that the total momentum of tracks projected to the same area is less than 1 GeV/c. By sacrificing some photon energy resolution we can increase the efficiency of detecting high energy photons by a factor of 2. The charged particle contamination is relatively small compared to the high energy photons.

3.1.3 TPC conversion photon reconstruction

STAR is able to reconstruct photons converted in materials such as the SVT, SSD, and TPC gas by detecting the daughter e^+/e^- pairs in the TPC. Photons reconstructed using this method will be called "TPC photons" in the following. The photon conversion probability as a function of p_T from simulation is shown in Figure 3.6. In total these materials are equivalent to about 10% of a radiation length.

A schematic view of a photon conversion is shown in Figure 3.7 [64]. TPC photons are reconstructed as follows. Global e^+/e^- track candidates are selected via ionization energy loss dE/dx and other quality cuts in the TPC. Then a number of geometrical cuts are applied to each e^+/e^- pair, requiring a topological signature of a photon conversion. It is required that the two tracks originate from a common secondary vertex within, or before entering, the TPC with a small opening angle and small invariant mass, and that the reconstructed photon candidate's momentum has

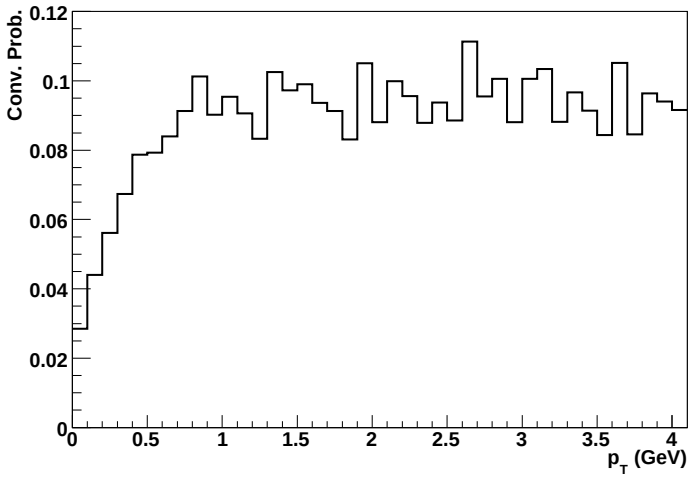

Figure 3.6: Photon conversion probability vs. p_T from simulation.

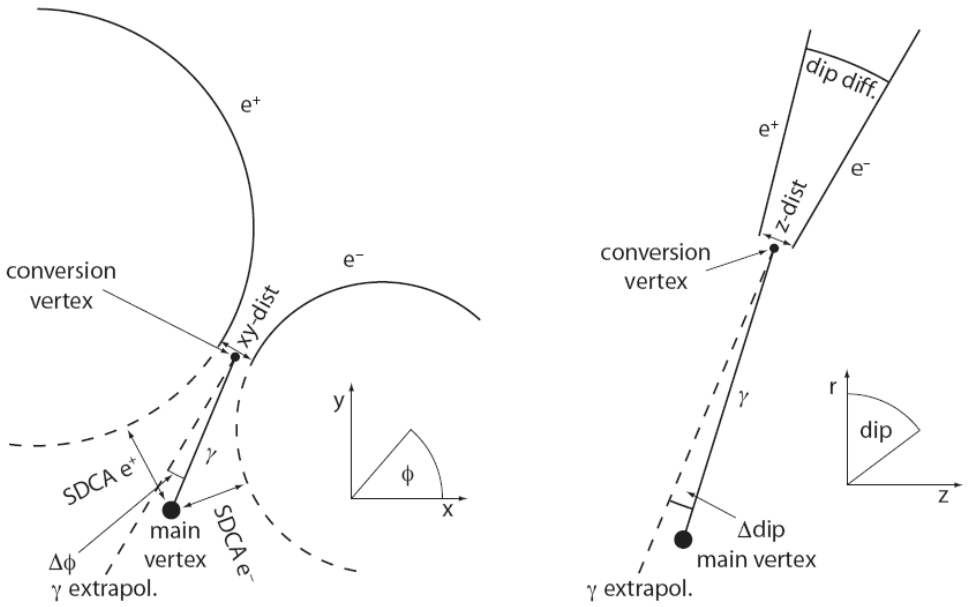

Figure 3.7: Schematic view of a photon conversion in the xy-plane and rz-plane. Figure is taken from Ref. [64].

Selection	Cut	Description
e^+/e^-	$N_{fit} > 12$	Number of fit points in the TPC
	$\frac{N_{fit}}{N_{poss}} > 0.55$	Ratio of number of fit points over number of max. possible fit points
	$-2 < N_{\sigma e} < 4$	$N_{\sigma e}$ selecting e^+/e^-
	SDCA> 0 if $p_T < 0.3$ GeV/c	SDCA = distance between primary vertex and track helix center in xy-plane - track helix radius
photon	DCA$_{xy} < 1.5$ cm	Distance of closest approach (DCA) between e^+ and e^- in xy-plane
	DCA$_z < 1.2$ cm	DCA between e^+ and e^- in rz-plane at conversion point
	$\alpha_{dip} < 0.03$ rad	Dip angle difference in rz-plane between e^+ and e^- at conversion point
	$\Delta dip < 0.035$ rad	Dip angle difference between photon momentum and vector from primary vertex to conversion point
	$\Delta\phi < 0.05 rad$	ϕ difference between photon momentum and vector from primary vertex to conversion point
	$m_{e^+e^-} < 12$ MeV/c^2	Invariant mass of e^+ and e^- pair
	$\lvert\eta_\gamma\rvert < 0.7$	Pseudo-rapidity of photon

Table 3.2: Cuts used to select e^+/e^- tracks and photon candidates.

the same direction as the conversion point from the primary vertex. The photon momentum is taken to be the sum of two daughter tracks' momenta at the conversion point.

Table 3.2 lists the cuts used to select e^+/e^- tracks and photon candidates. For the e^+/e^- track selection, the N_{fit} and $\frac{N_{fit}}{N_{poss}}$ cuts ensure that a track has enough valid fit points in the TPC to achieve good momentum resolution, and that it is unlikely to be a split segment of another track. The $N_{\sigma e}$ cut selects e^+/e^- by energy loss. The asymmetry of the cut is due to different levels of contamination on two sides of the electron dE/dx band, with more π contamination on the negative side at the most populated p_T range (see Figure 2.8). The dE/dx cut is still quite loose to accept as many e^+/e^- candidates as possible ($\sim$98%). The photon selection mainly relies on the later tight geometry cuts. The SDCA cut removes tracks that can not originate from photon conversion. At the conversion point daughter e^+/e^- tracks should have momenta roughly parallel to the vector from the primary vertex to conversion point.

For low p_T e^+/e^- tracks, due to their large curvature, the primary vertex should sit outside their helices in the xy-plane, as shown in Figure 3.7. For higher p_T tracks, their trajectories are straightened and the SDCA cut is no longer as useful due to the lower DCA resolution. So for $p_T > 0.3$ GeV/c, the SDCA cut is not used.

For the photon selection, the DCA_{xy} and DCA_z cuts require that two tracks should be close enough to each other at the conversion point. At the conversion point, we assume that two daughter tracks have parallel momenta in the xy-plane. So in the xy-plane, the conversion point is on the line connecting the centers of two helices ($\overrightarrow{x}_a$ and $\overrightarrow{x}_b$). It is calculated as

$$\overrightarrow{x}_c = (\overrightarrow{x}_a r_b + \overrightarrow{x}_b r_a)/(r_a + r_b), \tag{3.1}$$

where r_a and r_b are the radii of two helices. The points closest to the conversion point in the xy-plane on both tracks are found, and the average of their z coordinates is the z coordinate of the conversion point. The cut of dip angle difference in the rz-plane at the conversion point ensures small opening angle between two daughter tracks. The Δdip and $\Delta\phi$ cuts require that the reconstructed photon should emit from the primary vertex. The slightly different cut thresholds in the xy and rz-planes (1.5 vs. 1.2 cm, and 0.035 vs. 0.05 rad) are due to different spatial and angular resolutions in the two planes. The invariant mass cut is applied because photons have zero mass. The invariant mass is calculated as

$$M_{inv} = \sqrt{(E_1 + E_2)^2 - (p_1^2 + p_2^2 + 2p_1 p_2 \cos(\alpha))}, \tag{3.2}$$

where the opening angle between two daughter tracks $\alpha = \alpha_{dip}$, because they are assumed to be parallel in the xy-plane. Finally the η_γ constraint is to avoid the complex structure of the SVT and SSD in the forward direction.

The spatial distribution of conversion points vividly presents the material distribution inside the STAR detector, as shown in Figure 3.8. Most of the conversions happen in the SVT and SSD which have materials of high density. A peak at $r \sim$45 cm indicates the position of the TPC inner field cage. Twelve sectors are clearly seen in the TPC, and only a small fraction of conversions happen in the TPC gas.

The technique of reconstructing conversion photons has been successfully implemented in 130 [65, 66] and 62.4 [64] GeV Au+Au collisions. Cuts used in this analysis

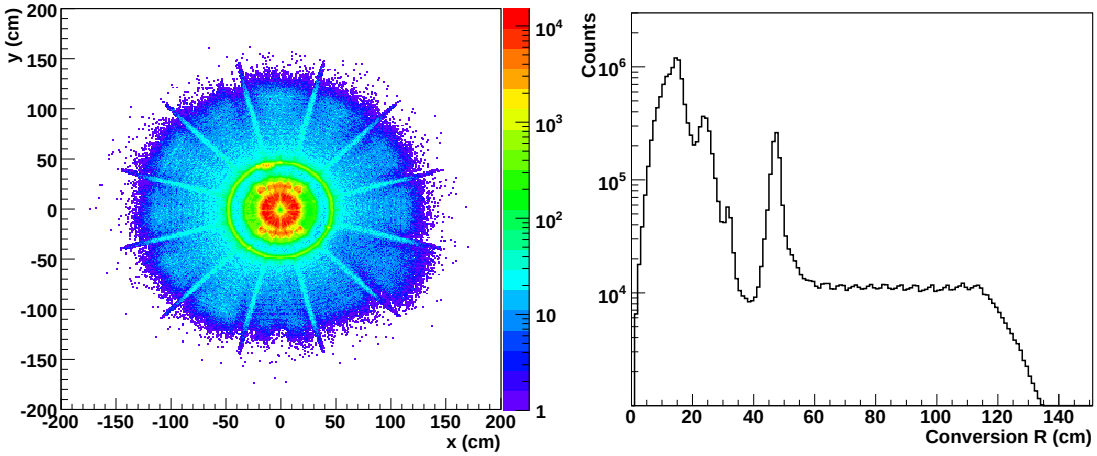

Figure 3.8: Left: Conversion point spatial distribution inside the STAR detector. Right: Conversion point radial distribution.

are largely inherited from earlier studies. More details about this technique can be found in the corresponding references.

3.1.4 Di-photon invariant mass

After photons are reconstructed, every two photons are paired and their invariant mass distribution is calculated as

$$M_{inv}^{\gamma\gamma} = 2\sqrt{E_1 E_2}\cos(\theta/2), \tag{3.3}$$

where E_1 and E_2 are photon energies, and θ is their opening angle. If two photons from a single π^0 decay are paired, they should give a signal at the π^0 mass value of 135 MeV/c^2. However, most of the pairs are random combinations, so the π^0 signal can easily be overwhelmed by the combinatorial background. In order to obtain a clear π^0 signal, the same-mixed event technique [67] is employed to remove the combinatorial background. In this procedure, photons from the same event are paired and create a "same-event" invariant mass distribution; and photons from different events are paired and create another "mixed-event" distribution. Due to the lack of decay correlation in mixed-event photon pairs, it only reproduces the combinatorial background of the

same-event distribution. Subtracting the mixed-event distribution from the same-event distribution with proper normalization reveals the π^0 signal. The normalization issue will be discussed in more detail later. Figure 3.9 shows an example of same-event distribution overlapped with the mixed-event distribution in 2.5-3.5 GeV/c p_T bin in 0-80% centrality using EMC-TPC method (will be discussed later). They are normalized in the invariant mass region of [0.5, 1.0] GeV/c^2. Their ratio is also shown in the right panel, which indicates how well the mixed-event distribution can reproduce the background in the same-event distribution.

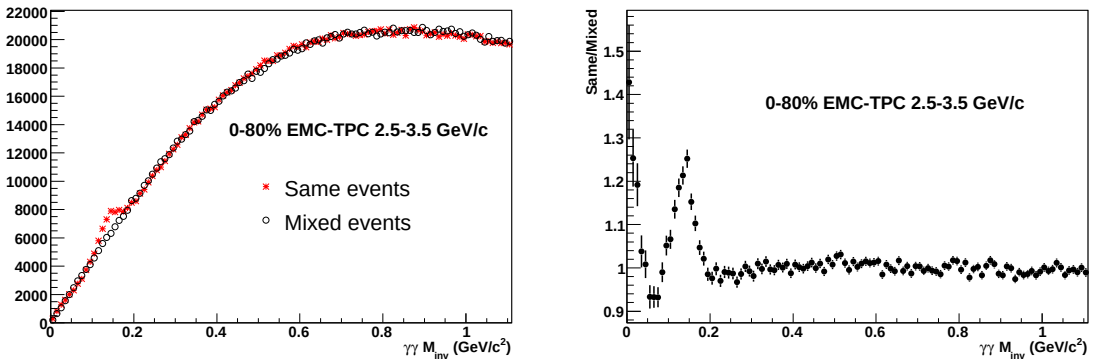

Figure 3.9: Left: Di-photon same- and mixed-event distributions normalized in the region of [0.5, 1.0] GeV/c^2. Right: Ratio of same- over mixed-event distributions.

The event mixing can be done using either the event pool method or the rotation method. The event pool method pairs photons from the event being analyzed with photons from events in a event pool, in which events have similar characteristics as the one being analyzed. Events are put into different pools according to their primary vertex z coordinate and multiplicity. The primary vertex z coordinate (-20 <VertexZ< 20 cm) is divided into 40 bins, with bin width of 1 cm; and the multiplicity (0 <RefMult< 800) is divided into 10 bins, with bin width of 80 tracks. Each event pool is maintained to have up to 5 events working like a queue, discarding the oldest event when a new one comes. Another characteristic that may be taken into account is the direction of reaction plane. Studies have been done to further divide events into 6 bins of reaction plane direction, and the final results are consistent with the ones without reaction plane binning. To improve statistics, the event mixing

is simplified to have only multiplicity and vertex binning. The event pool method is employed in the HT event analysis.

In the MB and central event analysis, the rotation method is used instead. The rotation method does not create any event pool, but mixes one photon with another one from the same event, after rotating the latter one by 180° in the ϕ plane. It is observed that the rotation method better reproduces the background at low p_T and thus gives flatter residual background shape, which is crucial because the signal-to-background ratio is smallest at low p_T.

Different photon combinations are used to calculate the invariant mass distribution. In MB and central events we pair an EMC photon with a TPC photon (EMC-TPC); and in HT events we use pairs of two EMC photons (EMC-EMC) too. Due to the relatively large tower size of the STAR BEMC, the low p_T single photon signal can be smeared by backgrounds such as overlapping photons, neutral particles, and residual charged particles not successfully vetoed in high multiplicity Au+Au events. The limited energy resolution at low energy ($16\%/\sqrt{E} \oplus 1.5\%$) also hinders the accurate measurement of photon energy. As a result, it is difficult to obtain a clear π^0 signal at low p_T by pairing EMC photons only. On the other hand, for TPC photons, the relatively tight geometrical cuts select very clean conversion photon samples. They significantly reduce the combinatorial background and improve the π^0 mass resolution. The EMC-TPC method gives a clear π^0 signal from below 1 GeV/c to the intermediate p_T (3-5 GeV/c) even in the most central Au+Au events. At higher p_T above the HT threshold, the EMC photons are less affected by backgrounds and the EMC-EMC method starts to produce clear π^0 signals. With the advantage of more statistics and higher efficiency, it is best able to measure the π^0 spectrum at higher p_T.

Figure 3.10 shows examples of the di-photon invariant mass distributions after mixed-event background subtraction for different π^0 reconstruction methods in Au+Au collisions at $\sqrt{s_{NN}}$=200 GeV. All figures are from the 0-20% centrality bin. They are fit to extract the raw π^0 yield, using a Gaussian plus background function. The total fit and the residual background curves are shown as solid and dotted lines respectively. For HT events at high p_T, the same- and mixed-event distributions are

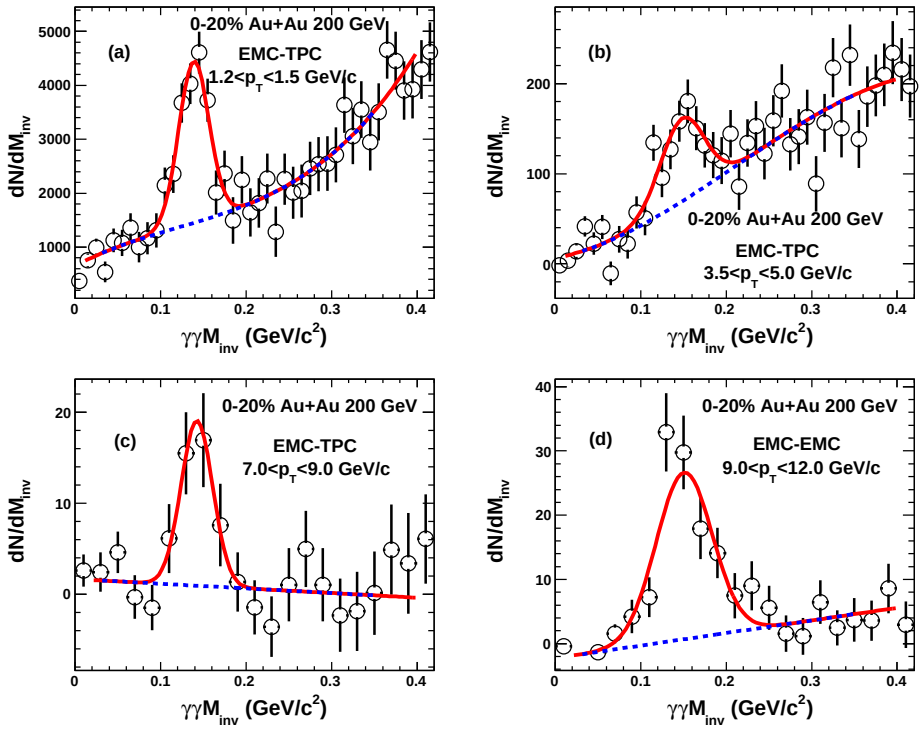

Figure 3.10: π^0 invariant mass distribution in 0-20% Au+Au collisions at $\sqrt{s_{NN}} = 200$ GeV. (a) EMC-TPC method in MB events at $1.2 < p_T < 1.5$ GeV/c; (b) EMC-TPC method in MB events at $3.5 < p_T < 5$ GeV/c; (c) EMC-TPC method in HT events at $7 < p_T < 9$ GeV/c; (d) EMC-EMC method in HT events at $9 < p_T < 12$ GeV/c. Solid lines are fit results of a Gaussian peak plus a 3rd order polynomial (panel a and b) or linear (panel c and d) background function. The residual backgrounds are shown as dotted lines.

normalized in the range of [0.5, 1.0] GeV/c^2, which is far away from the π^0 peak. The residual background is small and can be easily subtracted by fitting a linear dependence on M_{inv}. For MB and central events at low p_T, the signal-to-background ratio is rather small. After mixed-event background subtraction, a larger residual background is seen so a 3rd order polynomial function is used to subtract it out. To optimize the fitting to the residual background the normalization factor between same- and mixed-events is carefully chosen for each bin, so that the residual background has a shape roughly linearly increasing with mass, and can be described by a polynomial fit. The residual background can be due to the contaminations of BEMC photons as mentioned above, which introduce correlations not fully reproduced by the mixed-event technique. This effect is strongly centrality and p_T dependent, more pronounced in the more central events and at lower p_T. Figure 3.10(a) shows the situation where this effect is most severe; nevertheless the π^0 signal is still clearly seen on top of the background curve.

In order to assure that the fitting is reliable, especially at low p_T, several systematic checks have been performed. Firstly, results from two event mixing techniques, the event pool method and rotation method, are compared. Secondly, the normalization factor is adjusted and the invariant mass distribution is re-fit. Although these two procedures may significantly change the shape of residual background, yields extracted using the same fitting function are consistent within 10%, indicating the robustness of the fit. We have also changed the order of polynomial used for background fitting as well as the fit range, and consider the variance as the overall systematic errors.

Figure 3.11 shows the π^0 peak positions and widths from fitting as a function of p_T at $\sqrt{s_{NN}} = 200$ GeV using different π^0 reconstruction methods. Results from real data are compared to results from simulations of Monte Carlo (MC) π^0 embedded data. The π^0 peak position shows some p_T dependence at low p_T for the EMC-TPC method and at higher p_T for the EMC-EMC method. At low p_T the drop is understood as the effect of energy loss of e^+/e^- tracks. At high p_T the rise of peak position as a function of p_T is due to the limited energy resolution ($86\%/\sqrt{E} \oplus 12\%$) and the energy saturation effect of the BSMD. It has been found that the BSMD channels saturate when the energy deposited exceeds about 6 GeV. This effect leads

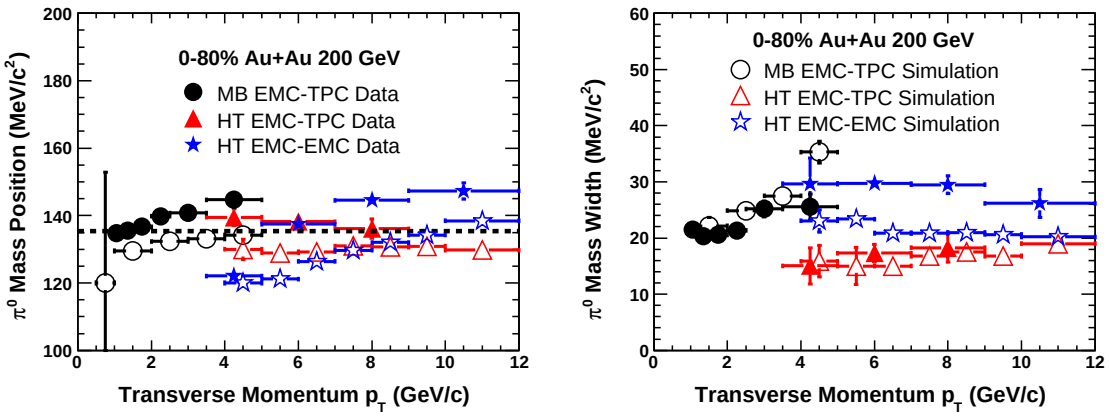

Figure 3.11: π^0 invariant mass peak position and peak width as a function of p_T in 0-80% 200 GeV Au+Au collisions. The results from π^0 embedded simulation are also shown for comparison. The dotted line is the π^0 mass value from PDG. The legends apply for both figures.

to more evenly distributed energies in two close photons on the BEMC when they hit the same tower, and therefore produces a larger invariant mass, more pronounced at higher p_T. The trend of p_T dependence is well reproduced by the simulation but it underestimates the mass peak position by 5-10 MeV/c^2, which may indicate an offset of the BEMC gain calibration. The use of TPC photons significantly improves the π^0 peak resolution. For the same HT data sample the EMC-EMC method also gives peak width broader than the EMC-TPC method, which is confirmed by the simulation. Comparing the MB and HT data samples, the requirement of BSMD hits clearly improves the spatial resolution of EMC photons, and thus gives narrower π^0 peak width.

3.1.5 Prescale factor

The π^0 spectra from the MB and HT event samples will be combined to obtain the spectra over the whole p_T range. The HT events are a subset of MB events which satisfy the HT trigger requirement. Therefore, we need to know the number of equivalent MB events with respect to the HT sample used in the analysis, in order to properly scale the spectra from HT events and match the ones from MB events.

Such information can be acquired from the data. When the data was being collected, before each run was started, a prescale factor $F_{prescale}$ was assigned to each trigger, indicating their priority of being accepted during the run. The factor of $F_{prescale}$ means that one out of $F_{prescale}$ number of events satisfying this trigger is accepted by the data acquisition system (DAQ). The DAQ system is unable to accept every collision happening, with a maximum Au+Au collision rate of about 100 Hz through the 2008 run and up to 1000 Hz after the DAQ upgrade. Therefore, for runs targeting rare triggered events (such as HT and Υ triggers), to ensure that we could collect as many of them as possible, the prescale factor of rare trigger is set to be 1, while the prescale factor of MB trigger is set to a larger number, such as 500. The prescale factor could be changed run by run.

The number of equivalent MB events for a HT data sample is calculated as:

$$N_{MB} = N_{HT} \frac{\sum_i F^i_{prescale\_MB} N^i_{MB}}{\sum_i F^i_{prescale\_HT} N^i_{HT}} \tag{3.4}$$

where the sum includes all runs in which HT events are collected, and $F^i_{prescale\ HT}$ is always 1 in this case. Here the same event selection cuts as mentioned in Section 3.1.1 are applied. The relative factors between MB and HT events in different centralities are shown in Figure 3.12. As we can see, it is more likely to acquire a HT event in more central collisions.

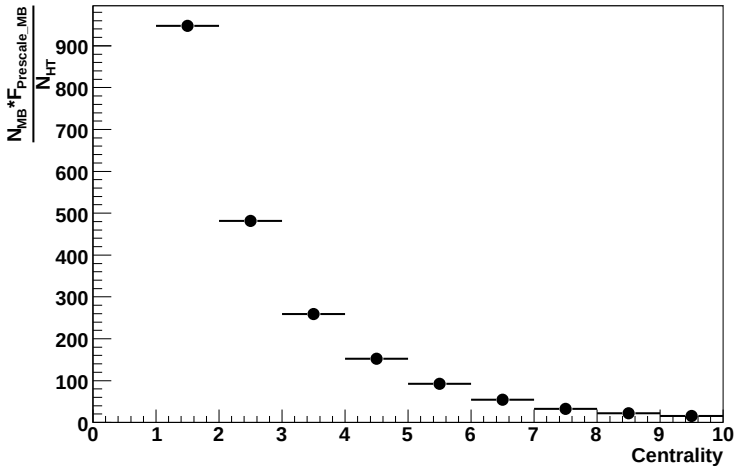

Figure 3.12: The number of equivalent MB events for one HT event in different centralities in Au+Au 200 GeV collisions. A larger number on the x axis represents more central collisions.

3.2 Efficiency calculation

In this section the π^0 reconstruction efficiency calculated from the embedding data is discussed. Two important corrections are done: the geometry correction for the photon conversion probability, and the BEMC acceptance correction.

3.2.1 Embedding procedure

The π^0 raw yield extracted from the di-photon invariant mass distribution is corrected by an overall detection efficiency. The efficiency is defined as

$$eff(y, p_T) = \frac{N_{reconstructed}(y, p_T)}{N_{produced}(y, p_T)}, \tag{3.5}$$

where $N_{produced}(y, p_T)$ is the number of π^0's produced in Au+Au collisions in a p_T and rapidity phase space, and $N_{reconstructed}(y, p_T)$ is the number of π^0's reconstructed in the same events and phase space. The efficiency is calculated from Monte Carlo (MC) simulations, where we employ a technique of embedding MC π^0's into real events.

In the embedding procedure, MC π^0's are randomly generated with constraints on phase parameters such as p_T, η, and azimuthal ϕ angle. They are then propagated in GEANT [68], where the geometry of STAR detector system is described and simulated. In GEANT MC particles can decay following their realistic decay kinematics. GEANT simulates their interactions with material in the STAR detectors, and particles leave hits in detectors as they do in reality. These MC hits are mixed with raw hits from a real event. The combined result is sent through the event reconstruction procedure, where, for example, raw TPC hits are fit and tracks are reconstructed. Finally a data file very similar to the original real data is created, only with some additional MC particles embedded in it.

The π^0 embedding data used in this analysis is located at PDSF [69]. There are totally 110k events, with 19k MB events and most of others are central triggered events. The multiplicity distribution can be seen in the left panel of Figure 3.13. MC π^0's are generated with a flat p_T distribution in a range of $0 < p_T < 20$ GeV/c (see left panel of Figure 3.14). They cover $-2 < \eta < 2$ and full azimuthal of $0 < \phi < 2\pi$

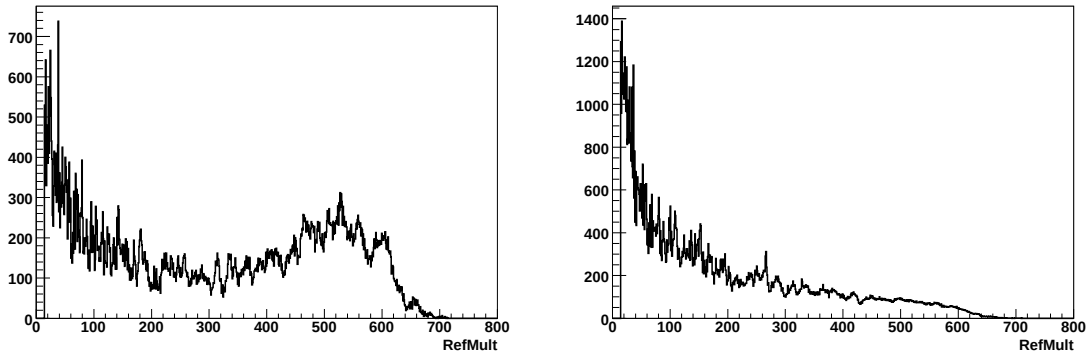

Figure 3.13: Left: Reference multiplicity distribution of embedding data before weighting. Right: Reference multiplicity distribution of embedding data after weighting.

with flat η and ϕ distributions, which can be seen in Figure 3.15. The number of π^0's embedded in each event is proportional to the event multiplicity.

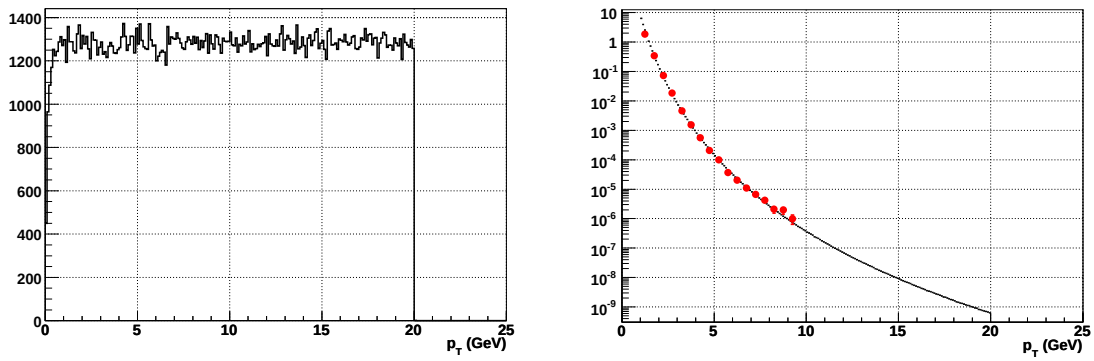

Figure 3.14: Left: p_T distribution of input MC π^0's. Right: p_T distribution of MC π^0's after weighting is shown as a curve. The PHENIX π^0 spectrum is shown as data points for comparison.

The embedding data is a mixture of events from different triggers, with a multiplicity distribution different from the pure MB and central events in real data analysis. The input MC π^0 spectrum is also different from the real data, where the π^0 spectrum rapidly drops as p_T increases. To fully make use of all statistics, the embedding events are weighted so that they mimic the realistic reference

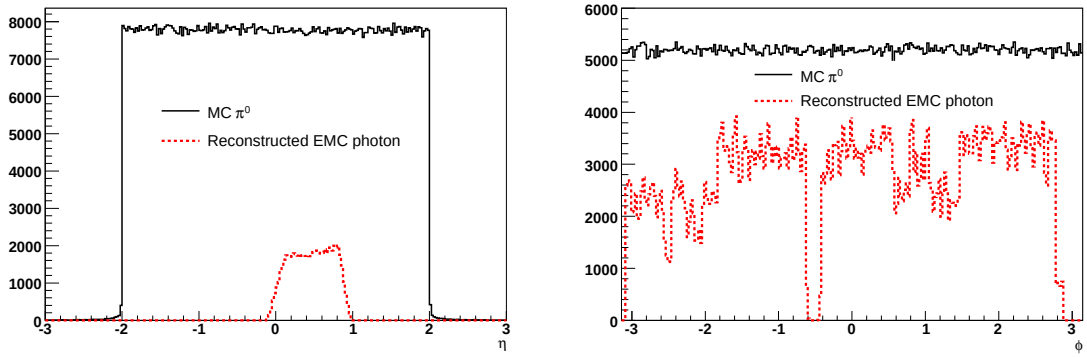

Figure 3.15: Left: η (left) and ϕ (right) distributions of MC π^0 and reconstructed EMC photons.

multiplicity distribution. The MC π^0 spectrum is also weighted to mimic the earlier measured PHENIX π^0 spectra [16]. In more detail, a weighting factor $f_{tot.} = f_{mult.}(RefMult) * f_{spec.}(p_T)$ as a function of event multiplicity and p_T is assigned to each MC π^0, where $f_{mult.}(RefMult) = \frac{\text{RefMult Distribution}_{data}(RefMult)}{\text{RefMult Distribution}_{MC}(RefMult)}$ is the multiplicity weighting, and $f_{spec.}(p_T) = \frac{\pi^0 \text{ Spectrum}_{data}(p_T)}{\pi^0 \text{ Spectrum}_{MC}(p_T)}$ is the spectrum weighting, where p_T is in unit of GeV/c. After weighting the embedding event multiplicity distribution and the MC π^0 spectrum follow the realistic ones, which can be seen in the right panel of Figure 3.13 and 3.14.

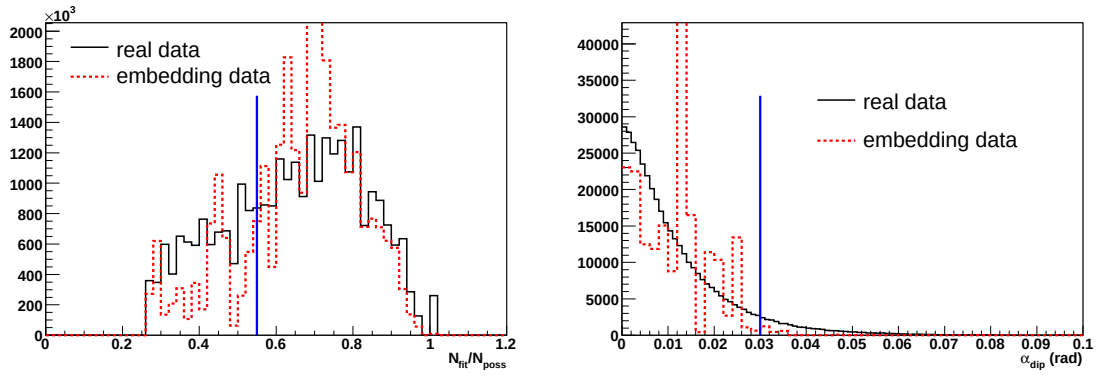

Figure 3.16: Left: $\frac{N_{fit}}{N_{poss}}$ distributions in e^+/e^- selection from data and embedding. Right: Dip angle difference α_{dip} in TPC photon selection from data and embedding. Distributions from embedding show reconstructed tracks with associated MC counterparts, and with spectra weighting applied as mentioned above.

Several more QA checks are done to compare the distributions of parameters used for photon and π^0 selection from data and embedding. Figure 3.16 presents two examples of $\frac{N_{fit}}{N_{poss}}$ (number of fit points over number of maximum possible fit points) and α_{dip} (Dip angle difference in rz-plane between e^+ and e^- at the conversion point), which show reasonable consistency between data and embedding. The reconstructed EMC photon η and ϕ distributions are also similar to the ones obtained from real data (see Figure 3.15), indicating that the BEMC status table is correctly applied.

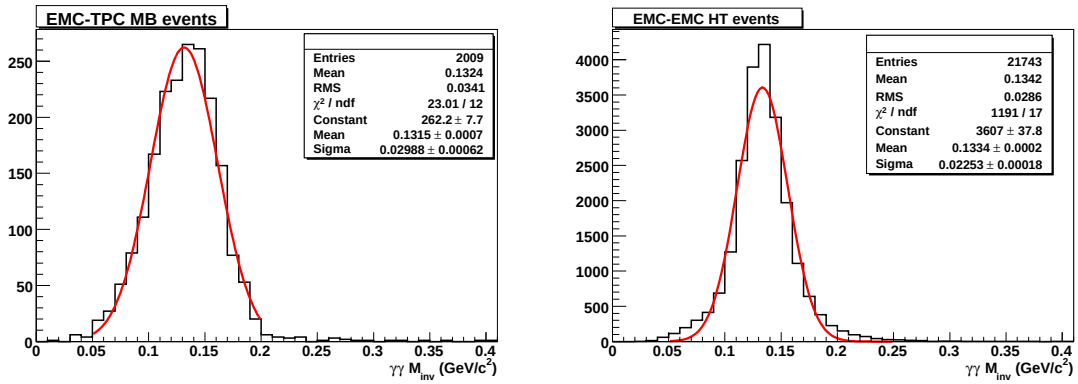

Figure 3.17: Reconstructed π^0 signal in embedding data analysis from EMC-TPC method in MB events (left) and from EMC-EMC method in HT events (right). Each reconstructed π^0 can be associated with a MC π^0. Results from Gaussian fit are also shown.

The same cuts as in the real data analysis are used to reconstruct the embedded MC π^0's. Several additional cuts are applied to associate the reconstructed particles to their MC counterparts. For TPC photons, 5 common hits are required to associate a reconstructed e^+/e^- track with an MC track, and both e^+/e^- tracks should be associated to two MC daughter tracks of a MC photon. For EMC photons in MB and central events, due to the fact that no SMD hits are required in the real data analysis, the BEMC tower in which a EMC photon is reconstructed should be the most energetic BEMC hit of a MC photon. For EMC photons in HT events, the position difference between a reconstructed photon and an MC one should be less than 0.02 in $\Delta\eta$ and $\Delta\phi$. For a reconstructed π^0, its two daughter photons should be associated with two photons from a MC π^0, and its di-photon invariant mass should be within [0.03, 0.23] GeV/c^2 for the EMC-TPC method, and within [0.03,

0.3] GeV/c^2 for the EMC-EMC method. The wider acceptance is due to the worse invariant mass resolution of the EMC-EMC method. Figure 3.17 shows the π^0 signal from π^0's embedded into the MB and HT events, and the detailed comparison of π^0 peak position and width between data and embedding can be found in Figure 3.11.

The efficiency for a given y and p_T bin is calculated as the ratio of the number of reconstructed π^0's in that bin over the number of π^0's in that bin from the input. The advantage of using embedding data is that the calculated efficiency takes into account many effects such as the losses due to acceptance, photon conversion probability, tracking inefficiency, all quality cuts, TPC track energy loss, and BEMC energy contamination. Before showing the π^0 reconstruction efficiency two more corrections should be done: the geometry correction and BEMC acceptance correction, which will be discussed in the next two sections.

3.2.2 Geometry correction

The conversion probability calculation is crucial for the π^0 efficiency when TPC photons are used. The photon conversion probability is proportional to the amount of matter it goes through. To reproduce the conversion probability, one relies on the accurate description of the geometry inside the detector. As a result, it is necessary to compare the result of photon conversion between real data and simulation, and correct for any inconsistency.

The simulation is performed by generating 25k π^0 only events using the STAR simulation geometry matching the year 2004 RHIC run, named y2004c and y2004d, respectively. The only difference between y2004d and y2004c is that the "d" version contains updated SVT wafer geometry. The reason for using two geometries is to observe whether the SVT geometry update will affect the photon conversion probability significantly. Each event has 200 π^0 with a realistic p_T distribution from the PHENIX result [16], and η distribution from the PHOBOS result [70]. The generated π^0 p_T starts from 0.5 GeV/c to have more statistics, since π^0's below 0.5 GeV/c can hardly be reconstructed. Their spatial distribution is $-2 < \eta < 2$ and $0 < \phi < 2\pi$ with a flat ϕ distribution. The z coordinate of event vertex is restricted to -20 <VertexZ< 20

cm. The generated π^0's are reconstructed using the same cuts as in real data analysis. To remove fake photons from combinatorial background, the e^- tracks are rotated by 180° in the azimuthal plane and with its origin point flipped with respect to the beam line. These rotated tracks are paired with the intact e^+ tracks. "Photons" reconstructed in this way are statistically subtracted out from the earlier photon candidates. They contribute to about 10% of all the reconstructed conversions.

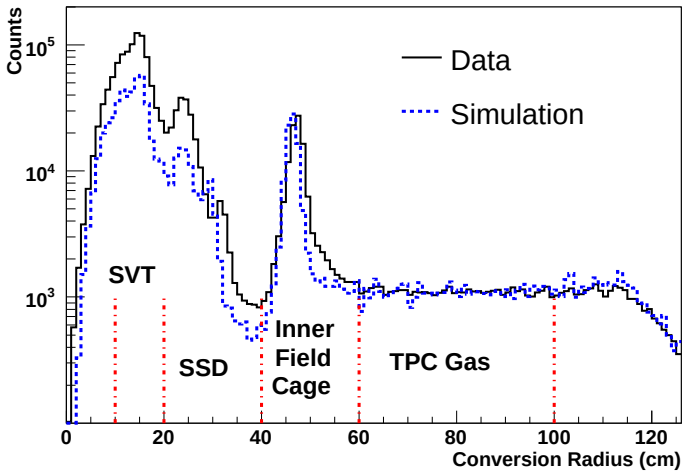

Figure 3.18: Photon conversion radius distributions from real data and MC simulation in 200 GeV Au+Au collisions. Two distributions are normalized in the TPC gas region at $60 < r < 100$ cm.

We compared the radius distributions of photon conversions between data and this MC simulation and it is shown in Figure 3.18. Simulation results from two geometry configurations are combined. The two distributions are normalized in the TPC gas region where geometry is simple and well understood. The comparison indicates that the photon conversion probability can be well reproduced in the regions of TPC gas and inner field cage, but is underestimated in the regions of SVT and SSD where structures are complex. This observation is consistent with previous studies [64, 66].

The comparisons in the SVT ($10 < r < 20$ cm) and SSD ($20 < r < 40$ cm) areas are shown in Figure 3.19 and 3.20, where the z coordinate distributions are drawn. It is clearly seen that the conversion probability is underestimated by a roughly constant factor of 2 at mid-rapidity, and that simulations using two different

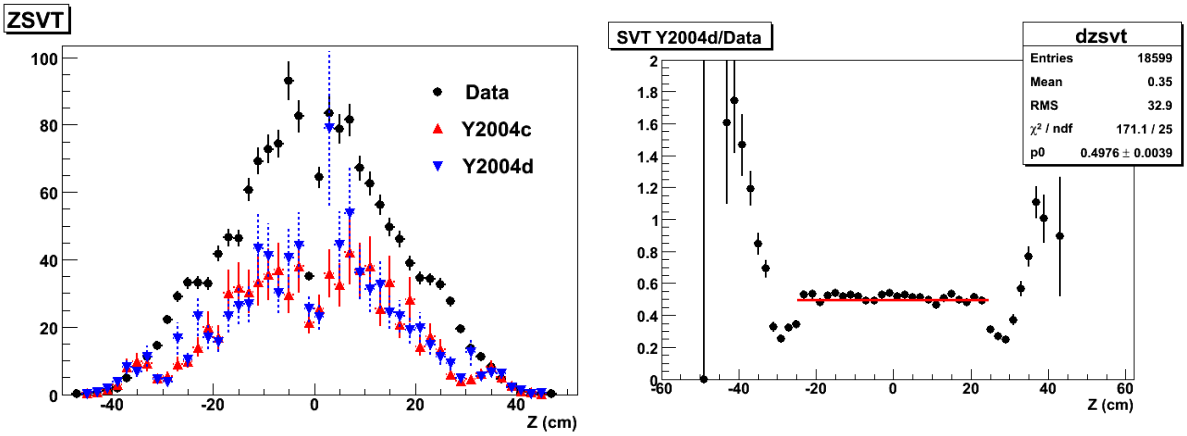

Figure 3.19: Left: z coordinate distributions of conversions in the SVT area ($10 < r < 20$ cm) from data and simulation, after normalization in the TPC gas area ($60 < r < 100$ cm). Right: Ratio of combined simulation over data result in the left panel.

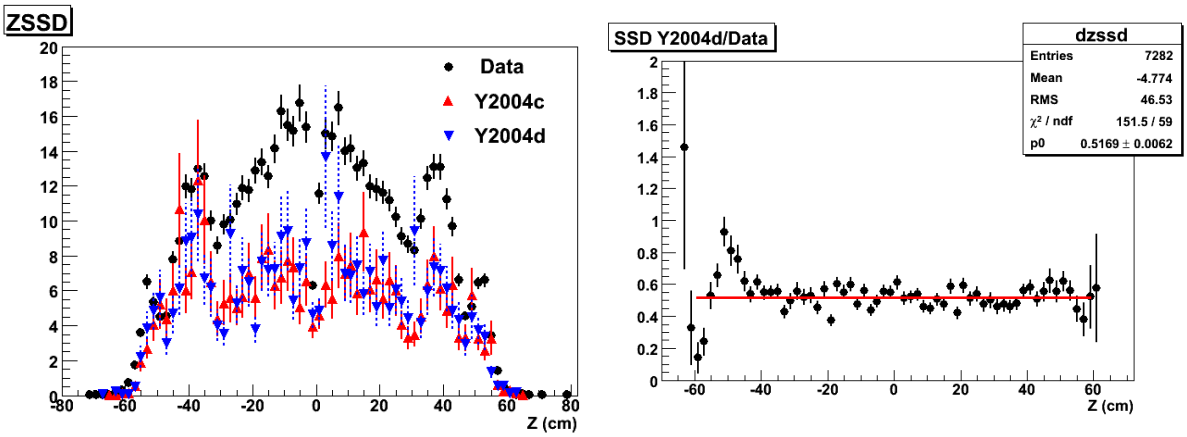

Figure 3.20: Left: z coordinate distributions of conversions in the SSD area ($20 < r < 40$ cm) from data and simulation, after normalization in the TPC gas area ($60 < r < 100$ cm). Right: Ratio of combined simulation over data result in the left panel.

geometry configurations give very similar results. It is the reason for combining results in Figure 3.18.

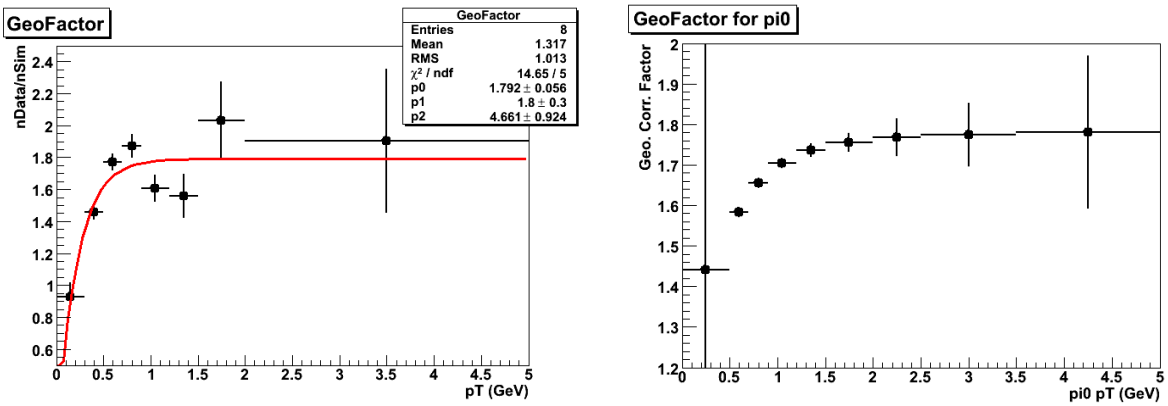

Figure 3.21: Conversion probability correction factor for TPC photons (left) and π^0's (right) as a function of p_T.

Any results involving TPC photons should be corrected for this effect, using the conversion rates in the TPC gas as a reference. The correction is done in the following way. A correction factor $F_{geo} = \frac{(n_{det}/n_{gas})_{data}}{(n_{det}/n_{gas})_{MC}}$ is calculated as a function of photon p_T, where n_{det} and n_{gas} are numbers of conversions in the whole detector and in the TPC gas only. This factor is shown in the left of Figure 3.21. The p_T dependence of F_{geo} is understood as the result of different conversion point distributions for reconstructed photons with different p_T. The fitting result $f_\gamma(p_T)$ is used to transform this factor to the correction for π^0's. Here two methods are used: 1. The correction is done p_T bin by p_T bin. For π^0's in a certain p_T bin, their decay photon p_T spectrum can be obtained by simulation. This spectrum is scaled up bin by bin by factors calculated from $f_\gamma(p_T)$. Then the ratio of integrated spectrum after scaling-up over the one before scaling-up is the correction factor for π^0's at that p_T bin. Repeating the procedure for all p_T bins, the correction factor as a function of π^0 p_T can be seen in the right panel of Figure 3.21. 2. In the embedding analysis a reconstructed TPC photon associated with an MC photon is weighted by the factor $f_\gamma(p_T)$ corresponding to its p_T. The weighting eventually folds the correction in the π^0 efficiency calculation. Spectra calculated from these two methods agree with each other within statistical error bars, and their difference will be taken into account in the final systematic error.

3.2.3 BEMC acceptance correction

Another important correction is the BEMC acceptance. Unlike the TPC which has relatively stable and uniform acceptance, the BEMC acceptance can be changing from run to run. When data was being collected, any dead or hot BEMC tower or SMD strip, and any power supply problem on the BEMC could cause the loss of BEMC acceptance. On the other hand, data used for the embedding simulation is only a small part of the whole data sample. If the BEMC acceptance in the embedding data fails to represent the real data, the efficiency can be mis-calculated. Figure 3.22 and 3.23 show event-averaged energy deposited in BEMC towers and SMD strips in different days of run to demonstrate the changing acceptance.

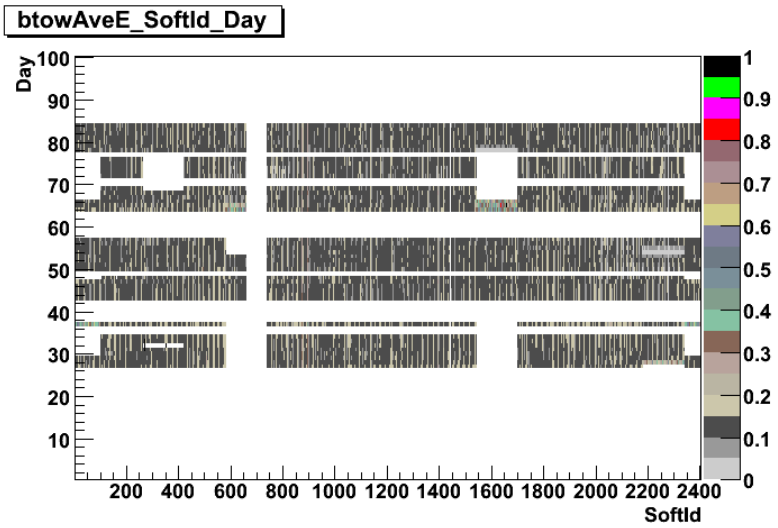

Figure 3.22: Event-averaged energy deposited in BEMC towers in different days of run. The "SoftId" is STAR's internal label for each BEMC tower.

Data sample used in embedding is from day 44 and 66. The averaged acceptances in the real data and embedding are calculated and compared. The average is obtained by weighting the acceptance of each day using the total number of events in that day. The comparison can be seen in Table 3.3. For MB events, where no SMD hits are required, the acceptance in embedding is 12% higher than real data. Therefore, the efficiency is over-estimated by 12%, and a factor of 1.12 should be applied to the MB π^0 spectra. In contrast, for HT events where SMD hits are required, the SMD

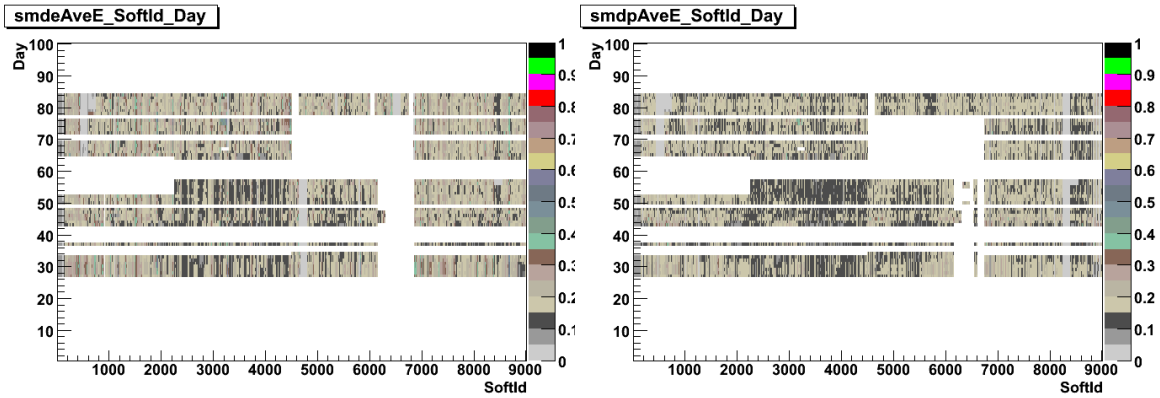

Figure 3.23: Event-averaged energy deposited in SMD η (left) and ϕ (right) strips in different days of run. The "SoftId" is STAR's internal label for each SMD strip.

Accpt. Embedding/Data	All good EMC data (MB)	ProductionLowMidHigh (HT)
BTOW	1.12	1.037
SMDE	0.954	1.009
SMDP	0.933	0.991

Table 3.3: Ratio of BEMC acceptance between embedding and real data in BEMC tower, SMD η, and SMD ϕ strips in different data samples.

acceptances are almost identical in embedding and real data, so the correction is negligible.

3.2.4 Efficiency

With the necessary corrections done, the total π^0 detection efficiency is shown in Figure 3.24. The geometry correction is included in the figures, but the BEMC correction is applied separately to the spectra. The use of TPC photons helps improve the π^0 signal resolution, but is more statistically challenging, due to the low conversion probability. Using one TPC photon instead of an EMC photon results in about a factor of 5 decrease of π^0 detection efficiency. Using EMC photons enhances the efficiency significantly and is more preferable in studying π^0 spectrum at high p_T.

The efficiency calculated here is used to correct the raw π^0 yield obtained in last section. In next section we will discuss in detail the systematic uncertainties of this analysis.

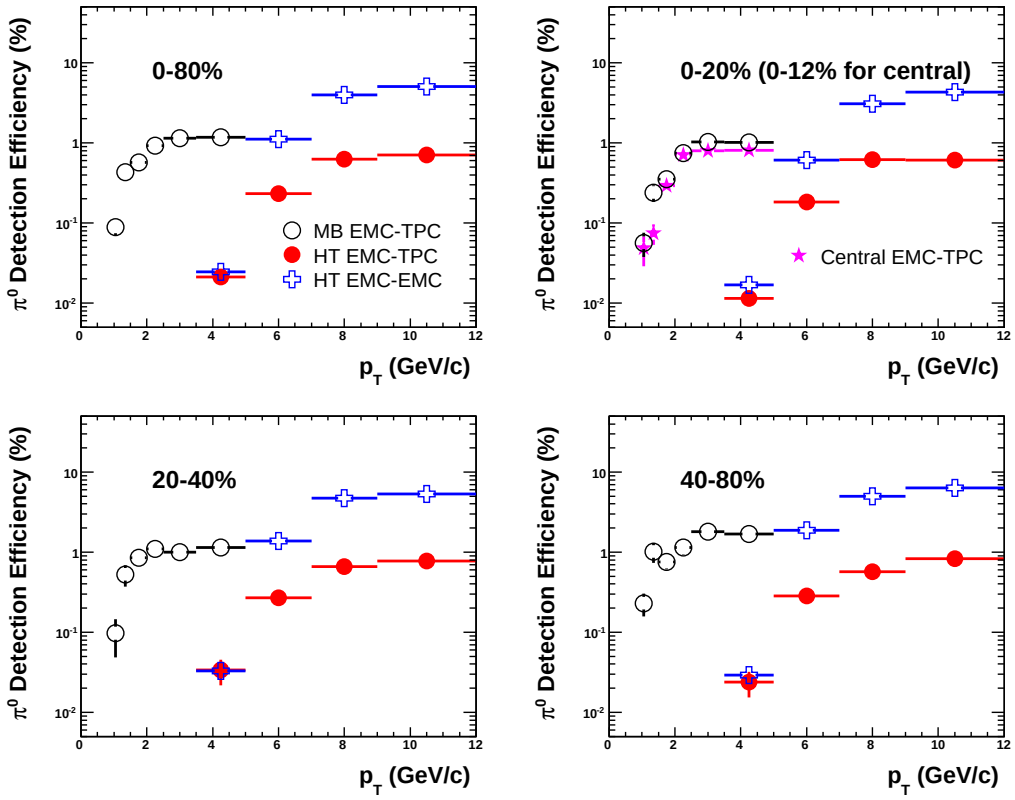

Figure 3.24: Total π^0 detection efficiency for three methods as a function of p_T in different centrality bins in 200 GeV Au+Au collisions.

Selection	Original cut	Tight cut	Loose cut
e^+/e^-	$N_{fit} > 12$	$N_{fit} > 18$	$N_{fit} > 9$
	$\frac{N_{fit}}{N_{poss}} > 0.55$	$\frac{N_{fit}}{N_{poss}} > 0.65$	$\frac{N_{fit}}{N_{poss}} > 0.45$
photon	$\mathrm{DCA}_{xy} < 1.5$ cm	$\mathrm{DCA}_{xy} < 0.75$ cm	$\mathrm{DCA}_{xy} < 2$ cm
	$\mathrm{DCA}_z < 1.2$ cm	$\mathrm{DCA}_z < 0.9$ cm	$\mathrm{DCA}_z < 1.5$ cm
	$\alpha_{dip} < 0.03$ rad	$\alpha_{dip} < 0.02$ rad	$\alpha_{dip} < 0.04$ rad
	$\Delta dip < 0.035$ rad	$\Delta dip < 0.02$ rad	$\Delta dip < 0.05$ rad
	$\Delta\phi < 0.05$ rad	$\Delta\phi < 0.03$ rad	$\Delta\phi < 0.07$ rad
	$m_{e^+e^-} < 12$ MeV/c^2	$m_{e^+e^-} < 6$ MeV/c^2	$m_{e^+e^-} < 30$ MeV/c^2

Table 3.4: Variation of TPC photon reconstruction cuts used to evaluate systematic uncertainty of π^0 spectra.

3.3 Systematic errors

In this section systematic uncertainties of the π^0 spectra are discussed. Major sources of systematic uncertainties include changing quality cuts for π^0 reconstruction, raw π^0 yield extraction, and BEMC overall energy scale.

3.3.1 Cut study

First, systematic uncertainties are estimated by varying photon reconstruction cuts. Different photon PID cuts are used and the fully corrected spectra are compared. Cut studies for TPC and EMC photons are performed separately. For TPC photons, two additional sets of cuts with tighter/looser requirements than in the original analysis are applied, as shown in Table 3.4, and the results are compared to the original cuts. For EMC photons in MB events, a different energy cut of tower energy greater than 150 MeV and at least 75 MeV higher than neighbor towers is used to select EMC photon samples with different level of purity. In HT events, instead of a single tower, a cluster with up to 2×2 towers is used to reconstruct an EMC photon.

The comparisons of results from varied cuts and original cuts are shown Figure 3.25 and 3.26. For the EMC photon figure, the ratios of spectra from varied cuts and original cuts over their averaged spectrum are shown. The typical systematic uncertainty from changing TPC photon cuts is 10-30%, with the largest uncertainty usually at the lowest p_T bin, where background is the largest. The source of the

abnormally large uncertainty at [3.5, 5.0] GeV/c p_T bin in 0-20% HT events is still unknown, but it can be due to the limited statistics in embedding data. Assuming that the systematic error should be similar to other centralities in the same p_T bin, we assign an uncertainty of 30% to this bin. The systematic uncertainty from changing EMC photon cuts ranges from 10-20%, again with the largest uncertainty usually at the lowest p_T bin. There are also a couple of points at [3.5, 5.0] GeV/c p_T bin with large uncertainty, mainly due to the failure of obtaining a clear π^0 signal when using the 4-tower cluster algorithm. Assuming the same argument as above, a typical value of 20% uncertainty is assigned to these bins.

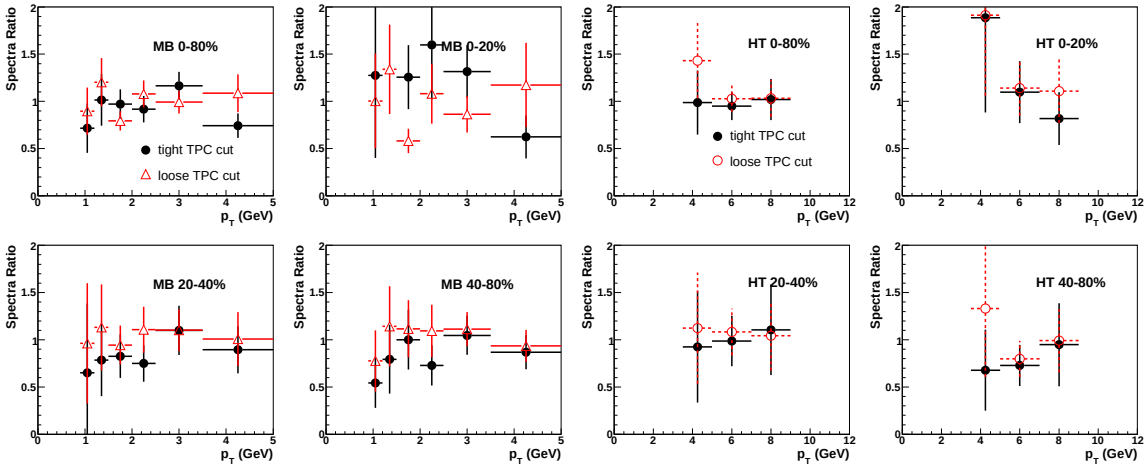

Figure 3.25: Ratio of π^0 spectra from tight/loose TPC photon reconstruction cuts over original cuts for different centrality bins using EMC-TPC method in MB (left) and HT (right) event samples.

3.3.2 Yield extraction

The raw yield of π^0 from data is sensitive to the fitting techniques used to extract it, including the background fit function, fit range, and the normalization of same- and mixed-event invariant mass distributions. Figure 3.27, 3.28, and 3.29 show the change of results after applying different fitting techniques. The ratio of spectra from two fitting parameters over their averaged values is shown. Details of the change of fitting parameters can be found in captions of individual figures. Results using different fit

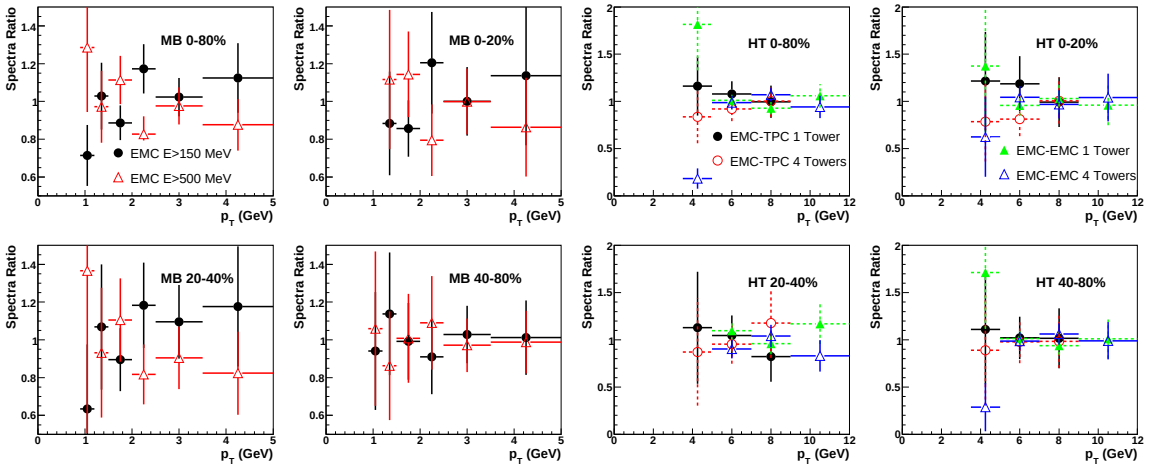

Figure 3.26: Change of π^0 spectra from varied EMC photon reconstruction cuts and original cuts for different centrality bins in MB (left) and HT (right) event samples.

parameters indicate a systematic error of 10-15% in raw yield extraction.

3.3.3 BEMC energy scale

The absolute energy scale of the BEMC, which translates measured ADC values of towers into energy deposited, affects the overall level of the π^0 spectra. Any inaccuracy of the BEMC gain calibration can result in a systematic shift of the π^0 spectra: if too large a gain is used, the spectrum is shifted to the higher p_T direction. The magnitude of such an inaccuracy is not trivial to know. Using data from collisions of simple systems such as p+p and d+Au should give us a hint, by comparing the π^0 invariant mass peak positions in data and simulation: larger gain leads to larger peak position. However, the discrepancy of π^0 peak position may be due to multiple effects, so far it can only provide us an upper limit of 4-5% [73]. To estimate the possible effect of this on measured π^0 yields, the BEMC energy scale is modified by $\pm 4\%$ in the embedding data analysis, and the new efficiencies are compared to original values. This gives a 20-30% systematic error throughout the p_T range, which is shown in Figure 3.30.

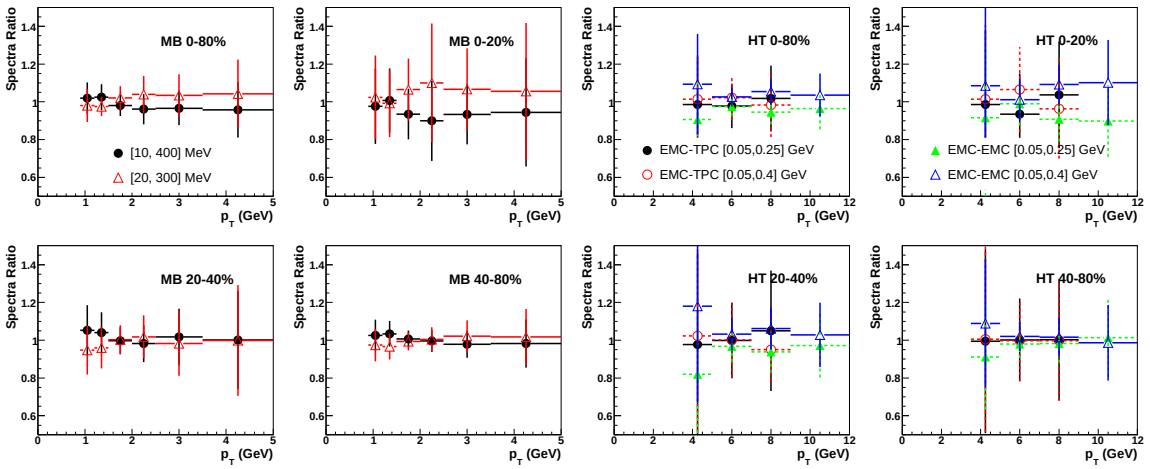

Figure 3.27: Change of π^0 spectra from different fit ranges for different centrality bins in MB (left) and HT (right) event samples.

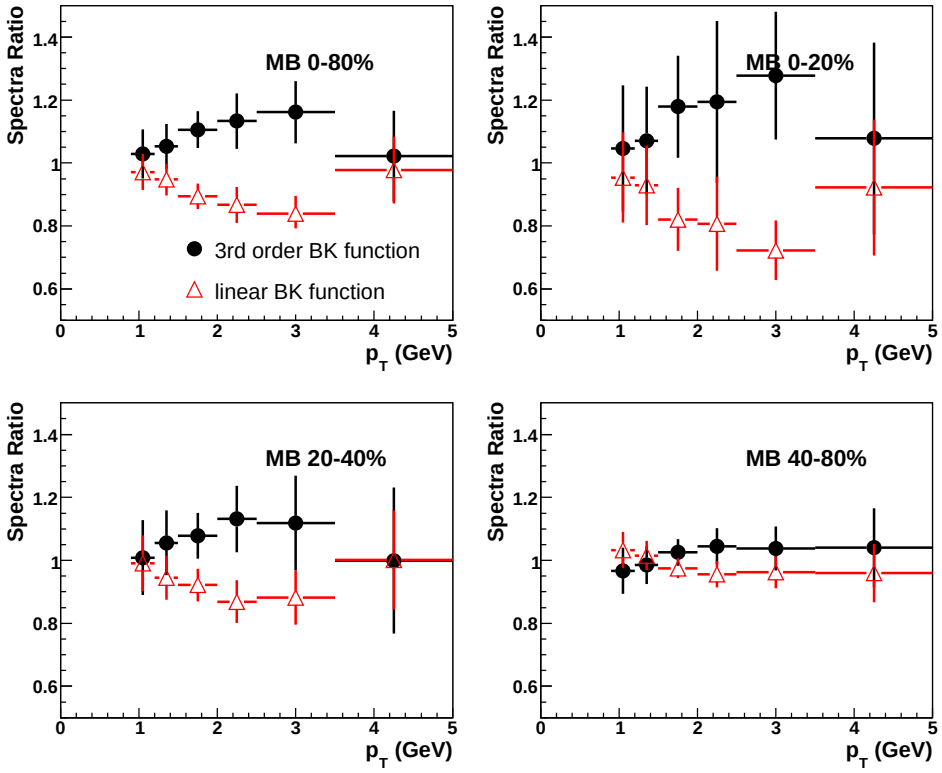

Figure 3.28: Change of π^0 spectra from different fit functions (3rd order polynomial vs. linear function) for different centrality bins in MB event samples.

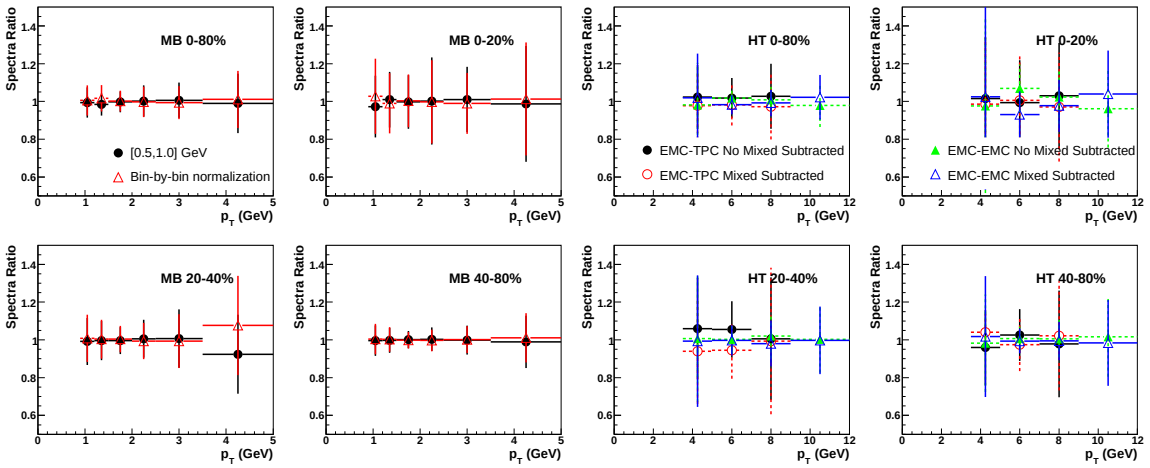

Figure 3.29: Change of π^0 spectra from different normalization factors used in mixed-event background subtraction for different centrality bins in MB (left) and HT (right) event samples. The bin-by-bin normalization is discussed in section 3.1.4. In HT events, the same-event di-photon invariant mass distribution is fit either with or without the mixed-event background subtracted.

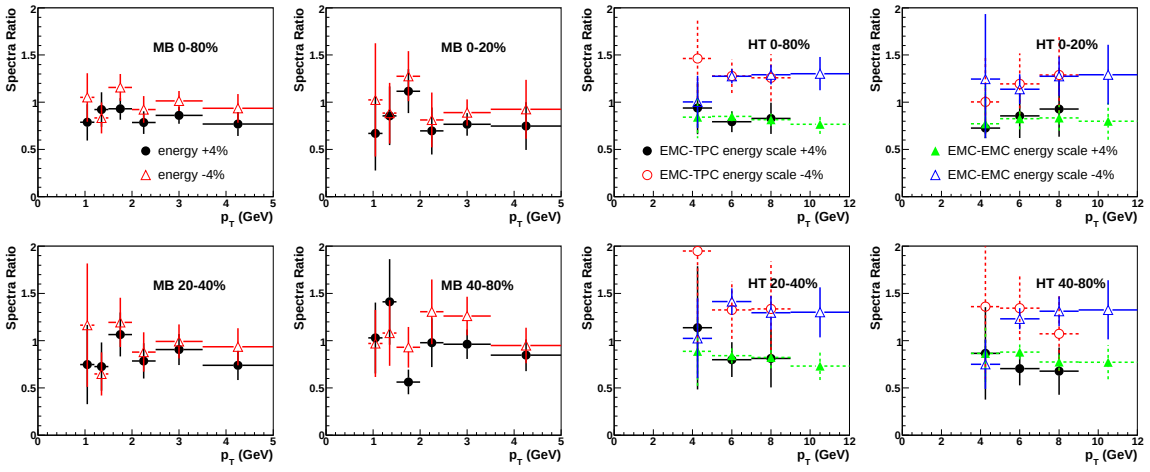

Figure 3.30: Change of π^0 spectra from different BEMC energy scale offsets for different centrality bins in MB (left) and HT (right) event samples.

3.3.4 Geometry correction

As discussed in section 3.2.2, the geometry correction is performed as a function of π^0 p_T. As a cross check, the correction is instead applied as a function of conversion position. The results are compared to those obtained with the original method. The correction factor as a function of conversion radius is shown in Figure 3.31. Again in the embedding analysis a reconstructed TPC photon associated with a MC photon is weighted by a factor corresponding to its conversion radius, which folds the correction into the π^0 efficiency calculation.

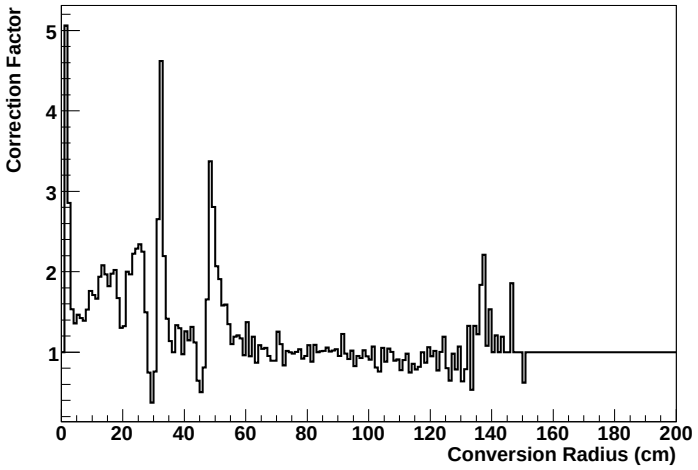

Figure 3.31: Geometry correction factor as a function of conversion radius applied in the embedding analysis.

The comparison to the original method is shown in Figure 3.32. The ratio of spectra from two methods over their averaged values is shown. Results from two methods are consistent with each other. The only exception is still the lowest p_T bin in HT events, which can be due to the limited statistics and fluctuation of the correction factors (spikes in Figure 3.31). Here a systematic uncertainty of 10% is assigned to take it into account.

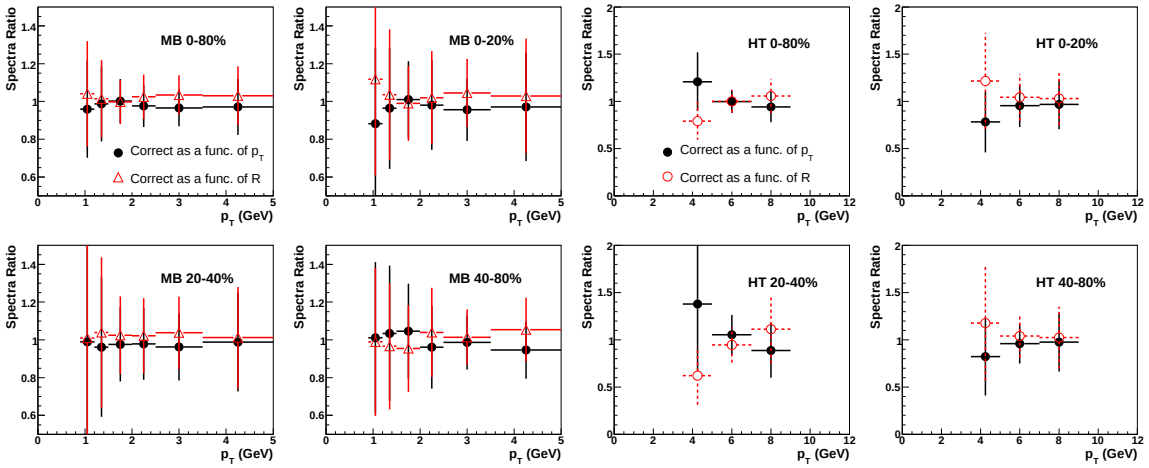

Figure 3.32: Change of π^0 spectra from different geometry correction methods for different centrality bins in MB (left) and HT (right) event samples.

	MB	HT	
	EMC-TPC	EMC-TPC	EMC-EMC
Photon Cuts	20%	20-30%	10-20%
Energy Scale (±4%)	20%	20-30%	20-30%
Yield Extraction	10%	15%	10%
Geometry Correction	10%	10%	–

Table 3.5: Summary of major sources of systematic uncertainties on the π^0 yields in 200 GeV Au+Au collisions.

3.3.5 Summary of systematic errors

As a summary, the major systematic uncertainties are listed in Table 3.5. They are added in quadrature to obtain the total systematic error in the π^0 yield.

3.4 Results

In this section the π^0 spectra and the nuclear modification factors R_{AA} and R_{CP} in 200 GeV Au+Au collisions are presented. They are compared to earlier STAR $\pi^{\pm}$ and PHENIX π^0 results, as well as the theoretical calculation of light quark energy loss through gluon radiation.

3.4.1 STAR π^0 spectra

Figure 3.33 shows the π^0 invariant yield per event at mid-rapidity ($0 < \eta < 0.8$) as a function of p_T in 200 GeV Au+Au collisions for different centrality bins. Statistical and systematic errors are shown as vertical lines and bars respectively. The π^0 spectra are measured over an extended p_T range from 1 to 12 GeV/c. For central triggered events the spectrum is measured up to 5 GeV/c due to the lack of HT triggered events. Results from different π^0 reconstruction algorithms and different data samples are compared in overlapping p_T range and agree well. Therefore the combined averaged result will be used in the following figures.

The STAR π^0 results are compared to earlier STAR $\pi^{\pm}$ and PHENIX π^0 results. Due to different p_T bin definitions, a Levy-function fit of earlier results is used. The ratios of spectra over their fits are shown in Figure 3.34, which indicate that the fit describes the data well.

The ratios of the STAR π^0 spectra over the STAR $\pi^{\pm}$ [71] and the PHENIX π^0 [16] in 200 GeV Au+Au collisions are shown in Figure 3.35. The error bars of earlier results are propagated using the averaged error of two neighboring data points. The spectrum ratio is larger in peripheral collisions than in central and mid-central collisions, where the yield of STAR π^0 appears to be slightly lower than the STAR $\pi^{\pm}$ but closer to the PHENIX π^0. With the best statistics in MB 0-80% centrality, the STAR π^0 yields are about 15% smaller than the STAR $\pi^{\pm}$ over the p_T range, but they are still consistent within systematic uncertainties. The discrepancy has not yet been fully understood. One possible reason may be an overall offset of the BEMC energy scale, indicated by the p_T independent ratio distribution. It has been demonstrated in the systematic uncertainty study that the π^0 spectra are very sensitive to it. However,

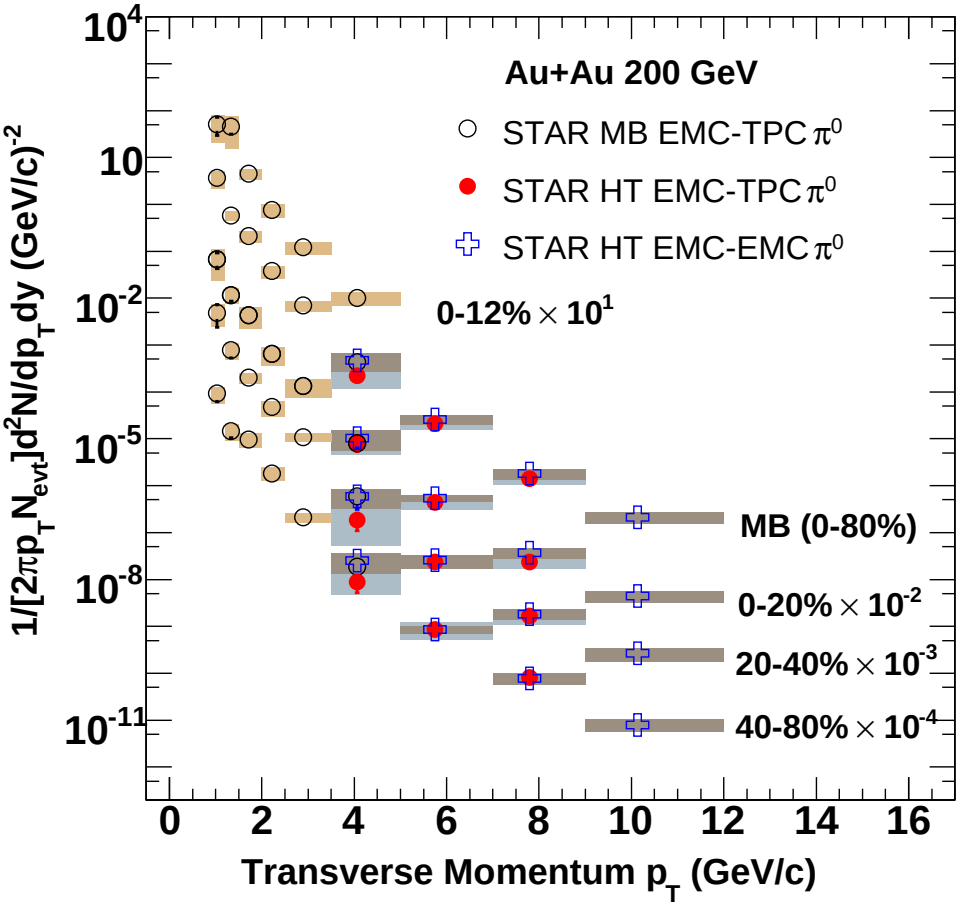

Figure 3.33: Invariant yield distribution of STAR π^0 as a function of p_T at mid-rapidity for different centrality bins in 200 GeV Au+Au collisions. Spectra for different centralities are scaled for clarity. Statistical errors are shown as vertical lines and point to point systematic errors are shown as bars.

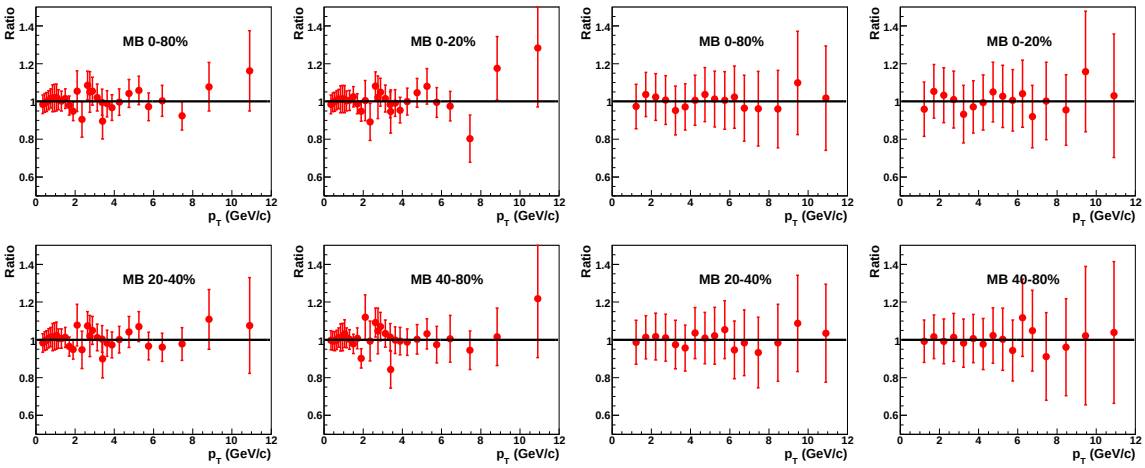

Figure 3.34: The ratio of STAR charged π (left) and PHENIX π^0 spectra over their fitting results for different centrality bins.

one caveat of this possibility is that it might contradict the results shown in Figure 3.11. Figure 3.11 shows that the reconstructed π^0 peak position from embedding is 5-10 MeV/c^2 lower than real data, which can indicate that the BEMC energy scale in data is too high. However, from Figure 3.30 of the energy scale study, increasing energy scale in embedding analysis to compensate the offset results in a decrease of the measured π^0 spectra, and therefore, would result in a larger difference between STAR π^0 and earlier π results.

3.4.2 Nuclear modification factors R_{CP} and R_{AA}

The nuclear modification factors R_{CP} and R_{AA} for pions is calculated from Equation 1.13 and 1.14. Figure 3.36 shows the nuclear modification factor R_{CP} for π^0 measured by STAR as a function of p_T in 200 GeV Au+Au collisions. When calculating R_{CP} many systematic uncertainties cancel out, such as the ones from BEMC energy scale and geometry correction, because they affect the π^0 spectrum for different centrality bins in the same direction and with roughly the same magnitude. Compared to the 40-80% peripheral Au+Au collisions, the more central collisions show a suppression of π^0 yield indicated by $R_{CP} < 1$ and the suppression is stronger for more central collisions. At high p_T above 4 GeV/c the π^0 R_{CP} is independent of p_T within uncertainties. The

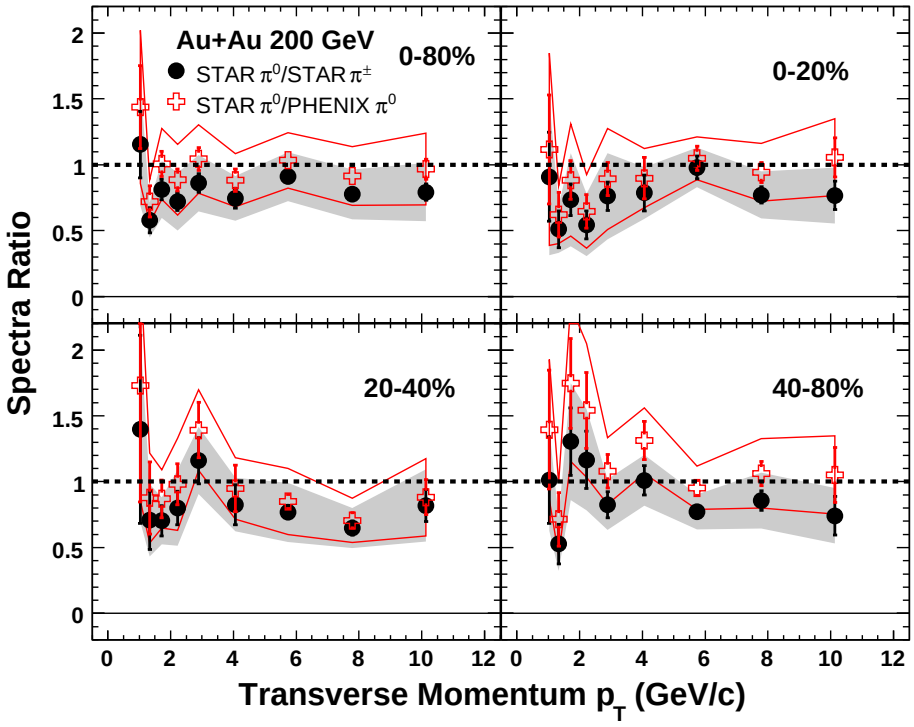

Figure 3.35: The ratios of STAR π^0 spectra over $\pi^{\pm}$ from STAR [71] (solid dot) and π^0 from PHENIX [16] (open cross) as a function of p_T for different centrality bins in 200 GeV Au+Au collisions. Statistical errors are shown as vertical lines and point to point systematic errors are shown as bands.

STAR π^0 shows the same magnitude of suppression as the STAR $\pi^{\pm}$ [71], which is shown by open circles.

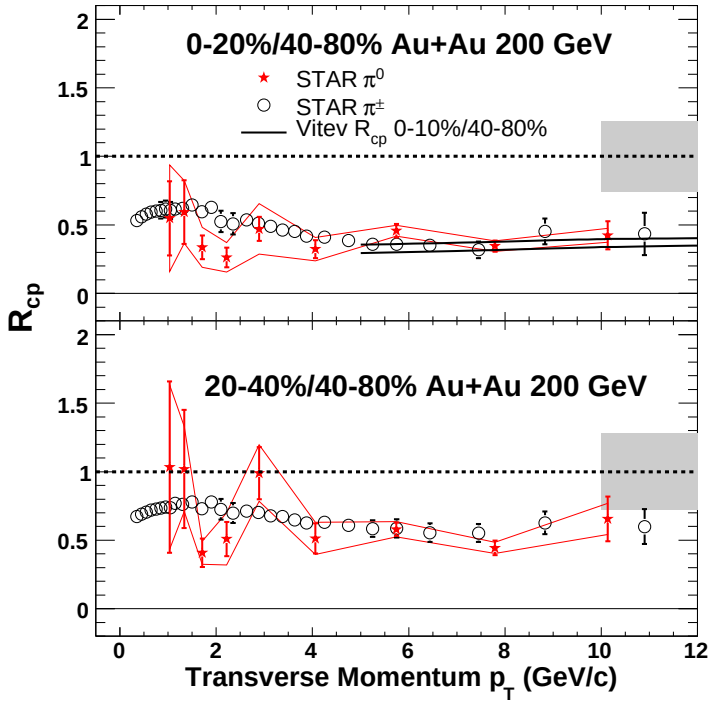

Figure 3.36: The nuclear modification factor R_{CP} as a function of p_T of STAR π^0 compared to STAR $\pi^{\pm}$ [71] in 200 GeV Au+Au collisions. Statistical errors are shown as vertical lines and point to point systematic errors are shown as horizontal lines. The shaded band on the right demonstrates the uncertainty of N_{bin}. The solid curves are jet quenching theoretical calculation [72].

Figure 3.37 shows the nuclear modification factor R_{AA} for π^0 measured by STAR as a function of p_T in 200 GeV Au+Au collisions. The π^0 spectrum in 200 GeV p+p collisions from Ref. [73] is used to calculate R_{AA}. The π^0 R_{AA} shows a similar centrality dependence to R_{CP} with stronger suppression in central collisions. In the most central Au+Au collisions a factor of 5 suppression of the π^0 yield relative to the nucleon-nucleon collisions is seen. For all the centrality bins, R_{AA} at high p_T for STAR π^0 agrees with earlier results of PHENIX [16].

The suppression of inclusive light quark meson production at high p_T in central

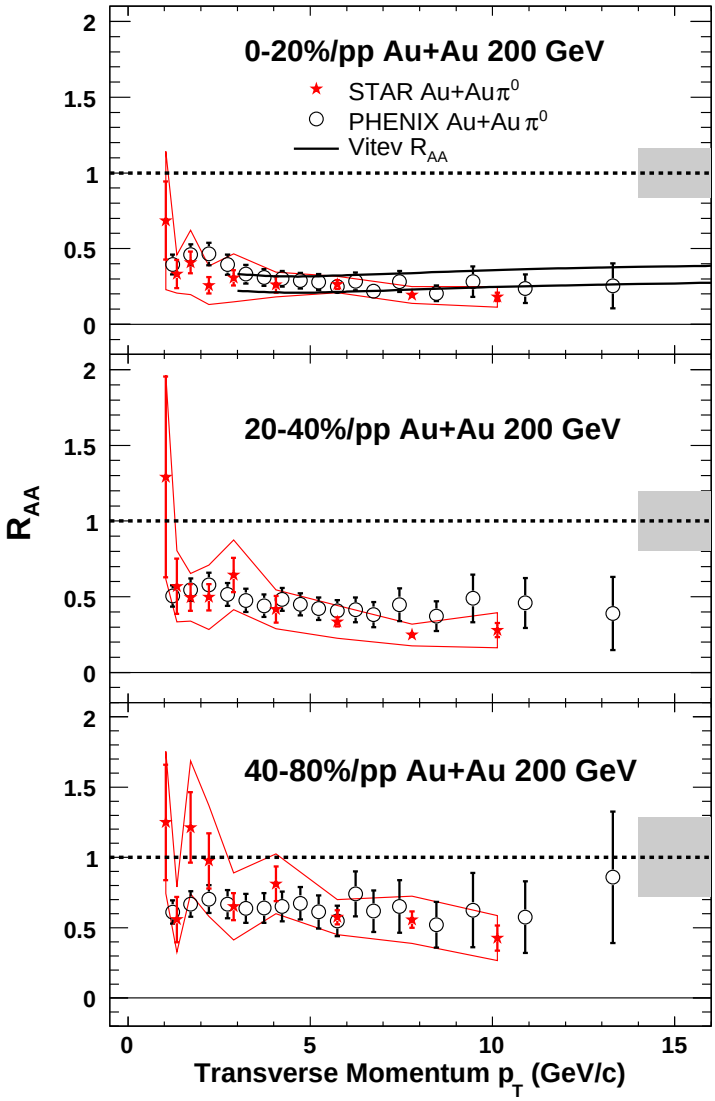

Figure 3.37: The nuclear modification factor R_{AA} as a function of p_T of STAR π^0 compared to PHENIX π^0 [16] in 200 GeV Au+Au collisions. Statistical errors are shown as vertical lines and point to point systematic errors are shown as horizontal lines. The shaded band on the right demonstrates the uncertainties of N_{bin} and the normalization error in p+p collisions. The solid curves are theoretical calculations in 0-10% Au+Au collisions [74].

heavy-ion collisions has been investigated by extensive model calculations. The nuclear modification factors R_{CP} and R_{AA} are used to reveal important parameters such as the initial gluon density [72, 74] and the medium transport coefficient $\hat{q}$ [75]. Recent study also suggests that the collisional energy loss may also play an important role in explaining energy loss of heavy quarks [76]. In Figure 3.36, theoretical calculations of jet quenching predictions with initial gluon density dN^g/dy=1150 in 0-10% Au+Au and between 100 and 150 in 40-80% Au+Au collisions [72] are shown as solid curves. In Figure 3.37, the calculations with dN^g/dy=800 to 1150 in 0-10% Au+Au collisions [74] are shown as solid curves too for comparison. In both figures data and theoretical predictions agree reasonably well, which indicates that the yield suppression of light quark mesons may be accounted for by the parton energy loss through gluon radiation.

3.4.3 Future analysis with run7 data

Au+Au 200 GeV data produced in 2007 RHIC run (run 7) will provide significantly more statistics for the π^0 production analysis. The advantages of run7 data include a higher HT trigger threshold of $E_T > 5.5$ GeV, a full BEMC coverage of $|\eta| < 1$, and much larger data sample of 605.7 μb^{-1} rare triggered events and 75.8×10^6 MB-VPD triggered events. So using run7 data can measure the π^0 production with higher precision and extend the spectra to higher p_T. A preliminary study of the run7 express stream data reveals that we can obtain a clear π^0 signal at as high as 12 GeV/c for the EMC-TPC method, and 15 GeV/c for the EMC-EMC method, which are shown in Figure 3.38.

3.4.4 Summary

We have presented the STAR results for the π^0 production in Au+Au collisions at $\sqrt{s_{\rm NN}}$=200 GeV. The π^0 spectra are measured over the range of 1< p_T <12 GeV/c using the combination of TPC conversion photons and BEMC photons. Despite the relatively large tower size, the STAR BEMC itself can reliably identify π^0 at high p_T above 4 GeV/c. The use of conversion photons significantly improves the π^0 invariant

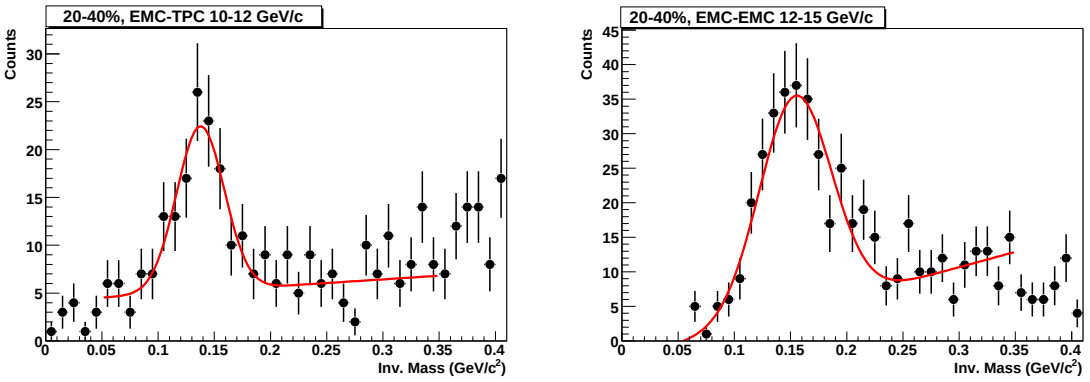

Figure 3.38: π^0 invariant mass distributions using 200 GeV Au+Au data in run7 express stream data sample for EMC-TPC (left) and EMC-EMC (right) methods.

mass signal at low and intermediate p_T and extends our study to a wide p_T range.

Compared to the STAR $\pi^{\pm}$ and PHENIX π^0, the overall STAR π^0 spectra are consistent with PHENIX π^0, and about 15% lower than STAR $\pi^{\pm}$, but still consistent within systematic errors. The nuclear modification factors R_{CP} and R_{AA} of the STAR π^0 are consistent with the earlier π results and the theoretical calculation based on jet quenching. At the most central Au+Au collisions the inclusive π^0 yield shows a factor of 5 suppression relative to the p+p collisions at high p_T. This result confirms the suppression of light mesons and provides additional evidence for the jet quenching picture.

Chapter 4

Direct Photon HBT

4.1 Photon reconstruction techniques

In this section the photon reconstruction technique is discussed. Similar to the π^0 analysis, photons are detected directly in the STAR BEMC or reconstructed through e^+/e^- tracks in the TPC.

4.1.1 Data set

The data presented in the photon HBT analysis are Au+Au events taken during the year 2004 RHIC run $\sqrt{s_{NN}} = 200$ GeV using the STAR TPC and BEMC. Only events selected by a minimum-bias trigger (MB) are analyzed, with the trigger ID of 15007. Due to the fact that the analysis was performed back in 2005, results shown here are from about 5×10^6 MB events, which is about 1/3 of the total statistics currently available. More details about the trigger and statistics can be found in Section 3.1.1.

Slightly different from the π^0 analysis, we require a vertex position within ± 30 cm from the detector center in z axis. As usual, a reference multiplicity requirement of RefMult>14 is applied to reject very peripheral events.

4.1.2 Photon reconstruction

Photons are reconstructed either directly from the electro-magnetic shower in the BEMC (EMC photon) or from e^+/e^- pairs in the TPC (TPC photon). The technique used to reconstruct the TPC photons is the same as shown in Section 3.1.3. For the EMC photons, a photon candidate is reconstructed as a cluster of up to 4 BEMC towers (2×2 layout) by adding the energy signal of neighboring towers to the tower with the highest energy in a local BEMC tower patch. The tower with the highest energy is required to have an energy of at least 700 MeV, and the total photon energy must be greater than 800 MeV. Both BSMD hits are required to determine the photon position. Each BSMD hit is a BSMD cluster of 1-5 BSMD strips. To remove the charged particle contamination, we require that no TPC global charged tracks hits the area of $\pm$ 0.05 in η and $\pm$ 0.05 in ϕ around the photon candidate. The EMC photon cuts used here are different from the ones used in the π^0 analysis using MB events. Here we desire a higher accuracy of photon position, so SMD hits are required even though the largest population of photons is at low p_T. The algorithm of using up to 4 towers is considered as being suboptimal now (see Section 3.1.2), but the tighter charged particle veto cut helps retain the photon purity.

4.1.3 Photon HBT correlation function

Photons are paired to calculate the HBT correlation function. Due to the limited statistics, only a one dimensional analysis of Q_{inv} is performed, where $Q_{inv} = \sqrt{p_0^2 - \boldsymbol{p}^2} = m_{inv}$ is the same as the di-photon invariant mass. The HBT signal lies in the small Q_{inv} region (Q_{inv} <50 MeV/c^2), so it demands high spatial and momentum resolution for close photons. Here we pair an EMC photon with a TPC photon. The advantage of this configuration is that two photons are reconstructed in two independent detectors, and therefore they can be arbitrarily close and not interfere with each other. In contrast, two close TPC photons may be affected by track merging which eliminates one of the e^+/e^- tracks and destroys the photon pair. The track splitting effect which splits a single e^+/e^- into two may create fake photons and hence fake correlations. In addition, the efficiency of reconstructing a TPC photon is very

small (∼2%), so pairing two TPC photons is also much more statistics demanding. For pairing two EMC photons, although the reconstruction efficiency is high, the minimal separation between two photons is limited by the BEMC to about 3 BSMD strips, which is equal to 0.02 in η or ϕ. So with two EMC photons we will fail to obtain any statistics at Q_{inv} <10-20 MeV/c^2, which is the critical region to extract the system size. Another advantage of using EMC-TPC photon pairs is that fake photons due to TPC track splitting or BEMC signal splitting won't create any fake HBT signal. Firstly, the fake photon is never paired with its sibling from which it is misidentified, because they are from the same detector (we only pair photons from two different detectors); secondly, any correlation duplicated by fake photons in the same-event distribution also takes place in the mixed-event distribution, so the effect is canceled in the ratio. As a summary, using EMC-TPC photon pairs is a more superior approach for the photon HBT analysis, with good balance between statistics and resolution.

The mixed event technique is employed to obtain the correlation function $C_2(Q_{inv})$. The Q_{inv} distributions of photon pairs from the same event and from different events are created. When creating the mixed-event distribution, we don't use the EMC photons in one event if they are close to the e^+/e^- daughter tracks of the TPC photons in the other event, so as to mimic the charged particle veto in the same-event distribution. The event pool method is implemented for the mixed-event distribution, where each event is mixed with up to 5 events with similar reference multiplicity, vertex z position, and reaction plane direction in a event pool. The same- and mixed-event pair distributions are normalized in the region of large Q_{inv} and the ratio of them is calculated, which is the correlation function $C_2(Q_{inv})$.

4.2 Results

4.2.1 Photon Q_{inv} correlation function

The one dimensional photon HBT correlation function ($C_2(Q_{inv})-1$) using EMC-TPC photon pairs is shown in Figure 4.1. All 0-80% MB events are combined in this figure. The correlation function approaches 0 at large Q_{inv} as a result of the normalization. The peak at $Q_{inv} \approx 135$ MeV/c^2 is the π^0 invariant mass signal. At low Q_{inv} region, we observe a significant peak with the magnitude of about 0.5. However, it is much larger than the expected HBT signal, which is about 10^{-3} considering the small fraction of direct photons. On the other hand, assuming that the real direct photon HBT signal has a magnitude of 10^{-3}, the statistical errors indicate that the current statistics are not enough to study the direct photon HBT correlation, even if the large peak were absent.

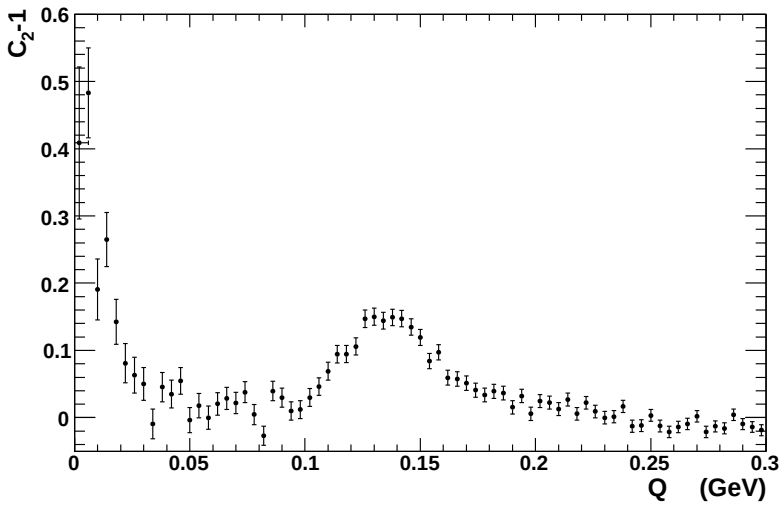

Figure 4.1: The photon HBT correlation function using EMC-TPC photon pairs in 200 GeV Au+Au collisions.

As a cross check, the correlation function using TPC photon pairs is shown in Figure 4.2. Similar to the EMC-TPC case, a strong peak is seen at small Q_{inv} region. When pairing two TPC photons, we require that the two photons should not share the same e^+/e^- track. This requirement is used to remove fake photons from random

track combinations which are close to a real photon. However, at the same time it may also reject real photons whose daughter track is lost due to track merging with a daughter track from another conversion photon, but is reconstructed via sharing that daughter track. As a result, it causes the "dip" structure at $Q_{inv} \approx 20$ MeV/c^2. Removing this requirement gets rid of the "dip" structure, and also produce a stronger peak at small Q_{inv}.

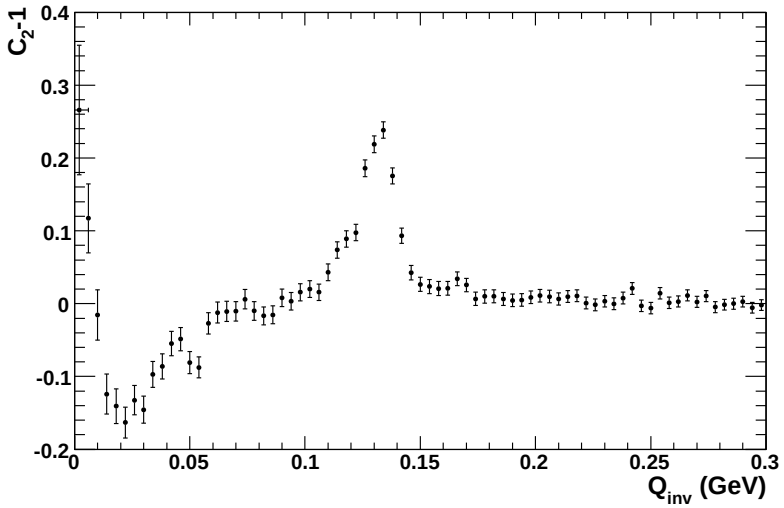

Figure 4.2: The photon HBT correlation function using TPC-TPC photon pairs in 200 GeV Au+Au collisions.

4.2.2 Study of the low Q_{inv} peak

We have attempted to determine the cause of the peak at small Q_{inv}. For photon HBT, the Q_{inv} can be written as

$$Q_{inv} = \sqrt{4E_1E_2\sin^2(\frac{\theta}{2})} \tag{4.1}$$

where E_1 and E_2 are energies of two photons, and θ is their opening angle. So firstly, the photon energy and pair opening angle distributions in different Q_{inv} regions (Q_{inv} <50 MeV/c^2 and Q_{inv} >50 MeV/c^2) are investigated, and photon pairs from the same- and mixed-event are compared. Figure 4.3 and 4.4 show the TPC and

EMC photon energy distributions in different Q_{inv} regions and in same- or mixed-event, as well as their ratios. They indicate no significant difference in photon energy in different Q_{inv} regions.

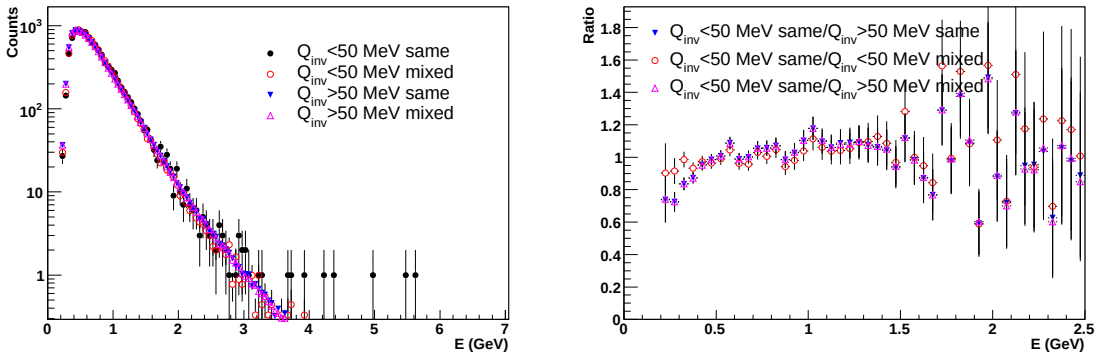

Figure 4.3: Left: The TPC photon energy distribution in different Q_{inv} regions for the same- and mixed-event photon pairs. Right: The ratios of the energy distributions.

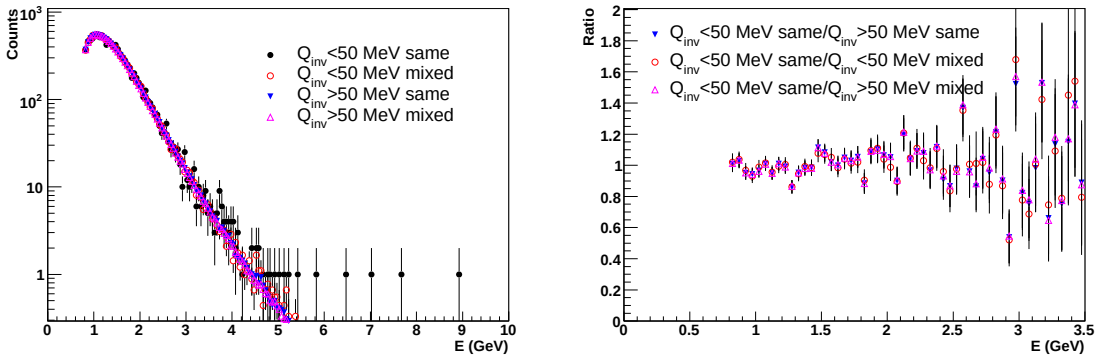

Figure 4.4: Left: The EMC photon energy distribution in different Q_{inv} regions for the same- and mixed-event photon pairs. Right: The ratios of the energy distributions.

Figure 4.5 shows the ratio of the opening angle distributions between the same- and mixed-event photon pairs, in Q_{inv} regions of Q_{inv} <50 MeV/c^2 and Q_{inv} >50 MeV/c^2. Above 50 MeV/c^2 there is no significant difference between the same- and mixed-event distributions, indicated by ratio$\sim$1. However, below 50 MeV/c^2 there is hint of an angular correlation between two photons in the same event. However, the reason for this possible angular correlation is still unknown.

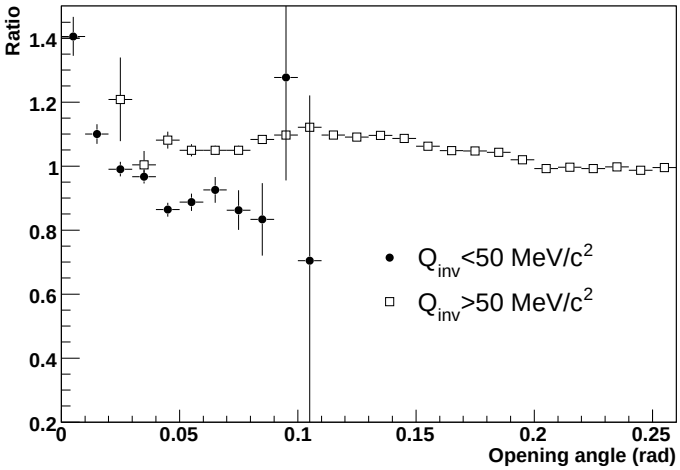

Figure 4.5: The ratio of the opening angle distributions of the same-event over the mixed-event photon pairs in different Q_{inv} regions.

Photons in different energy ranges are used to study the photon energy dependence of the small Q_{inv} peak. Figure 4.6 indicates that the small Q_{inv} peak is not affected by the cuts on the EMC photon energy. However, using low energy TPC photons helps reduce the magnitude of the peak, although it can not completely remove it.

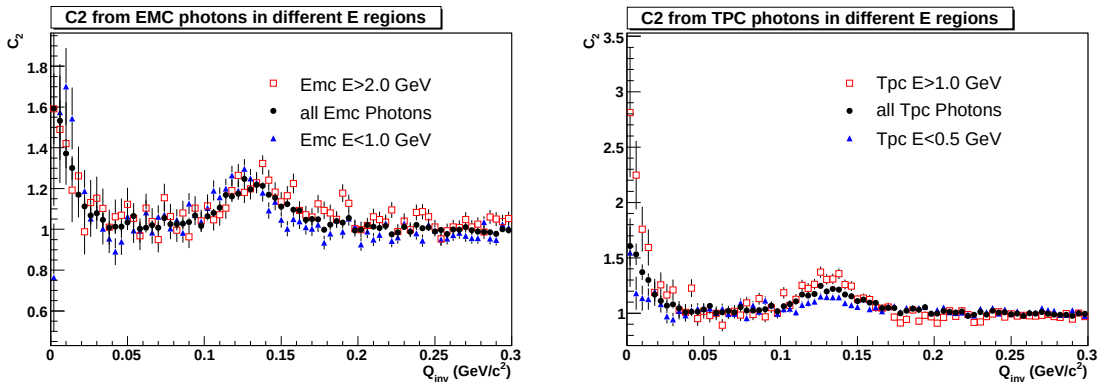

Figure 4.6: The photon HBT correlation functions using EMC (left) and TPC (right) photons from different energy ranges.

The TPC photon decay length dependence of the correlation function is studied and shown in Figure 4.7. The argument is that if we fail to reject the e^+/e^- daughter

tracks and accept their hits on the BEMC as EMC photons, they will create an angular correlation with their parent TPC photons. Using TPC photons converting with smaller decay length (farther away from BEMC) should help to reduce the peak because it takes longer for an e^+/e^- track to travel and they are farther away from their parent TPC photons if mis-identified. However, Figure 4.7 indicates that it is not the case.

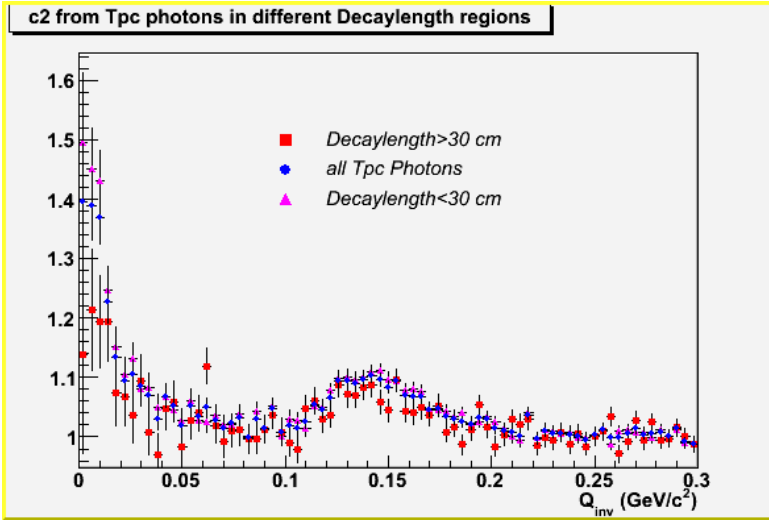

Figure 4.7: Photon HBT correlation function when using TPC photons with different decay lengths.

A more reliable source of TPC photons is photons converted in the inner field cage at $R \approx 45$ cm. The inner field cage is thin so the conversion point is well defined and should have better spatial resolution than photons converted elsewhere. As a result, only TPC photons converted at the inner field cage are selected and paired with each other. The correlation function is shown in Figure 4.8. Compared to Figure 4.2 which has the same cuts, the small Q_{inv} peak is significantly reduced, indicating that using photon sample with higher purity and resolution helps to remove the unknown peak.

There are also a couple of possible improvements for the photon HBT analysis. Firstly, using a single BEMC tower instead of a tower cluster to reconstruct EMC photons should eliminate a large amount of background from overlapping photons and

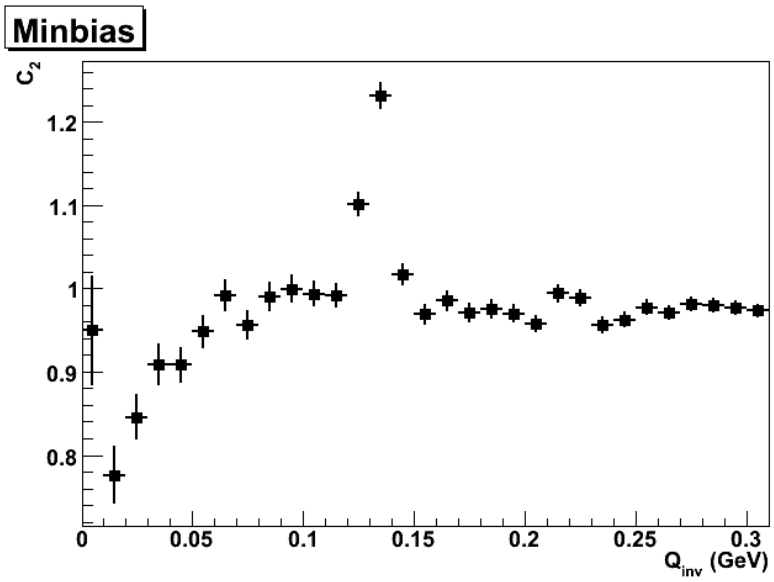

Figure 4.8: Photon HBT correlation function when only using TPC photons converted at the inner field cage.

other neutral or charged particles. Secondly, calculating background by a rotation method can remove the fake TPC photons from random combinations of e^+/e^- tracks. In this method the e^- tracks are rotated by 180° in the azimuthal plane, also with its origin point flipped with respect to the beam line. The rotated tracks are then paired with the e^+ tracks from the same event. "Photons" reconstructed in this way represent fake TPC photons from random combinations. By subtracting the correlation between the fake photons and real EMC photons from the total correlation function, we can remove the contribution from fake TPC photons. Unfortunately they are not implemented in the current analysis, but should be considered in the future.

4.2.3 Summary

As a summary, we observe a significant peak at the small Q_{inv} region in the photon HBT correlation function study. It is likely due to some angular correlation between photons. However, the reason for the peak structure has not be fully understood yet. The study using TPC photons converted in the inner field cage suggests that the peak might be a detector effect, because using a more reliable TPC photon sample helps

reduce the peak. More simulation work has to be performed to understand the small Q_{inv} peak, such as analyzing a large sample of HIJING events and comparing results from MC photons and photons in real data. The current statistics from run 4 data are not enough to further investigate the direct photon HBT correlation. In future analysis, more careful adjustment in photon reconstruction cuts should help reduce backgrounds and improve the correlation function, as stated above. This analysis is so critical in understanding the heavy-ion collisions that it should definitely be targeted in future RHIC runs and upgrades. In the next section we will briefly discuss the possible future STAR upgrades which will be crucial for the direct photon HBT analysis.

4.3 Future upgrades

In this section, several critical upgrades in STAR for the direct photon HBT analysis are discussed. Results from MC simulation are presented and the possibility of the analysis is evaluated. This simulation study is performed by Alexei Chikanian and Evan Finch [78] and is included here for completeness.

As shown in the last section, the current detector set up and statistics are not enough for further investigating the direct photon HBT. Considering its requirement of large statistics and efficient photon reconstruction, three critical upgrades of the STAR detector system are needed: DAQ upgrade, the photon converter, and the Shashlyk calorimeter [77].

4.3.1 DAQ Upgrade

The upgrade of DAQ system significantly enhances the performance of the data acquisition system so that an event collecting rate of 1000 Hz can be achieve, about 10 times as fast as the current rate. In 2008 RHIC run one TPC sector has implemented this upgrade, and the full upgrade was completed and took data in the 2009 RHIC run. Given the fact that we are likely to need about 10^9 central Au+Au events to perform a comprehensive, p_T dependent study of the direct photon HBT, the DAQ upgrade will significantly shorten the running time needed and make the analysis feasible.

4.3.2 Photon converter

A 0.1 radiation length lead photon converter concentric with the beam pipe with a radius of approximately 43 cm is proposed for portions of 2010 and 2011 RHIC runs [78]. The converter provides a simple and well defined geometry for reconstructing conversion photons, and therefore gives higher photon resolution with well known conversion points. The layout of the photon converter is shown in Figure 4.9.

We plan to only accept conversions which occur at the converter. MC simulation shows that the average detection efficiency, including the conversion probability and

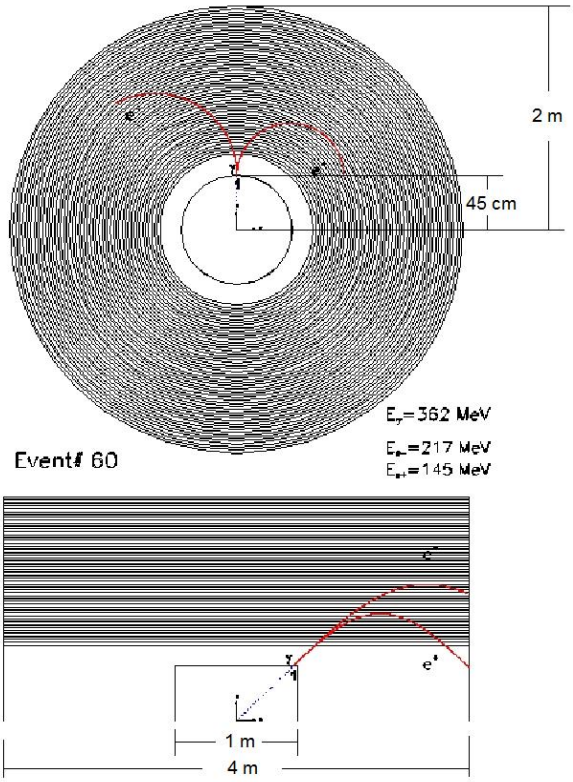

Figure 4.9: Layout of the photon converter and an example of photon converting at the converter.

reconstruction efficiency, is about 7%. It generally gives very good energy and angular resolution, with better resolution for larger incident angles of the photon into the converter and higher p_T photons. The results are shown in Figure 4.10.

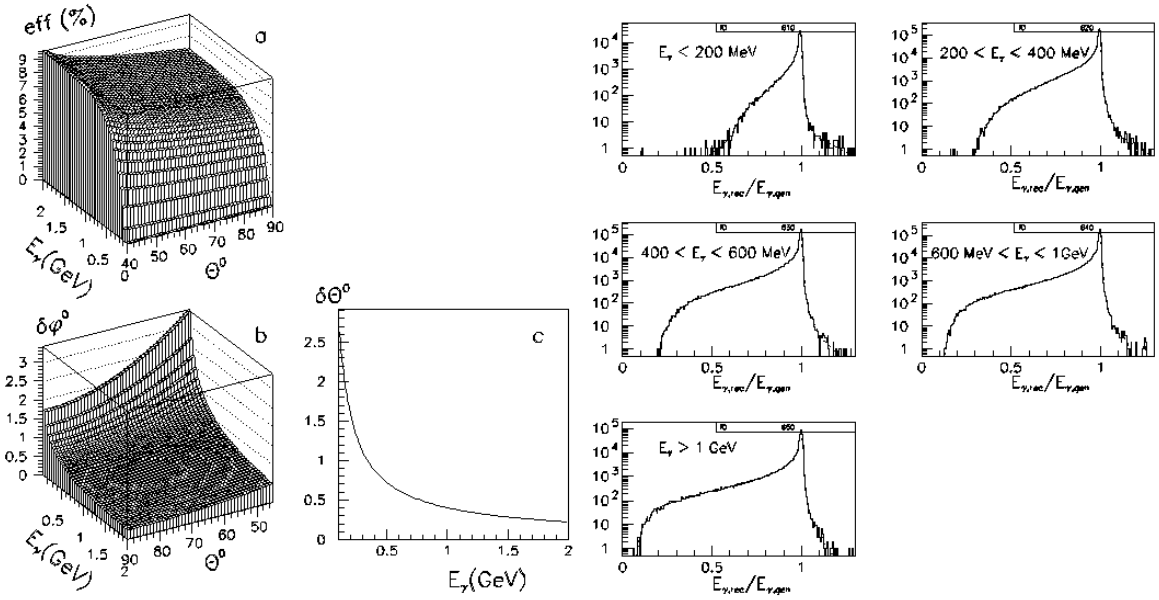

Figure 4.10: TPC conversion photon detection efficiency as a function of photon energy and incident angle (upper left). TPC photon reconstructed angular resolution as a function of photon energy and incident angle (lower left). TPC photon reconstructed energy resolution in different photon energy ranges (right).

Other physics topics involving photons will also benefit from the converter, such as the π^0, η, η', and other resonance analysis.

4.3.3 Shashlyk calorimeter

A Shashlyk calorimeter consists of alternating sheets of lead and scintillator with longitudinal wavelength shifting fibers. It can reach an energy resolution of $3\%/\sqrt{E}$ and the efficiency is essentially 100% for photons with energy down to 100 MeV [77]. It has a granularity of about 10×10 cm^2, and a Moliere radius of about 6 cm. The angular resolution can reach 10 mrad in θ and ϕ directions [77].

Compared to the current STAR calorimeter, the Shashlyk calorimeter can provide much better energy ($3\%/\sqrt{E}$ vs. $16\%/\sqrt{E}$) and spatial resolution, especially for low

energy photons. However, it is likely to be a long term upgrade, so the simulation results shown here only consider using photons reconstructed from the converter and current STAR calorimeter.

4.3.4 Simulation results

The EMC photon reconstruction algorithm is similar to the one used in the π^0 analysis in Section 3.1.2, but with a lower energy threshold, which requires that a peak tower energy is greater than 150 MeV and 75 MeV greater than its neighbor towers.

Again EMC-TPC photon pairs are used to extract the direct photon HBT signal from simulated data. In one week of data collection for year 2009 run with DAQ upgrade, it is expected that we could collect 50×10^6 central Au+Au events. The simulated 1-D HBT correlation function integrated over all k_T for such an event sample is shown in Figure 4.11 [78]. Comparing the correlation functions with HBT effect turned on and off, we believe that it may well be possible to measure the direct photon HBT signal.

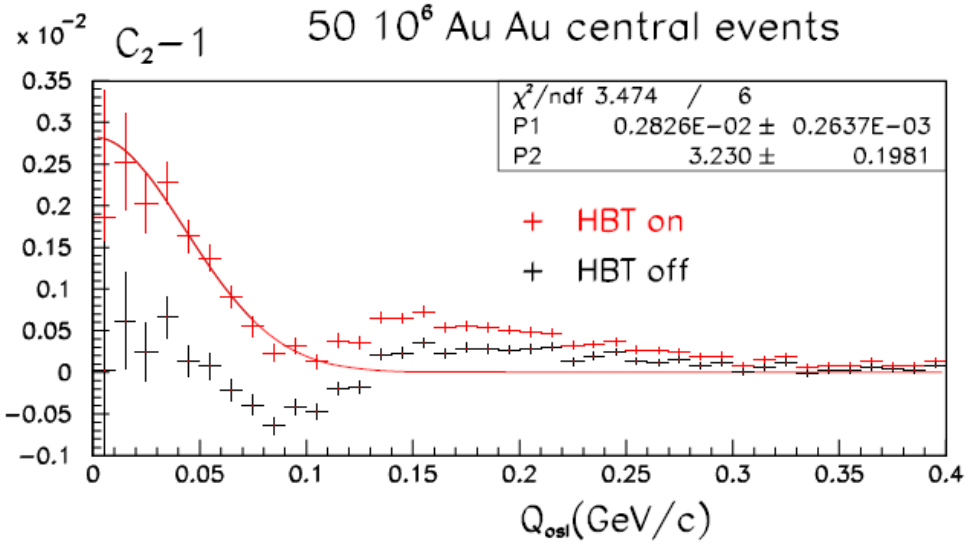

Figure 4.11: Expected 1-D HBT correlation function for photons as a function of Q_{osl} for 50×10^6 central Au+Au events. The black histogram is the same simulation done with HBT turned off.

It has also been estimated how many events are required to perform a 3-D HBT

Analysis to be done	Statistics required
3-D & all p_T spectrum	300×10^6 events
3-D & $p_T < 300$ MeV	350×10^6 events
3-D & $(300 < p_T < 600)$ MeV	800×10^6 events
3-D & $p_T > 600$ MeV	20×10^9 events

Table 4.1: Number of central Au+Au events required to perform a 3-D HBT analysis in different p_T ranges.

analysis and extend it to a higher p_T range, based on the statistical error bars of our current simulation event sample. The results are shown in Table 4.1 [78].

The numbers above show how statistics demanding the direct photon HBT analysis is. Nevertheless, it would reveal such valuable space-time information about the collision system that we should never stop pursuing it.

Chapter 5

Photon Elliptic Flow

5.1 Photon v_2 measurement techniques

In this section the inclusive photon reconstruction technique and the elliptic flow (v_2) calculation methods are discussed. High p_T photons are reconstructed from the high tower triggered data sample, and the inclusive photon v_2 is calculated using the reaction planes determined by the charged tracks in the TPC and FTPC.

5.1.1 Data set

The data presented in the photon v_2 analysis are Au+Au events taken during the year 2004 RHIC run at the energy of $\sqrt{s_{NN}} = 200$ GeV using the STAR TPC, FTPC, and BEMC. Only events selected by a high tower trigger (HT) are analyzed. The HT trigger requires that at least one BEMC tower has an energy of $E_T = E * \sin\theta > 3/\sin\theta$ GeV, where θ is the polar angle of the tower with respect to the detector center [61].

To select events with good quality, we require a vertex position within ± 30 cm from the detector center in the z axis. As usual, a reference multiplicity requirement of RefMult>14 is applied to reject very peripheral events. We also require that the ratio $R = \frac{E_{BEMC}}{E_{BEMC}+E_{TPC}}$ is less than 0.8 to remove the beam background. For more details about the beam background, please refer to Section 3.1.1. After event selection

2.2×10^6 HT events were analyzed. Due to the difficulty of measuring v_2 in very central and peripheral collisions, only results from centrality bins of 5-20%, 20-60% will be shown.

5.1.2 Photon reconstruction

As stated in Section 1.2.3, the direct photon v_2 is mostly interesting at intermediate to high p_T. In addition, the fraction of direct photons among inclusive photons at low p_T is so small that separating contribution of direct photon v_2 from inclusive photons is formidable. As a result, we will focus on photon v_2 measurement at high p_T using HT events: only photons with energy above the HT trigger threshold are accepted, which means that at least one BEMC tower of the photon has energy of $E > 3/\sin^2\theta$ GeV.

Photons are reconstructed using two slightly different methods: 1. a photon consists of up to 4 BEMC towers with a 2×2 layout; 2. a photon is reconstructed from a single tower. The reason for using a cluster of 4 BEMC towers is to measure the photon energy more accurately when a photon hits the boundary of a tower and parts of its energy are deposited into neighboring towers. Considering the high energy of photon candidates, the smearing from other background particles is less troublesome. In both methods two BSMD hits are required to determine the photon position. Each BSMD hit consists of 2-5 strips with the most energetic strip above 0.4 GeV. Charged particle contamination is removed by requiring that the total momentum of TPC charged tracks projected to the area of $\pm$ 0.05 in η and $\pm$ 0.05 in ϕ around the photon candidate should be less than 1 GeV/c. The pseudo-rapidity range of reconstructed photons is $0 < \eta < 0.9$ to avoid the beam background at forward direction. Hot towers are rejected.

5.1.3 Event plane measurement from TPC and FTPC

The direction of the event plane is determined by charged tracks in the TPC and FTPC. Qualified tracks with p_T less than 2 GeV/c are used to calculate the Q-vector, which will reveal the estimated reaction plane direction. The cuts used for track

selection are listed in Table 5.1.

$$\begin{aligned} Q_x &= \sum_{i=1}^{N} w_i \cos(2\phi_i) \\ Q_y &= \sum_{i=1}^{N} w_i \sin(2\phi_i) \end{aligned} \tag{5.1}$$

where the sum goes over all the particles used in event plane calculation for that event, and ϕ_i is each track's azimuthal angle. For tracks in the TPC, the weights w_i include a p_T weight which is equal to the value of the charged track's p_T in GeV/c, and a ϕ weight which corrects for the TPC acceptance mainly due to the gaps between TPC sectors. The use of p_T weight is due to the fact that v_2 of charged particles is roughly linear with p_T in the low p_T range, and a track with larger v_2 should have more weight in determining the event plane. The ϕ weight is equal to the average charged track density over the charged track density at that ϕ position:

$$w(\phi) = \frac{\int_0^{2\pi} \frac{dN(\phi)}{d\phi} d\phi / 2\pi}{\frac{dN(\phi)}{d\phi}} \tag{5.2}$$

where $\frac{dN(\phi)}{d\phi}$ is obtained from real data. For tracks in the FTPC, the weights w_i are all equal to 1 in contrast. However, it should be noted that results using different weighting factors are consistent with each other. The final FTPC Q-vectors are re-centered run by run by shifting the event-by-event Q-vector by a constant value, so that the average $\langle Q_x \rangle$ and $\langle Q_y \rangle$ are 0 over all events in the same centrality in each run. The purpose of this procedure is similar to the ϕ weight used in the TPC method. Because the FTPC has some dead regions with significantly lower efficiency, the method of applying ϕ weights gives larger uncertainty, or is even un-doable in those regions. Finally we obtain three $Q-$vectors from the TPC and FTPC individually, two Q_E and Q_W from the east and west TPC and FTPC, and one total $Q = Q_E + Q_W$. The Q-vector reveals the event plane direction, which is called the 2nd order event plane.

$$\Psi_2 = \tan^{-1}(\frac{Q_y}{Q_x})/2 \tag{5.3}$$

Cuts	TPC tracks	FTPC tracks
Track type	Primary	Primary
N_{fit}	$15 \leq N_{fit} \leq 50$	$5 \leq N_{fit} \leq 10$
$\frac{N_{fit}}{N_{poss}}$	$0.52 \leq \frac{N_{fit}}{N_{poss}} \leq 1.21$	N/A
η	$\|\eta\| \leq 1.0$	$2.5 \leq \|\eta\| \leq 4.0$
p_T	$0.1 \leq p_T \leq 2.0$ GeV/c	$0.1 \leq p_T \leq 2.0$ GeV/c
global DCA	DCA$\leq$ 1 cm	DCA$\leq$ 2 cm

Table 5.1: Cuts used to select TPC and FTPC charged tracks for event plane calculation.

5.1.4 Scalar product method

The most commonly used method to calculate elliptic flow is the event plane method [36]. The azimuthal distribution of particles with respect to the event plane is calculated, and the observed v_2 is obtained as:

$$v_2^{obs} = \langle \cos[2(\phi - \Psi_2)] \rangle \tag{5.4}$$

where the angle brackets denote an average over all particles in a given phase space from all events. Due to the finite multiplicity, the estimated event plane does not accurately represent the true reaction plane, so the v_2^{obs} should be corrected by the event plane resolution to obtain the final true v_2:

$$v_2 = \frac{v_2^{obs}}{\langle \cos[2(\Psi_2 - \Psi_r)] \rangle} \tag{5.5}$$

where the brackets average over a large event sample. The event plane resolution is estimated by the correlation of event planes in two subevents Ψ_2^A and Ψ_2^B:

$$\langle \cos[2(\Psi_2 - \Psi_r)] \rangle = C \langle \cos[2(\Psi_2^A - \Psi_r)] \rangle = C \sqrt{\langle \cos[2(\Psi_2^A - \Psi_2^B)] \rangle} \tag{5.6}$$

where C is a constant calculated from the known multiplicity dependence of the resolution [36]. Charged tracks in the TPC can give an event plane resolution of about 30°, with worse resolution obtained from the FTPC and the Shower Maximum Detectors of the Zero Degree Calorimeters (ZDCSMD).

In this analysis we use the scalar product method [37] to calculate the inclusive photon v_2. This method is more convenient than the event plane method because,

instead of calculating v_2^{obs} and correcting for the event plane resolution in two steps, one obtains the final v_2 directly. For the case of using FTPC tracks, the photon v_2 can be calculated in 1, 2, or 4 terms, using the combination of two FTPC Q-vectors. Equation 5.7 uses the full FTPC Q-vector:

$$v_2 = \frac{\langle uQ^* \rangle}{2\sqrt{\langle Q_E Q_W^* \rangle}}. \tag{5.7}$$

Equation 5.8 uses two individual Q-vectors:

$$\begin{aligned} v_2 &= \frac{\langle uQ_E^* \rangle}{\sqrt{\langle Q_E Q_W^* \rangle}} \\ v_2 &= \frac{\langle uQ_w^* \rangle}{\sqrt{\langle Q_E Q_W^* \rangle}}. \end{aligned} \tag{5.8}$$

Equation 5.9 uses the x and y components of two Q-vectors:

$$\begin{aligned} v_2 &= \frac{1}{\langle \cos^2 2\phi_\gamma \rangle} \frac{\langle u_x Q_{Ex} \rangle}{\sqrt{2\langle Q_{Ex} Q_{Wx} \rangle}} \\ v_2 &= \frac{1}{\langle \cos^2 2\phi_\gamma \rangle} \frac{\langle u_x Q_{Wx} \rangle}{\sqrt{2\langle Q_{Ex} Q_{Wx} \rangle}} \\ v_2 &= \frac{1}{\langle \sin^2 2\phi_\gamma \rangle} \frac{\langle u_y Q_{Ey} \rangle}{\sqrt{2\langle Q_{Ey} Q_{Wy} \rangle}} \\ v_2 &= \frac{1}{\langle \sin^2 2\phi_\gamma \rangle} \frac{\langle u_y Q_{Wy} \rangle}{\sqrt{2\langle Q_{Ey} Q_{Wy} \rangle}}. \end{aligned} \tag{5.9}$$

Here $u = \cos 2\phi_\gamma + i \sin 2\phi_\gamma$ is the vector for a photon candidate, and the scalar product of two vectors $uQ^* = u_x Q_x + u_y Q_y$. The average is over all the events, so the scalar product can also be written as:

$$uQ^* = \langle \sum_i \cos 2(\phi_\gamma - \phi_i) \rangle \tag{5.10}$$

where the sum goes over all charged particles that determine the event plane. The factor of $\frac{1}{\langle \cos^2 2\phi \rangle}$ and $\frac{1}{\langle \cos^2 2\phi \rangle}$ are used to correct the asymmetry of the detector in x and y directions. In an ideal case these two terms are equal to 2. Multiple terms of v_2 are added and averaged using their reciprocal of error as weight to obtain the final v_2. In the v_2 calculation above, the numerator is analogous to the v_2^{obs}, and the denominator is analogous to the event plane resolution in the event plane method.

The reason for using FTPC tracks to calculate the event plane is to take advantage of the pseudo-rapidity gap between the FTPC and the BEMC and suppress the non-flow effects at high p_T. The non-flow effects are correlations not associated with the reaction plane, including resonance decay, HBT correlations, final state interactions, and jets, which become more significant at high p_T. Most of them are short range correlations, so a pseudo-rapidity gap helps to remove them. To ensure that the FTPC event plane will give reasonable v_2 results and effectively suppress the non-flow effect, several QA checks on charged particle v_2 have been performed. Firstly, four terms of the v_2 in Equation 5.9 are calculated and compared in Figure 5.1, their agreement indicates the robustness of the FTPC method.

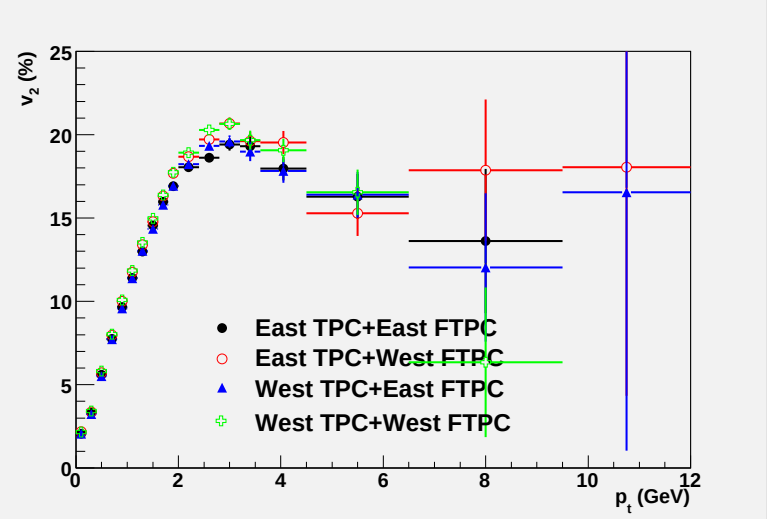

Figure 5.1: The comparison of four terms of charged particle v_2 using Q-vectors calculated from FTPC tracks.

The charged particle v_2 from the FTPC method is also compared to results from the two- and four-particle cumulant methods ($v_2\{2\}$ and $v_2\{4\}$) in Figure 5.2. It has been known that the four-particle cumulant method is able to remove most of the non-flow effects, and the two-particle cumulant method keeps most of them. On the other hand, v_2 fluctuations lead to an increase in the $v_2\{2\}$ values and an equal amount of decrease in the $v_2\{4\}$ values [79]. As a result, the true v_2 values should be between $v_2\{2\}$ and $v_2\{4\}$, closer to the $v_2\{4\}$ values. The FTPC method is expected

to have similar sensitivity to v_2 fluctuations as the two-particle cumulant method, so the difference between $v_2\{2\}$ and $v_2\{FTPC\}$ is the non-flow contribution suppressed by the pseudo-rapidity gap. Figure 5.2 indicates that the FTPC method effectively suppresses the non-flow effect and $v_2\{FTPC\}$ is a good estimate of the true v_2.

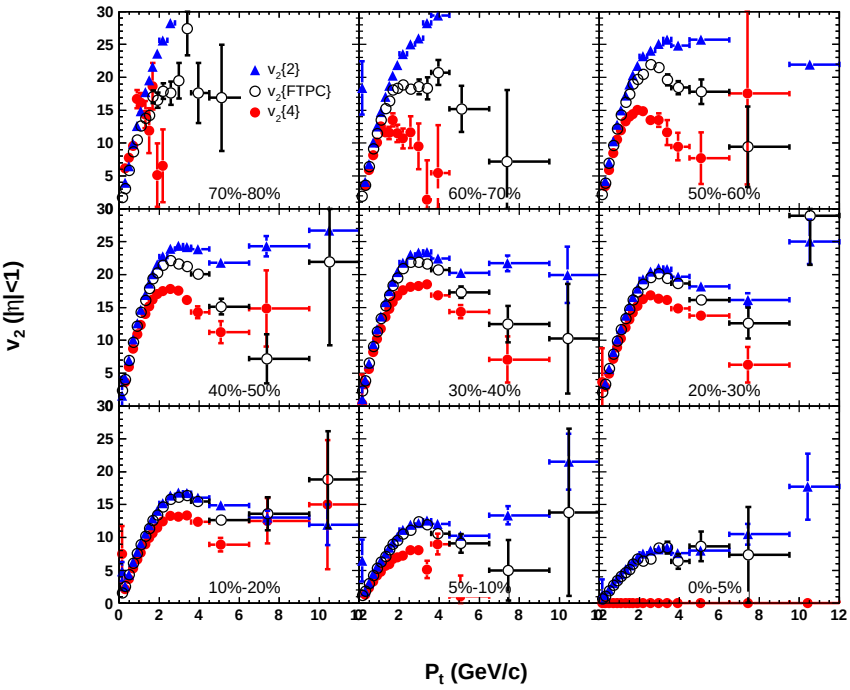

Figure 5.2: The comparison of charged particle v_2 from FTPC method to v_2 from two- and four-particle cumulant methods in different centralities bins.

The Q-vector obtained from the main TPC can also be used to calculate the photon v_2. However, due to the lack of pseudo-rapidity gap between the TPC and BEMC, the non-flow contribution needs to be subtracted. The scalar product in Au+Au collisions can be written as the sum of one term related to the true v_2 and the other term of non-flow contribution:

$$\langle uQ^* \rangle^{AA} = (v_b v_p + \delta_{bp}^{AA}) M^{AA} \tag{5.11}$$

where v_p is the flow of photons in a specific p_T and η bin, v_b and M^{AA} are the average

flow and the number of charged tracks used to define the event plane, and δ_{bp} is the non-flow correlation per charged track. The per-particle non-flow contribution in Au+Au collisions is diluted compared to p+p collisions, and they are approximately related by a factor of number of binary collisions N_{bin}:

$$\delta_{bp}^{AA} \approx \frac{\delta_{bp}^{pp}}{N_{bin}} \approx \frac{\delta_{bp}^{pp} M^{pp}}{M^{AA}} \tag{5.12}$$

As a result, the scalar product in Au+Au collisions can be approximated as:

$$\langle uQ^* \rangle^{AA} \approx v_b v_p M^{AA} + \langle uQ^* \rangle^{pp} \tag{5.13}$$

which means that by subtracting the scalar product from p+p collisions, we are able to subtract a large fraction of the non-flow contribution. Here we call it the TPC-pp method. The real data also support this approach. Figure 5.3 shows that the scalar product of p+p mimics the very peripheral Au+Au, as well as the central Au+Au collisions at high p_T, where small v_2 and large non-flow contribution are expected [80]. As a result, the scalar product of p+p should be a good approximation of the non-flow contribution in Au+Au.

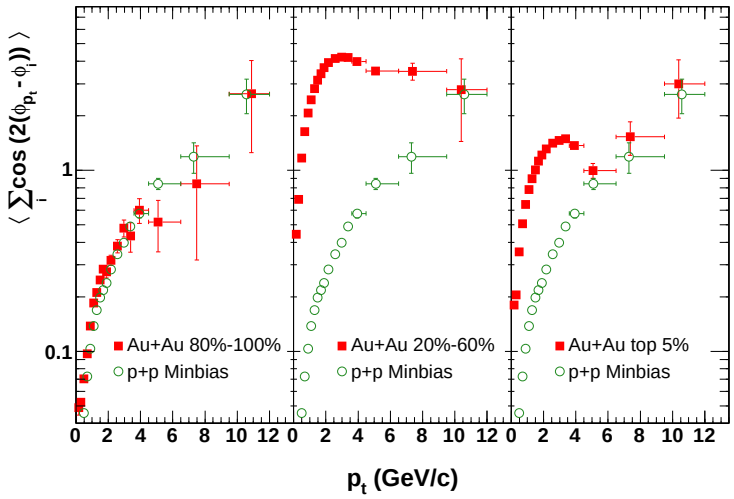

Figure 5.3: Azimuthal correlations in Au+Au collisions as a function of centrality compared to minimum bias azimuthal correlations in p+p collisions [80].

The difference between Au+Au and p+p scalar products is then divided by the averaged v_2 and the multiplicity of the charged particles in the TPC, and it gives

the v_2 of inclusive photons. A more convenient way is again to take advantage of the scalar product method. Note that $v_b M^{AA} = 2\sqrt{\langle Q_E Q_W^* \rangle}$, so the inclusive photon v_2 using the TPC-pp method can be calculated as

$$v_2 = \frac{\langle uQ^* \rangle^{AA} - \langle uQ^* \rangle^{pp}}{2\sqrt{\langle Q_E Q_W^* \rangle}}. \tag{5.14}$$

It should be noted that this method is somewhat model dependent and less fundamental than other v_2 calculation methods. The approximation of non-flow contribution using p+p data might not be valid in all centralities and p_T ranges. As a result, this method is mainly used as a cross check to the v_2 calculated from the FTPC method.

An example of the scalar product between inclusive photons and charged particles in the TPC in 40-50% Au+Au and HT p+p collisions is shown in Figure 5.4. Photons reconstructed by both algorithms are presented. The HT p+p events are used to increase the statistics at high p_T. However, in Equation 5.14 $\langle uQ^* \rangle^{pp}$ represents the scalar product in MB p+p collisions, and the HT p+p events are biased towards collisions with higher multiplicity, which will over-estimate the scalar product. As a result, the scalar product from HT p+p events is scaled down by a factor of M_{MB_pp}/M_{HT_pp}, where M_{MB_pp} and M_{HT_pp} are the average numbers of charged tracks used to calculate the Q-vectors in MB and HT p+p events.

5.1.5 v_2 correction for charged particle veto cut

We are still one step away from obtaining the inclusive photon v_2. The measured inclusive photon v_2 above will be smaller than the true v_2 due to the charged particle veto cut: the charged particle density is higher in the reaction plane direction, where a photon candidate is more likely to be rejected.

This effect in principle depends on the charged particle multiplicity, v_2 and even the spectral shape, considering different charged particle veto cuts. In the case of a simple veto cut of rejecting a photon if any charged track is projected to the area of $\pm$ 0.05 in η and $\pm$ 0.05 in ϕ around the photon candidate, the correction can be calculated analytically. We assume the number of charged particles is N in the phase

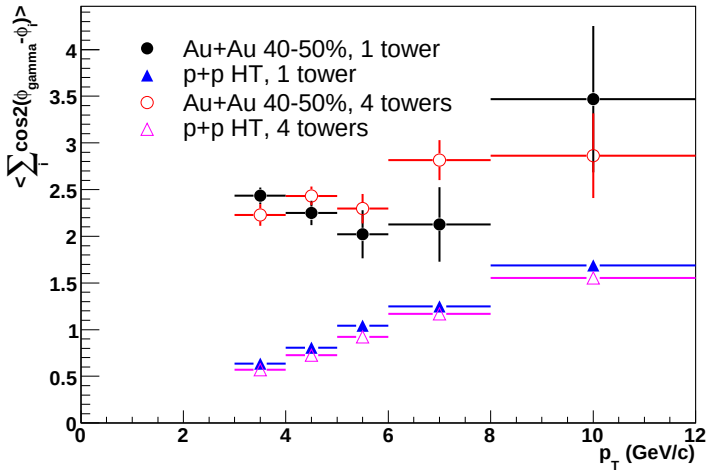

Figure 5.4: Azimuthal correlations between inclusive photons and charged particles in the TPC in 40-50% Au+Au and MB p+p collisions as a function of p_T.

space of $0 < \phi < 2\pi$ and $0 < \eta < 1$ with flat η distribution, and their average v_2 is v_2^{ch}. The charged particle azimuthal distribution is:

$$\frac{d^2N}{d\phi d\eta} = \frac{N}{2\pi}[1 + 2v_2^{ch}\cos 2\phi]. \tag{5.15}$$

For one charged particle, the probability, p_{in}, that it hits a 0.1×0.1 area centered at a photon position of (η_0, ϕ_0) is:

$$p_{in} \approx \frac{0.1 \times 0.1}{2\pi}[1 + 2v_2^{ch}\cos 2\phi_0]. \tag{5.16}$$

For N charged particles and small p_{in}, the probability that none of them hits the same area is:

$$p = (1 - p_{in})^N \approx 1 - Np_{in} = 1 - \frac{0.01N}{2\pi}[1 + 2v_2^{ch}\cos 2\phi_0]. \tag{5.17}$$

After applying the charged particle veto cut, the photon distribution becomes:

$$\begin{aligned}
\frac{d^2N^\gamma}{d\phi d\eta} &\propto [1 + 2v_2^\gamma \cos 2\phi] \times p \\
&= [1 + 2v_2^\gamma \cos 2\phi]\{1 - \frac{0.01N}{2\pi}[1 + 2v_2^{ch}\cos 2\phi]\} \\
&\approx 1 - c + 2(1-c)v_2^\gamma \cos 2\phi - 2cv_2^{ch}\cos 2\phi \\
&= (1-c)(1 + 2(v_2^\gamma - \frac{c}{1-c}v_2^{ch})\cos 2\phi)
\end{aligned} \tag{5.18}$$

where $c \equiv \frac{0.01N}{2\pi}$ and the higher order term of $\cos^2 2\phi$ is neglected. The measured photon v_2 turns out to be:

$$v_2^{measured} = v_2^{true} - \frac{c}{1-c} v_2^{ch}. \tag{5.19}$$

The difference between the true v_2 and the measured v_2 does not depend on the true v_2, but only on the charged particle v_2 and multiplicity.

The charged particle veto cut in this analysis is slightly more complicated, requiring that the total momentum of TPC charged tracks projected to the area of $\pm$ 0.05 in η and $\pm$ 0.05 in ϕ around the photon candidate should be less than 1 GeV/c. So the correction depends on the charged particle spectrum too and can not be calculated analytically easily. Therefore the correction is done through simulation. In the simulation charged particles are generated according to the measured inclusive spectra and $v_2(p_T)$ values. Photons are generated with flat p_T distribution and with the same $v_2(p_T)$ as charged particles. The photon v_2 measured after the charged particle veto cut is compared to the input and shown in Figure 5.5. Although with a more complex charged particle veto cut, the conclusion that the correction is independent of the input v_2 is still true. As a result, a constant photon v_2 correction is applied in each centrality bin. The correction is larger in more central collisions.

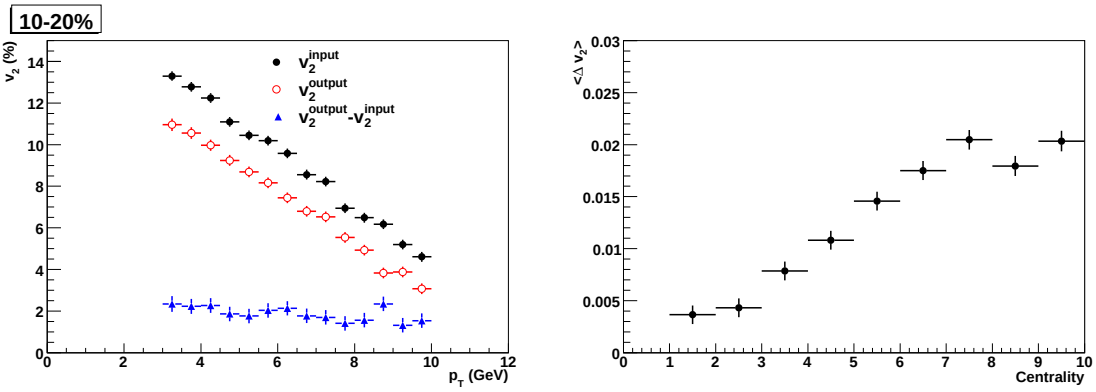

Figure 5.5: Left: The comparison of photon v_2 after applying the charged particle veto cut to the input v_2 in simulation. Their difference is also shown. Right: the average v_2 correction for the charged particle veto cut as a function of centrality in Au+Au collisions. Here a larger number in the x axis represents more central collisions.

5.2 Decay photon v_2

In this section the technique of calculating the decay photon v_2 using the π^0 embedding data sample is discussed. The decay photon v_2 is derived from results of the known STAR $\pi^{\pm}$ v_2 and PHENIX π^0 spectra.

5.2.1 STAR BEMC's response to high-p_T π^0

As discussed in the last section, two algorithms have been implemented to reconstruct inclusive photons. Although the two algorithms only differ in the number of towers used as a photon candidate, they response to photons and π^0's distinctly, as shown below. Simulations generating pure high p_T ($p_T > 3$ GeV/c) photons and π^0s give results in Figure 5.6, which shows the ratio of reconstructed particle p_T over its MC counterpart for two photon reconstruction algorithms.

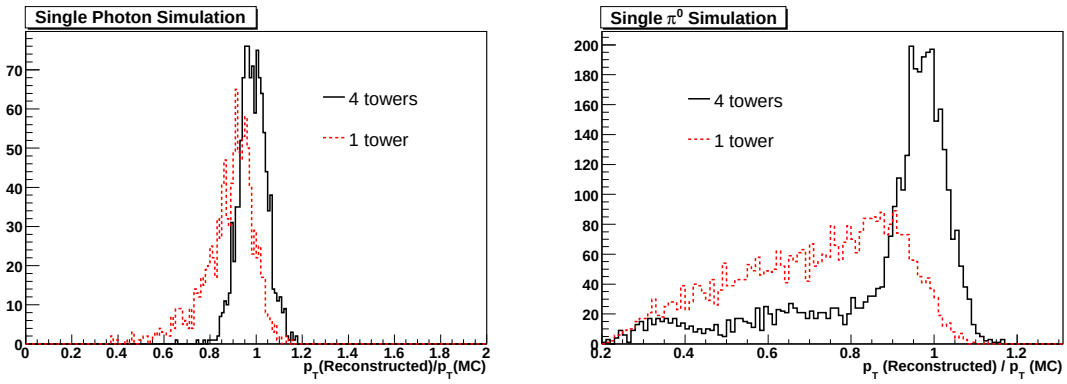

Figure 5.6: Ratio of reconstructed photon p_T over MC photon p_T (left) and π^0 p_T (right) for two photon reconstruction algorithms.

As expected, the algorithm using 4 towers is able to recover the single photon p_T better than a single tower. However, the π^0 simulation indicates that, instead of reconstructing the decay photons, the algorithm using 4 towers actually finds the π^0 itself. Using single tower seems to do a better job, although it still tends to reconstruct something closer to the π^0 p_T.

The difference between two algorithms is due to the STAR BEMC's response to

high p_T π^0's. According to the decay mechanism of π^0, the invariant mass is equal to

$$m_{\pi^0} = \sqrt{4E_1E_2\sin^2\frac{\theta}{2}} \tag{5.20}$$

where E_1 and E_2 are photon energies, and θ is their opening angle. θ is minimal when the decay is completely symmetric, or $E_1 = E_2$, so

$$\theta_{min} = 2\sin^{-1}\frac{m_{\pi^0}}{2E} \approx \frac{m}{E}. \tag{5.21}$$

Due to the relatively large BEMC tower size (0.05×0.05 in $\Delta\eta \times \Delta\phi$), two decay photons from a single π^0 have chances of hitting the same tower when the π^0 p_T is above 6 GeV/c, and start hitting the same cluster of 4 towers above 3 GeV/c. So two photons are more likely to merge into one when using 4 towers. When the merging happens, we rely on the BSMD to separate them. However, the BSMD efficiency remains relatively low for low p_T photons: the probability for a photon with E >6 GeV to leave signal in the BSMD is 60-80% and it drops to less then 20% at E <2 GeV [81]. Therefore, the chance of detecting the merging of two photons, or the π^0 itself, is significantly higher when using a cluster of 4 towers. Since decay photons are dominating in the final state, and we are essentially measuring different samples of them (photon vs. π^0), we expect to obtain different inclusive photon v_2 values. At the same p_T bin, the ratio of direct photon over decay photon background is also different for these two algorithms. Using 4 towers boosts the decay photon spectra to higher p_T due to the more significant photon merging effect, and therefore results in a smaller signal-to-background ratio for direct photons. The amount of contamination also differs in two algorithms. In the π^0 analysis we have demonstrated that background from charged particles can be significant. The algorithm of using 4 towers is exposed to much more background so it has worse photon energy and position resolution. In this sense, the single tower algorithm is more superior and should give more reliable results. Nonetheless, we will carry on with two algorithms and take their difference as systematic uncertainty.

5.2.2 Decay photon v_2 from π^0 embedding

Although we are unable to distinguish between direct photons and decay photons particle by particle in real data analysis, the decay photon v_2 is still measurable. In principle, it is determined by the π^0 spectra and v_2, as well as its decay mechanism. Using the measured π^0 spectra and v_2 as input, we can perform simulation of π^0 decay and measure v_2 of decay photons. As discussed in the last section, the measured decay photon v_2 also largely depends on the detector response. In addition, background particles from the same event will also affect purity of the reconstructed photon sample, as well as their energy and position resolution. As a result, we use the π^0 embedding data to take into account all these effects.

The embedding data used here is the same as the one used in the π^0 analysis. Here only the MB triggered events in the embedding sample are used, which is about 22.5×10^3 events. Similar to the π^0 spectrum analysis, weighting factors are applied to the input π^0 spectra so that they mimic the PHENIX π^0 spectra [16]. Using the PHENIX π^0 spectra is due to the lack of precise π^0 spectra results in Au+Au collisions from STAR at the time this analysis was performed. More details about the weighting can be found in Sec 3.2.1.

Again, due to the lack of π^0 v_2 measurement in STAR, we use the v_2 of $\pi^{\pm}$ measured by the FTPC method in 200 GeV Au+Au collisions as input. Using the same v_2 measuring method as inclusive photons can help to partially cancel the v_2 systematic uncertainties, such as non-flow effect, when we subtract the decay photon v_2 from the inclusive photon v_2. The calculation of $\pi^{\pm}$ v_2 is similar to the inclusive photon v_2. Quality cuts in the TPC column of Table 5.1 except the p_T cut are applied to select good TPC charged tracks. An additional PID cut of N_σ is applied to select $\pi^{\pm}$ tracks. At p_T <2 GeV/c, we require that $-3 < N_{\sigma\pi} < 3$ and the N_σ of other particle types (proton, anti-proton, $K^{\pm}$, Deuteron, anti-Deuteron, and $e^{\pm}$) should be $N_\sigma < -3$ or $N_\sigma > 3$. At p_T >2 GeV/c, the PID cut is changed to $0 < N_\sigma < 3$ only, due to the separation of dE/dx bands at the relativistic rise. The $\pi^{\pm}$ v_2 in different centrality bins are shown in Figure 5.7. The fitting results of the $v_2(p_T)$ are also shown. At p_T <3 GeV/c a 4th order polynomial function is used, while at $p_T > 3$ GeV/c a linear function is used, requiring that it goes through the data point given

by the polynomial fit at 3 GeV/c. These fit results are used as the v_2 input of the embedding analysis.

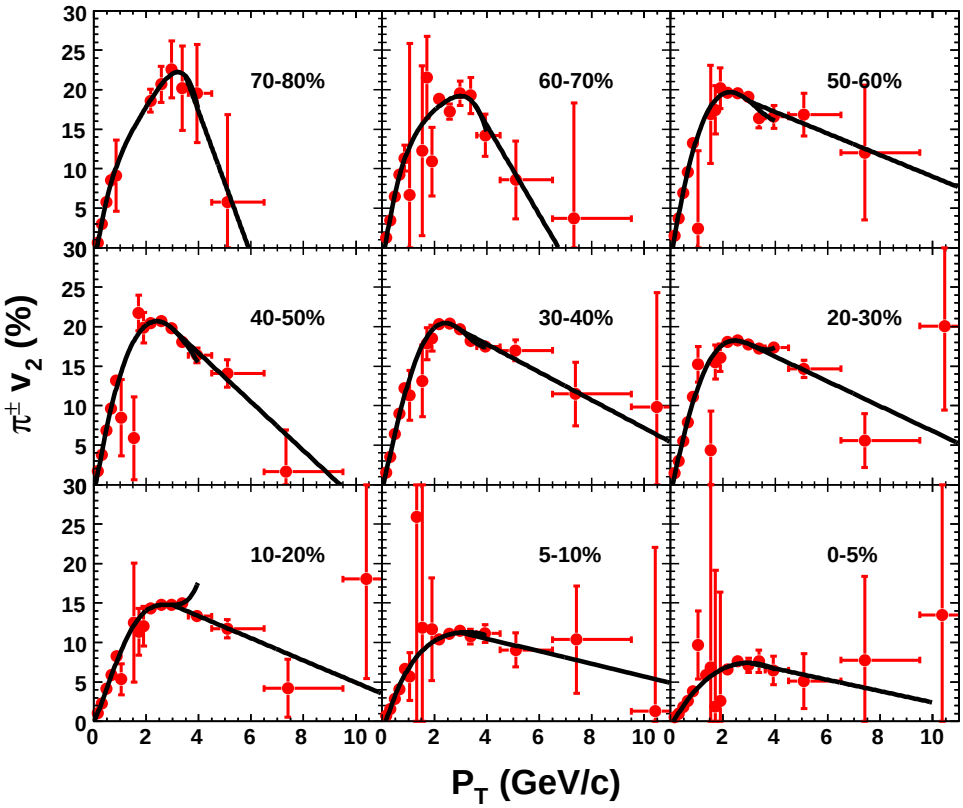

Figure 5.7: The $\pi^{\pm}$ v_2 measured by the FTPC method in different centralities in 200 GeV Au+Au collisions. The solid curves are fitting results.

The MC π^0's are generated with a flat azimuthal distribution. To simulate the π^0 v_2, we assume that the π^0 azimuthal distribution is purely sinusoidal $\frac{d^2N(p_T,\phi)}{dp_T d\phi} \propto [1 + 2v_2(p_T)\cos 2(\phi - \Psi_r)]$. If the azimuthal averaged π^0 spectrum is $\frac{dN(p_T)}{dp_T}$, at 0° and 90° with respect to the reaction plane, the spectrum becomes $\frac{dN(p_T)}{dp_T}[1 + 2v_2(p_T)]$ and $\frac{dN(p_T)}{dp_T}[1 - 2v_2(p_T)]$, respectively. Therefore, a weighting factor of $[1 \pm 2v_2(p_T)]$ is applied to the input π^0 spectrum to simulate the situations at 0° and 90° with respect to the reaction plane. The same photon PID cuts as the real data analysis are applied to reconstruct those MC decay photons. The spectra obtained from these two situations represent the decay photon spectra at 0° and 90° with respect to the

reaction plane. Their ratio $R(p_T)$ is related to the decay photon $v_2^{decay}(p_T)$ as:

$$R(p_T) \equiv \frac{dN(p_T, \phi = 0°)/dp_T}{dN(p_T, \phi = 90°)/dp_T} = \frac{1 + 2v_2^{decay}(p_T)}{1 - 2v_2^{decay}(p_T)}. \tag{5.22}$$

Solving this equation reveals the decay photon $v_2^{decay}(p_T)$.

To include the systematic uncertainty of the input v_2, the upper and lower limits of error bars of the $\pi^{\pm}$ $v_2 p_T$ data points are fitted, and their results are used as input in the embedding analysis too, with the outcomes of decay photon v_2^{up} and v_2^{low}. The differences of $[v_2^{up} - v_2^{decay}(p_T)]$ and $[v_2^{decay}(p_T) - v_2^{low}]$ are taken as the error bars of the decay photon v_2.

Besides the decay photon v_2, this procedure can also reveal the decay photon spectrum in the inclusive photon sample. To achieve it, a precise normalization factor should be applied to the input π^0 spectrum, so that not only the spectra shape, but also its absolute scale duplicates the true π^0 spectrum. Using the same photon PID cuts will produce the decay photon spectrum in the embedding data sample. It is then scaled by a normalization factor to match the data sample in real data analysis. Using the prescale factor discussed in Section 3.1.5, the decay photon spectrum in real HT data is given by

$$\frac{dN_{decay\_data}}{dp_T} = \frac{\sum_i F^i_{prescale\_MB} N^i_{MB}}{\sum_i F^i_{prescale\_HT} N^i_{HT}} \frac{N_{HT\_data}}{N_{MB\_embedding}} \frac{dN_{decay\_embedding}}{dp_T} \tag{5.23}$$

where N_{HT_data} and $N_{MB\_embedding}$ are numbers of HT events in real data and MB events in embedding. The prescale factor is used to transform the number of HT events in real data to the number of equivalent MB events.

Having the v_2 and spectrum of π^0 decay photons, its contribution can be subtracted from the inclusive photon v_2 using the additive relation of v_2:

$$v_2^{inclusive} N_{inclusive} = v_2^{b.g.\_subtracted}(N_{inclusive} - N_{b.g.}) + v_2^{b.g.} N_{b.g.}, \tag{5.24}$$

where "b.g." represents "background". Solving the equation gives the photon v_2 after background subtraction.

$$v_2^{b.g.\_subtracted} = \frac{v_2^{inclusive} N_{inclusive} - v_2^{b.g.} N_{b.g.}}{N_{inclusive} - N_{b.g.}}. \tag{5.25}$$

After removing all the background sources we will eventually obtain the direct photon v_2.

5.2.3 Other backgrounds

Decay photons from π^0's is the most important part, but not all of the background particles. Other background particles include photons from other meson decays, such as η, and ω mesons, and neutral hadrons which leave signals in the BEMC, mainly anti-neutrons [73]. A similar procedure as dealing with the π^0 can be applied to data embedded with the specific background particles, using its realistic spectrum and v_2 values.

To study the contributions from other meson decays, considering the lack of conclusive η and ω spectra and v_2 results in STAR, we can take advantage of the experimental observation of the so called m_T scaling law: the spectra of many hadrons scale with the π^0 spectrum when determined as a function of their transverse mass $m_T = \sqrt{m^2 + p_T^2}$ [82]. For the yields of η, it is given by

$$\frac{dN(m_T)}{dp_T}|_{\eta} = R_{\eta/\pi^0} \frac{dN(m_T)}{dp_T}|_{\pi^0}. \tag{5.26}$$

The ratio of R_{η/π^0} can be taken to be 0.40±0.04 (stat)±0.02 (syst) according to the measurement at RHIC [83]. For the contribution of ω, the ratio $R_{\omega/\pi^0} = 0.94$ and 0.85 for d+Au and p+p collisions [83], but there is no results for Au+Au collisions yet. The v_2 of η meson can be approximated using the v_2 of K meson, due to their similar mass and number of constituent quarks. Following the same procedure as the π^0 will give the v_2 contribution of photons from other meson decays.

The anti-neutrons interact with materials in the BEMC via the annihilation process, e.g. $\bar{n} + p \rightarrow 2\pi^+\pi^-\pi^0$, and create electromagnetic showers. Due to its large mass at rest (≈1 GeV), the measured spectrum can be significantly boosted to higher p_T and become a non-negligible contamination. The anti-neutrons yield can be approximated by the yield of anti-proton [71], after correcting for the feeddown from Λ and $\bar{\Lambda}$ ($\delta_\Lambda \approx 20\%$):

$$\bar{n} = (1 - \delta_\Lambda)\bar{p} + \delta_\Lambda \frac{\Gamma(\Lambda \rightarrow n\pi^0)}{\Gamma(\Lambda \rightarrow p\pi^-)}\bar{p} \tag{5.27}$$

where the last term estimates the feeddown according to the branching ratios $\Gamma(\Lambda \rightarrow n\pi^0)$=0.358 and $\Gamma(\Lambda \rightarrow p\pi^-)$=0.639 [73]. Similarly, the proton v_2 can be taken as

the anti-neutron v_2 as input. The same embedding data analysis will reveal the v_2 contribution of anti-neutrons. Using Equation 5.25 repeatedly can subtract their contributions and give the direct photon v_2.

What has been discussed is guidelines for studying the v_2 contributions from background particles. However, due to the lack of η, ω, and anti-neutron embedding data for this analysis, only results from π^0 embedding data are presented here.

5.3 Results

In this section results of inclusive photon and π^0 decay photon v_2 are shown and compared. The comparison indicates a small value of direct photon v_2.

5.3.1 Inclusive photon v_2

The inclusive photon v_2 as a function of p_T in 200 GeV Au+Au collisions is shown in Figure 5.8. The inclusive photon v_2 is measured up to 10 GeV/c using different photon identification algorithms and different v_2 measuring approaches. For the algorithm using BEMC clusters, two v_2 measurements give consistent results in the mid-centrality of 20-60%. In the more central collisions of 5-20%, two measurements give a consistent trend of v_2 as a function of p_T, but the values are more different than the 20-60% centrality bin. However, it should be emphasized that v_2 measurement in more central collisions suffer from more systematic uncertainty [79], due to their different sensitivity to non-flow effect, so we should expect larger variance between results from different methods.

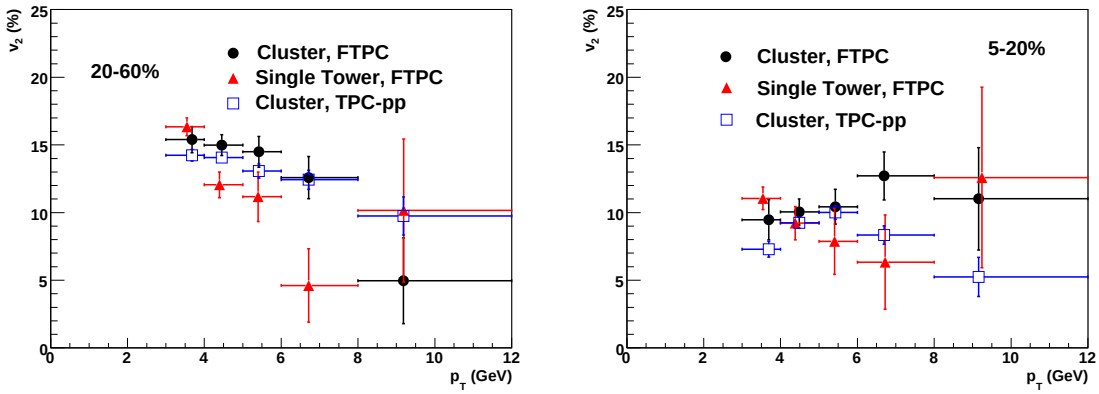

Figure 5.8: Inclusive photon v_2 as a function of p_T for centrality 20-60% and 5-20% in 200 GeV Au+Au collisions. Results from two photon reconstruction algorithms and two v_2 calculating methods are shown for comparison. Only statistical errors are shown.

The v_2 measurements from different photon identification algorithms using the FTPC method also give quite different results, with larger discrepancy in more central

collisions. It can be understood as the result of the STAR BEMC's response to high p_T π^0's and different background levels in the two algorithms, which is discussed in Section 5.2.1. Using the algorithm of clusters is more likely to reconstruct the whole π^0 instead of its decay photons. Therefore the different particle samples measured by the two methods yield different v_2 values.

5.3.2 Decay photon v_2

Figure 5.9 shows the decay photon v_2 as a function of p_T in different centrality bins using two photon identification algorithms. The input π^0 v_2 is also shown for comparison, which comes from fitting result of the $\pi^{\pm}$ v_2.

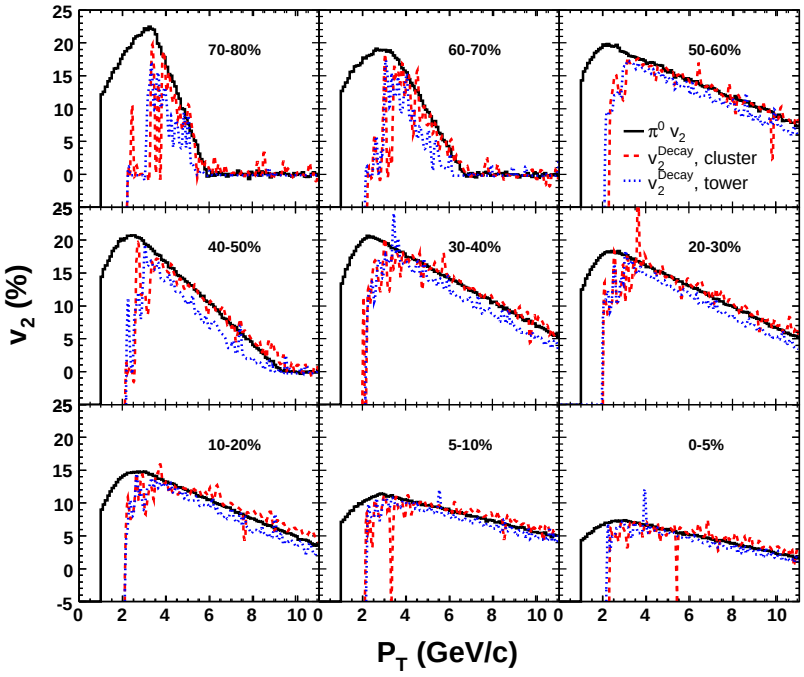

Figure 5.9: Decay photon v_2 as a function of p_T in different centrality bins using two photon identification algorithms, compared to the input π^0 v_2. Here only the v_2 values are shown without any error bars.

From these figures we can observe that both decay photon v_2 curves follow the

input π^0 v_2 closely, indicating that the decay photon v_2 largely inherits the v_2 of its parent. However, v_2 from the single tower algorithm is systematically smaller than the cluster algorithm. It is consistent with the STAR BEMC's response to high p_T π^0's. The particles reconstructed from cluster are likely to have higher p_T than the ones from single tower, therefore its v_2 curve is shifted towards higher p_T compared to the single tower algorithm. In addition, the v_2 from clusters are very close to the input π^0 v_2, which is consistent to the simulation result that the cluster algorithm very likely reconstructs the π^0 itself instead of decay photons. In the most central events, there is even some hint that the v_2 from clusters is higher than the input π^0 v_2. It is possibly due to the larger background from other particles which further enhance the reconstructed particle's energy.

After considering the error bars and re-binning the π^0 decay photon v_2 values, we show the results in Figure 5.10, comparing to the corresponding inclusive photon v_2. The inclusive photon and π^0 decay photon v_2 follow the same trend of v_2 decreasing with p_T. One exception is the central events from the cluster algorithm. However, as discussed in the last section, the cluster algorithm is likely to include more background which modifies the shape of $v_2(p_T)$, especially in more central events.

For most of the data points, more evident in the single tower algorithm, the inclusive photon v_2 is systematically smaller than the π^0 decay photon v_2. According to Equation 5.25, after background subtraction the $v_2^{b.g.\_subtracted} < v_2^{inclusive}$ if $v_2^{inclusive} < v_2^{b.g.}$, because $v_2^{b.g.\_subtracted}$ can be written as

$$v_2^{b.g.\_subtracted} = v_2^{inclusive} - (v_2^{b.g.} - v_2^{inclusive})\frac{N_{b.g.}}{N_{inclusive} - N_{b.g.}}. \tag{5.28}$$

In addition, other background particles, such as η decay photons and anti-neutrons, are likely to have larger v_2 than π^0 decay photons. As a result, current comparison in Figure 5.10 indicate that direct photons have a small value of v_2, especially considering the small fraction of direct photons. Although still far from conclusive, the current results are qualitatively consistent with theoretical calculations of direct photon v_2 [45, 46].

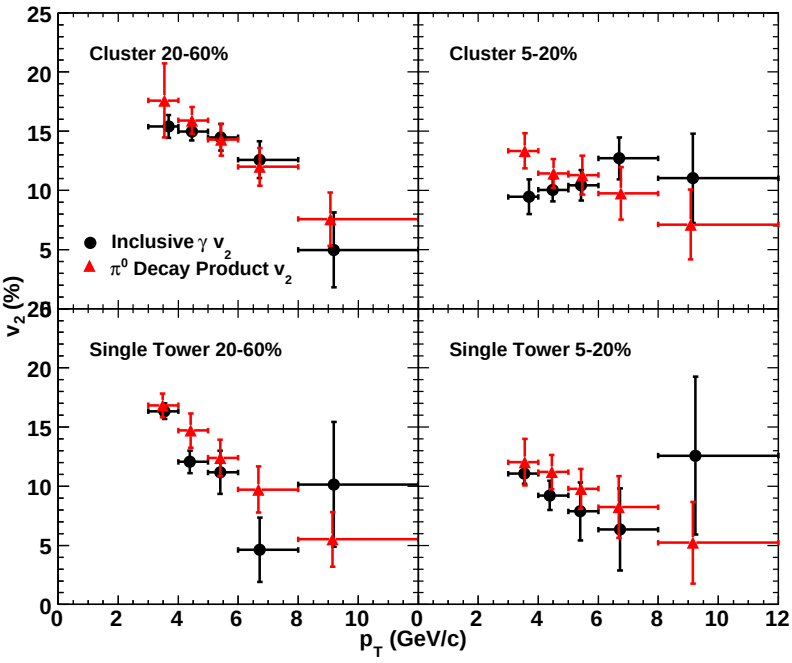

Figure 5.10: The π^0 decay photon v_2 as a function of p_T using both photon identification algorithms in centrality bins of 20-60% and 5-20%. The inclusive photon v_2 is shown for comparison. Only statistical errors are shown.

5.3.3 Decay photon spectrum

As discussed in Section 5.2.2, the decay photon spectrum in the reconstructed inclusive photon sample can also be obtained from the embedding data analysis. The π^0 decay photon spectra from two photon identification algorithms are shown in Figure 5.11 and 5.12, respectively. The inclusive photon spectra are also shown for comparison.

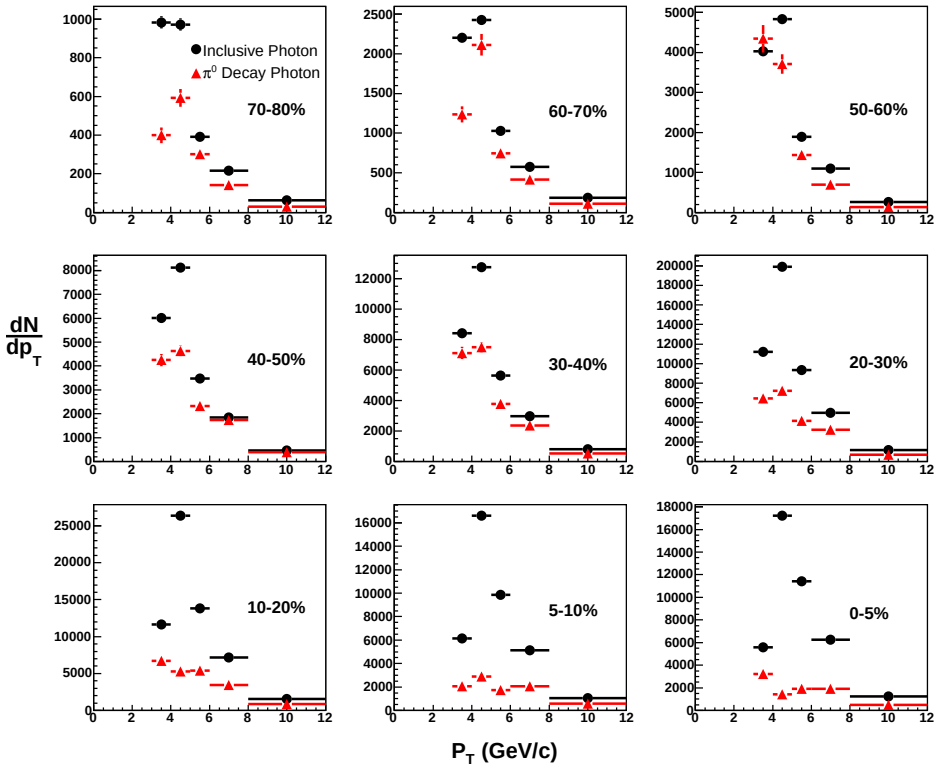

Figure 5.11: The π^0 decay photon spectra in different centralities compared to the inclusive photon spectra from the cluster algorithm.

We observe difference between the inclusive photon spectra and π^0 decay photon spectra, which should represent the contributions from direct photons and other background particles. However, the difference seems too large, especially in the more central events. It contradicts the expectation that π^0 decay photons dominate the inclusive photon sample. This issue is still not fully understood yet, and it needs

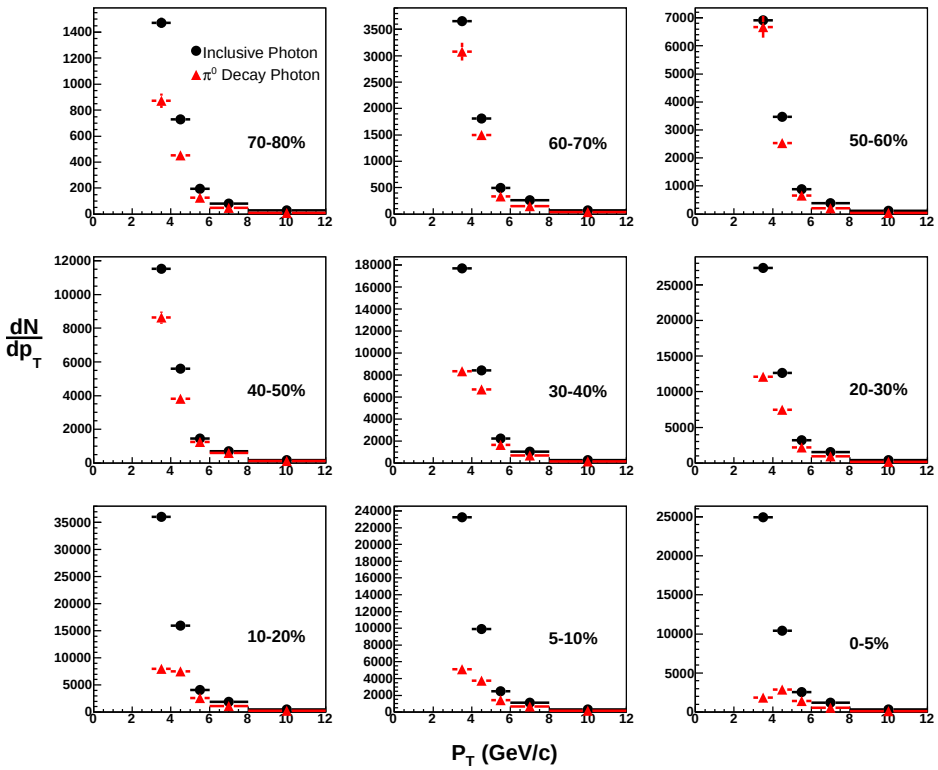

Figure 5.12: The π^0 decay photon spectra in different centralities compared to the inclusive photon spectra from the single tower algorithm.

further investigations.

5.3.4 Summary

As a summary of this chapter, the first STAR results for high p_T inclusive photons elliptic flow in 200 GeV Au+Au collisions are shown. The inclusive photon v_2 is calculated using event planes from the FTPC and the main TPC. The non-flow contribution is suppressed by the pseudo-rapidity gap between the FTPC and TPC, or is subtracted using particle correlations in p+p collisions.

As the major background in the inclusive photon sample, the π^0 decay photon v_2 is calculated via the π^0 embedding data, using the earlier measured π spectrum and v_2 results. The comparison between decay photon and inclusive photon v_2 indicates that the direct photons have small values of v_2, consistent with theoretical predictions. However, to further subtract the background contributions requires better understanding of the spectra and v_2 of different background particles, as well as more embedding simulations of the background particles.

The direct photon v_2 analysis is undoubtedly a challenging task. It requires a larger amount of statistics, considering the current statistical errors. It also demands the knowledge of many background particles. As shown in Chapter 3, measurement of these particles is being effectively performed in STAR. Future upgrade of full azimuthal STAR BEMC coverage and DAQ upgrade will also significantly enhance our ability for data collection and enable us to trigger on higher p_T photons. All of these will help to perform a more precise and comprehensive measurement of direct photon v_2.

Chapter 6

Muon Telescope Detector

6.1 MTD simulation

In this section simulation results for the Muon Telescope Detector (MTD) performance will be presented, including the efficiency of identifying muons and rejecting hadron backgrounds, and the possibility of implementing a muon trigger for heavy ion collisions.

6.1.1 MTD geometry

The idea of the MTD is to utilize the whole STAR detector system as hadron absorber to suppress the hadron background. Without participating in strong interactions, muons have very small cross section for interactions and thus can easily escape from the detectors. Unlike traditional muon detectors which rely heavily on tracking stations, the MTD uses a Multi-gap Resistive Plate Chamber with large modules, long strips, and double-ended readout (Long-MRPC) as core units, which have good timing (<100 ps) but relatively mediocre spatial (≈1 cm) resolution. Similar technology with small pads has been used for the Time-of-Flight detector (TOF) in STAR [57].

The geometry of the MTD used in our simulation is shown in Figure 6.1. The MTD layers are placed outside the STAR magnet and cover the 30 magnet return bars at radius $r = 371$ cm, leaving the gaps between the return bars open. The dimension

of each MTD layer is $715 \times 54 \times 2$ cm^3, covering pseudo-rapidity of $|\eta| < 0.8$ and 73.6% of the azimuthal angle. The material of this detector would be thin scintillator plastic.

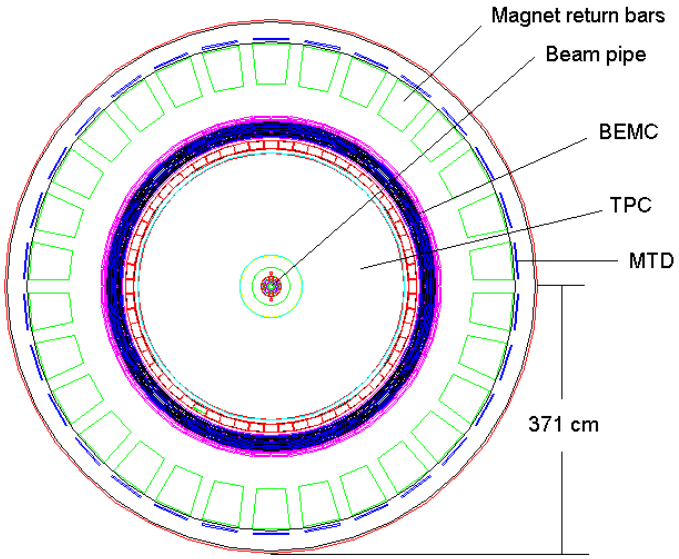

Figure 6.1: The schematic view of the MTD geometry. The MTD is shown as a blue layer outside the magnet return bars.

To demonstrate the feasibility of the MTD, Figure 6.2 shows its response to 5 MC muons and pions generated with $2 < p_T < 5$ GeV/c. The simulation confirms our expectation, in which muons can easily penetrate through the materials and hit the MTD, while pions are mostly stopped by the BEMC or the magnet return bars.

6.1.2 Muon identification and hadron rejection

In this simulation we use the STAR year 2003 geometry. Due to the fact that in 2003 the STAR BEMC was only installed for $0 < \eta < 1$, we generate MC particles with $0 < \eta < 0.8$ only. Here muons and hadrons ($\pi^{\pm}$, $K^{\pm}$, p, and $\bar{p}$) are generated with a flat p_T and ϕ distributions in $0 < p_T < 20$ GeV/c and $0 < \phi < 2\pi$, respectively. For simplicity, only a single particle is generated in each event. The MC particles are propagated through GEANT and reconstructed using a number of quality cuts,

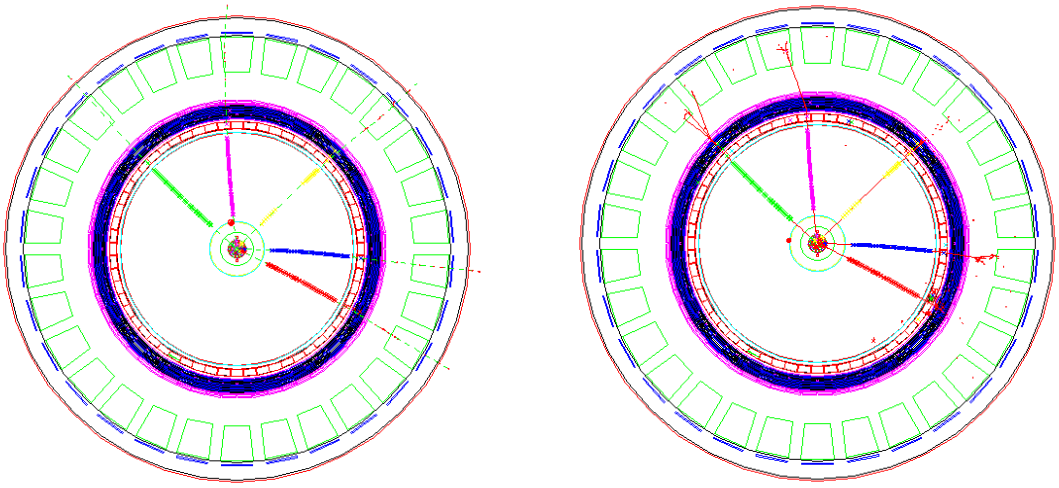

Figure 6.2: Examples of 5 MC muons (left) and pions (right) generated with $2 < p_T < 5$ GeV/c and propagated through the STAR detectors in GEANT.

which will be discussed below. Finally the detection efficiencies of muons and other hadrons are compared to evaluate the performance of the MTD.

It is interesting to see how the MTD performs without applying any cuts. Any track which leaves any hit on the MTD is counted as a reconstructed track. This simple requirement gives the efficiency shown in Figure 6.3. For muons, the efficiency saturates at 2 GeV/c. Considering the MTD coverage of 73.6%, about 90% of the muons are able to arrive at the MTD when $p_T > 2$ GeV/c. For pions, the efficiency increases roughly linearly with p_T, and reaches 30% at 15 GeV/c (40% considering the MTD coverage), indicating that higher energy tracks are more likely to survive. Although the efficiency for muons is significantly higher than pions, it is still far from enough due to the overwhelming pion background ($\frac{N_\pi}{N_\mu} \approx 500$) in heavy-ion collisions. Therefore, cuts on the MTD should be refined to distinguish those which can be associated with the original MC tracks.

Firstly, MTD hits close to the layer edge should be rejected. Although the MTD is completely behind the magnet return bars, hadrons can still escape from the gaps between two return bars and hit the MTD boundary after scattering or showering. Figure 6.4 shows the MTD hit distribution on one MTD layer with respect to the layer center in the azimuthal direction in pion simulation. Near layer center hits are

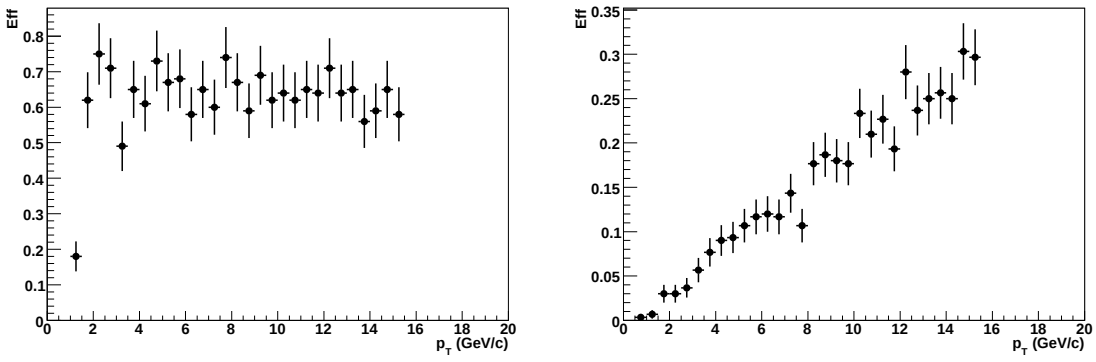

Figure 6.3: Efficiency of reconstructing muons (left) and pions (right) at the MTD as a function of p_T requiring only one hit on the MTD.

from penetrating pions and are uniformly distributed. Approaching the boundary we start to observe tracks escaping through the gaps and the distribution rises. To remove this background only hits within 22 cm from the layer center are accepted, which reduces the effective azimuthal acceptance of the MTD to 56.6%.

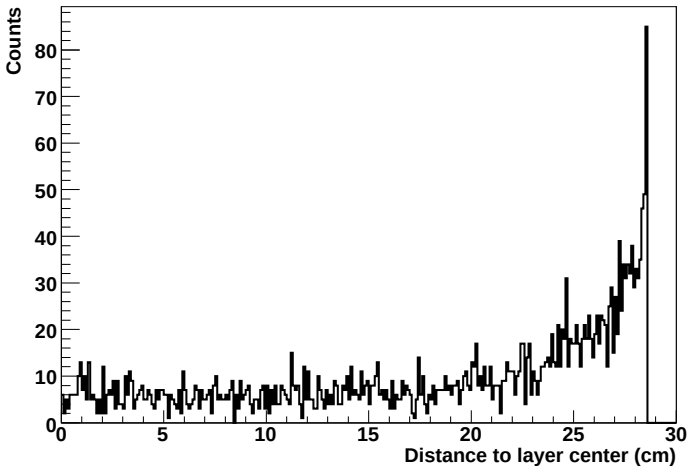

Figure 6.4: MTD hit distribution with respect to the layer center in the azimuthal direction in pion simulations.

Secondly, MTD hits deviating from the MC tracks are rejected. From Figure 6.2 we can see that a hadron experiences much more scattering and is more likely

to generate a hadronic shower. Therefore, its trajectory usually deviates from its original direction and it creates a random hit on the MTD. We assume that the trajectory of a charged track without any interaction in the detector is an ideal helix, with its direction and velocity determined by its parameters at the primary vertex. MC tracks are projected onto the MTD based on this assumption, and their distance of closest approach (DCA) to the detected MTD hit are calculated. The DCA vs. p_T 2-D distributions for muons and pions are shown in Figure 6.5. For muons, the detected MTD hits are generally close to the ones predicted by a helix, but with more scattering for low p_T muons. While for pions, the MTD hits are randomly distributed at all p_T ranges. The DCA distributions at different p_T slices for muons are fit using a gaussian function, and the most probable DCAs and widths (σ) are obtained. Only MTD hits with DCA within 1.5σ from the most probable DCA at the corresponding p_T are accepted. The most probable DCA and width as a function of p_T are shown in Figure 6.6. Their fitting curves are used to apply this cut.

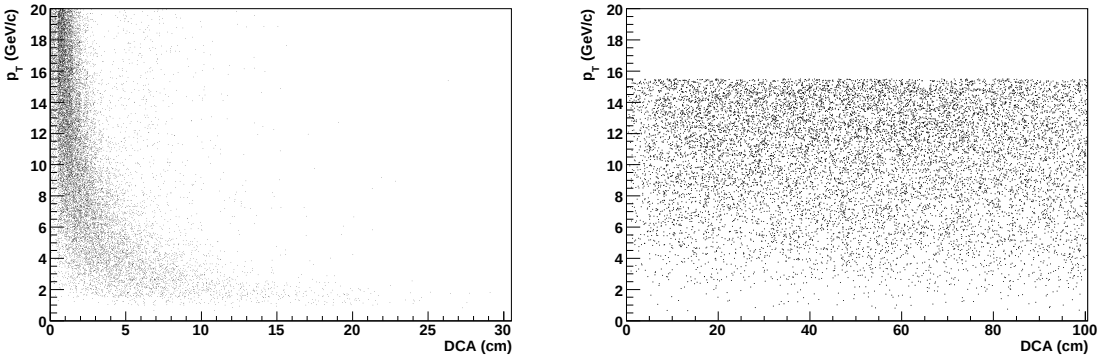

Figure 6.5: The DCA vs. MC track p_T distributions for muons (left) and pions (right).

Thirdly, the TOF of MTD hits are compared to the TOF of MC tracks assuming that they are ideal helices, and MTD hits with large TOF deviations are rejected. TOF of MC tracks are calculated as the length of the helix from primary vertex to the MTD over the speed of light. Similar to the DCA cut, hadrons experience more scattering and showering and thus have longer paths and TOF to the MTD. Figure 6.7 shows the TOF difference $\Delta TOF = TOF_{track} - TOF_{hit}$ distributions for muons and pions. Muons have much narrower distribution than pions, and we require

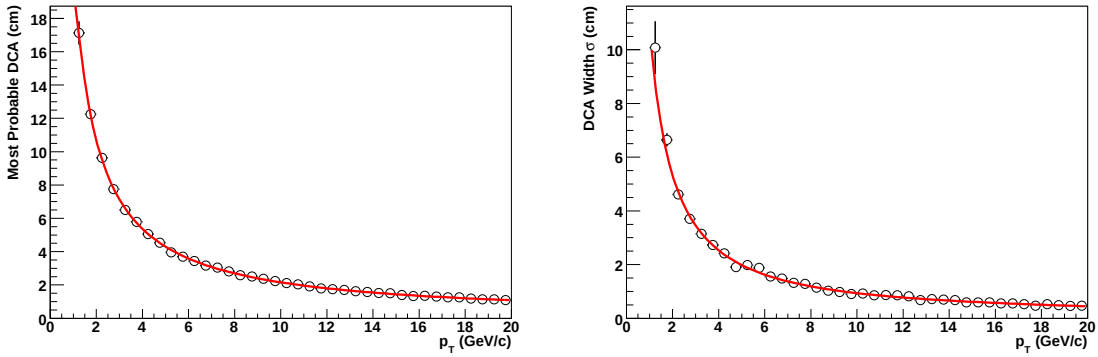

Figure 6.6: The most probable DCA and the width of the DCA distribution for muons as a function of p_T

$-0.2 < \Delta TOF < 0.1$ ns for a muon candidate.

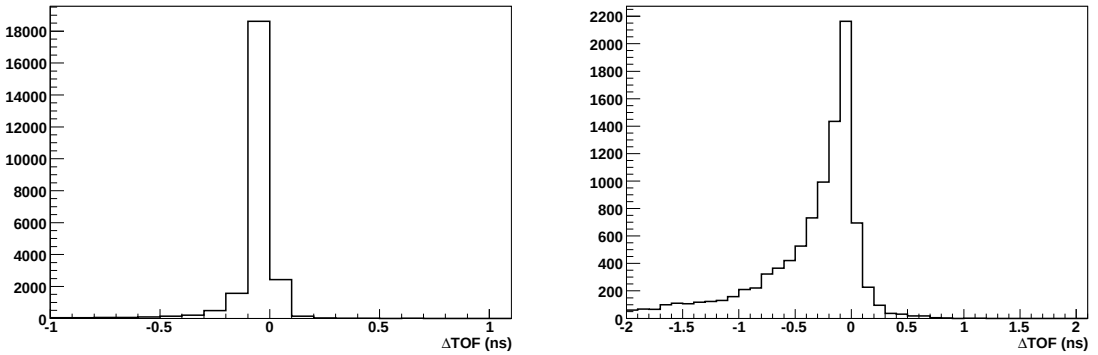

Figure 6.7: TOF difference between MC tracks and the MTD hits for muons (left) and pions (right).

Last, but not the least, if measuring energy loss of charged tracks on the MTD is possible, it can be used to distinguish muons from hadrons. Figure 6.8 shows the energy loss of muons and pions in the MTD, which peak at different values. As a result, an energy loss cut of $3 < E_{loss} < 6$ MeV is applied to select muons in our simulation.

After applying all cuts the detection efficiencies for muons and hadrons are shown in Figure 6.9. For muons, the efficiency saturates at 40-45% above 2 GeV/c. Considering the MTD coverage of 56.6%, about 80% of muons within the MTD coverage

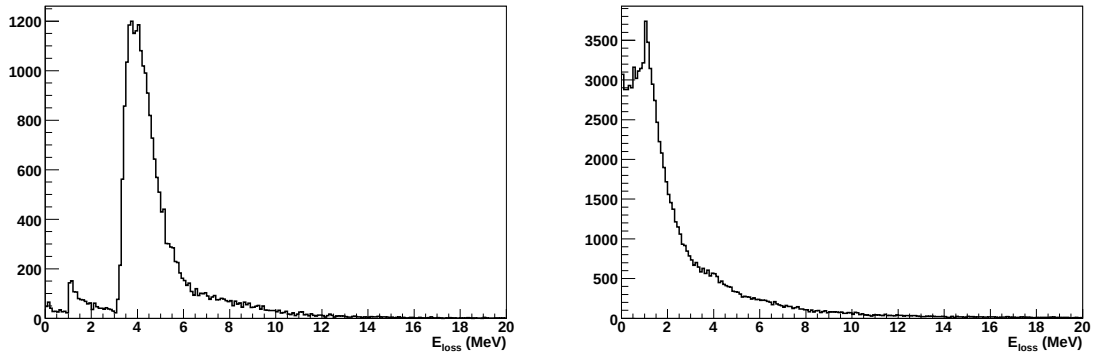

Figure 6.8: Energy loss of muons (left) and pions (right) in the MTD.

can be reconstructed. For hadrons of pions and kaons, the efficiency reaches 1-1.5% at intermediate to high p_T. The efficiency for protons is lower than pions and kaons. Therefore, the MTD itself is able to provide a factor of 50 in hadron suppression.

Intermediate p_T muons ($2 < p_T < 5$ GeV/c) are most interesting at RHIC because muons are most populous at this p_T range and they involve a lot of important physics topics, such as J/Ψ, Υ, and Drell-Yan di-muon production. As a result, we increase the statistics of our simulation in this p_T range and have a closer look at the MTD's hadron rejection ability. The result is shown in Figure 6.10. The detection efficiency is consistent with Figure 6.9. It indicates that a significant fraction of pion hits on the MTD are from secondary decay muons, which will become a major background for primary muons. Whether we can remove the decay muon background using additional cuts, such as the global DCA, requires more in-depth simulations and unfortunately, can not be addressed here.

The MTD itself is able to reject hadron background by a factor of 50. In STAR, kaons and protons can be removed by the TOF and dE/dx in the TPC. For central heavy-ion collisions at intermediate p_T, pions are about 1/3 of all hadrons. Therefore, depending on the possibility of identifying decay muons from pions and kaons, which is roughly 1/2 of background from pions, we expect a rejection factor of 150-300 for hadron backgrounds.

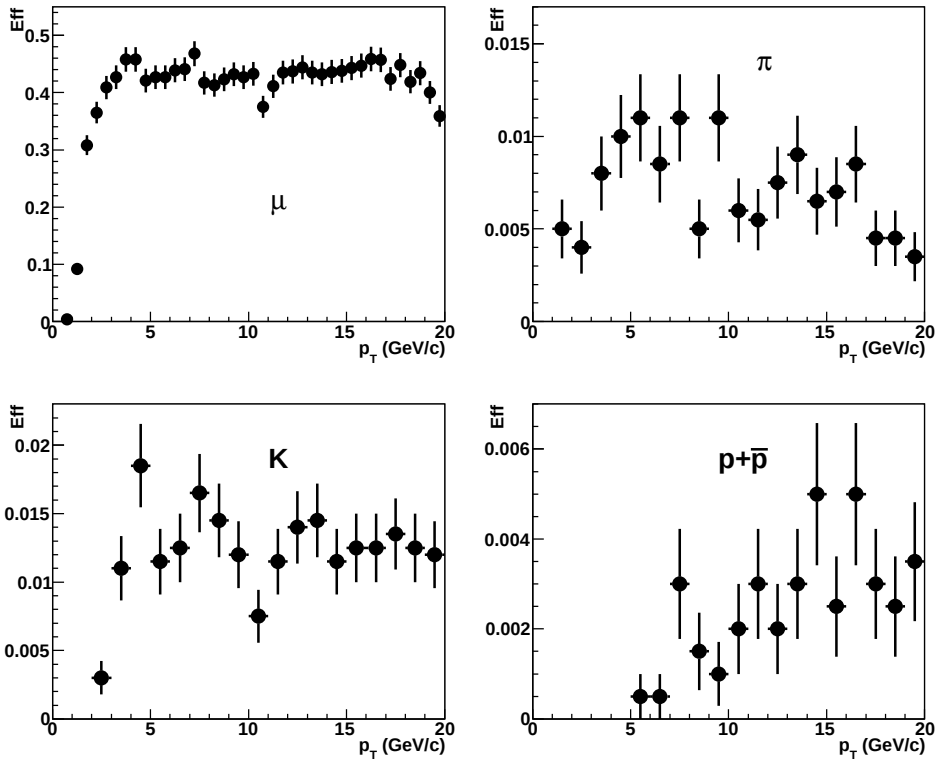

Figure 6.9: The detection efficiencies for muons and hadrons in the MTD.

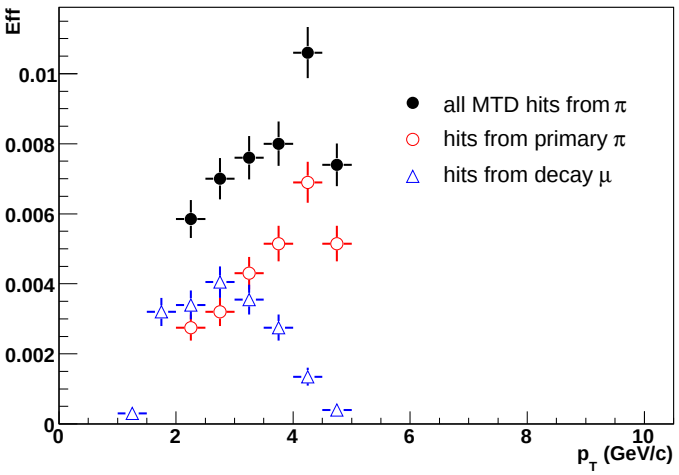

Figure 6.10: The detection efficiencies for pions in the MTD at $2 < p_T < 5$ GeV/c. MTD hits from primary pions and decay muons are also presented.

6.1.3 Muon and high-p_T hadron trigger

Being able to distinguish muons from hadrons offline is good, but being able to select and trigger on muons online will be even better. Another prospect of the MTD is to serve as a muon trigger detector. In principle it is promising because, as discussed earlier, muons do not participate in strong interaction and have much higher chance to arrive at the MTD. Therefore, requiring hits on the MTD should help select muon rich events. However, one caveat is that the large multiplicity of central Au+Au events will counteract the low probability of hadrons hitting the MTD, and thus void the muon trigger.

As a result, 100 central HIJING events [62] with impact parameter $b < 3$ fm are generated and propagated in GEANT to test the performance of the MTD. Without Charm and Bottom contribution, all tracks in HIJING events are hadron backgrounds for us. Figure 6.11 shows an example of a central HIJING event in STAR, as well as the p_T distribution of charged tracks in 100 HIJING events. The first impression of the figure is very positive. Most of the charged tracks are stopped by the BEMC or the return bars, and the survivors mostly escape from the gaps between return bars and do not hit the MTD.

To further test the hadron rejection ability of the MTD under high-multiplicity conditions, we apply the same cuts used to identify muons in the single particle simulation. Out of 840 charged tracks with $p_T > 2$ GeV/c, only 3 tracks survive. Considering the MTD coverage the hadron rejecting factor is about 100, which is consistent with the single particle simulation.

The difference between online muon trigger and offline muon reconstruction is that tracking is not available for triggering. So only the TOF and energy loss information may be used. In addition, due to the lack of tracking, the TOF of a track can not be calculated. Instead, a straight line from the primary vertex to the MTD hit is used. Different combinations of TOF and energy loss cuts have been tried and the performance of the muon trigger is shown in Table 6.1. Here two different TOF requirements are applied, one conservative cut requires that $TOF < 20$ ns and the other more aggressive one requires that $-400 < \Delta TOF < 100$ ps, where $\Delta TOF = TOF_{track} - TOF_{hit}$ as before. We can see that without any cut every

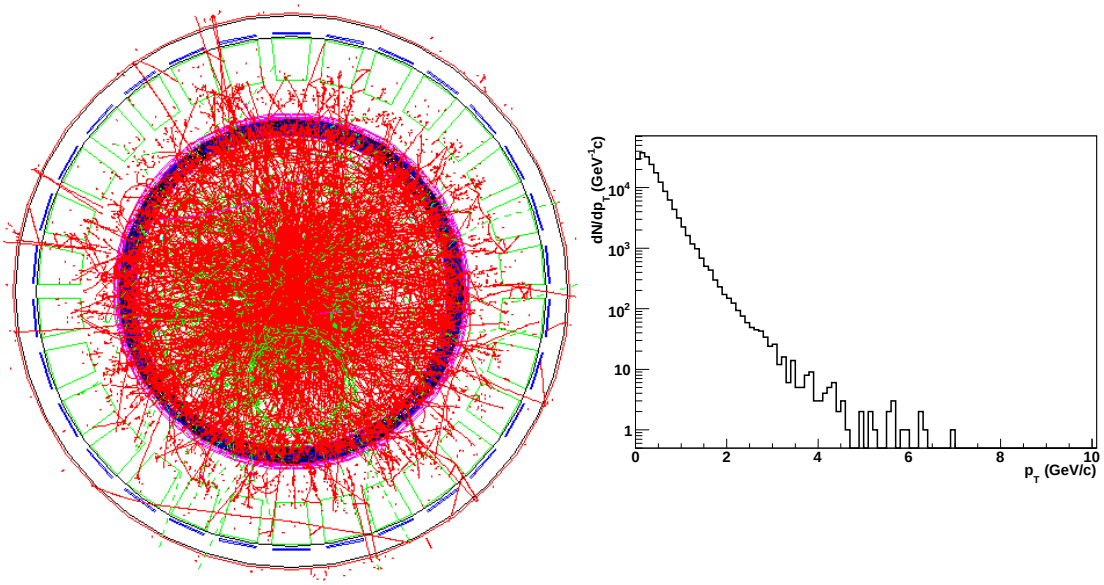

Figure 6.11: An example of a central HIJING event propagated in GEANT (left) in STAR and the p_T distribution of the charged tracks in 100 HIJING events (right).

event leaves a large number of hits on the MTD, but most of them are from multiple scattering and showering and can be rejected using the TOF cut. If we would like to trigger on di-muon events and require at least two qualifying hits on the MTD, 18 out of 100 events pass the conservative TOF cut while only 2 pass the tighter cut. This suggests that with a conservative timing resolution we can reject central Au+Au background events by a factor of 5, and the rejection factor will be up to 50 if we can reach a timing resolution of less than 100 ps. This result indicates that the key for the muon trigger is the timing resolution of the MTD. In the next section we will demonstrate that the technology of Long-MRPC is an ideal solution for the main unit of the MTD.

On the other hand, the MTD may be used as a high p_T hadron trigger as well, since high p_T hadrons have smaller cross section of interaction and are more likely to hit the MTD. Only requiring that $TOF < 20$ ns, the detection efficiency for pions is shown in Figure 6.12. This result is obtained from single particle simulation. It is clearly seen that the detection efficiency is linear with p_T and reaches 20% at p_T=15 GeV/c. The detection efficiencies for kaons and protons are similar to pions.

Cuts	N_{hits}/event
No cut	70
TOF <20 ns	1.6
$3 < E_{loss} < 6$ MeV	7.6
$TOF < 20$ ns && $3 < E_{loss} < 6$ MeV	0.72
$-400 < \Delta TOF < 100$ ps	0.23

Table 6.1: The number of MTD hits per central Au+Au HIJING event when using different online muon trigger requirements.

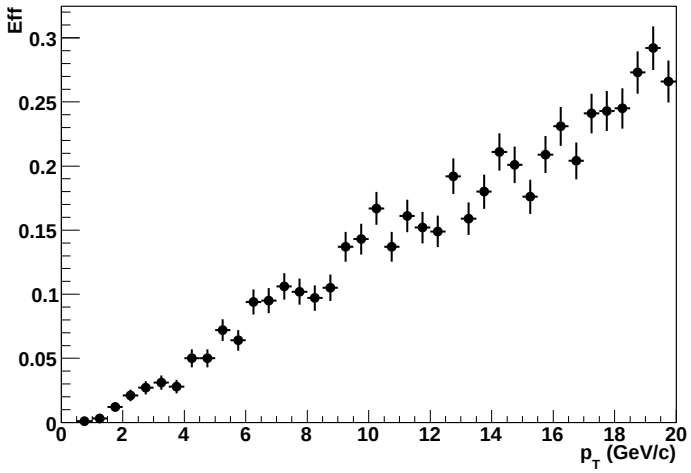

Figure 6.12: The detection efficiency for pions in the MTD as a function of p_T after requiring $TOF < 20$ ns.

6.1.4 Upsilon Simulation

One potential physics topic of the MTD is the Υ production. A conventional way to reconstruct Υ in STAR is via the di-electron channel using two electrons reconstructed by the TPC and BEMC. The main problem of this approach is that electrons lose energy through bremsstrahlung, so the reconstructed electron tracks have bad momentum resolution and we are unable to separate different states of Υ. Muons do not suffer bremsstrahlung energy loss so the di-muon channel will be preferable.

A toy model [84] assuming a nominal TPC primary track momentum resolution of $\delta p/p = 0.0087 + 0.0045p$ [85], and a ratio of 1S:2S:3S=9:1.8:1 for 3 states of Υ from CDF [86], gives the di-muon invariant mass distribution shown in Figure 6.13. We can see that using two muon tracks with momenta given by the TPC is able to separate different states of Υ.

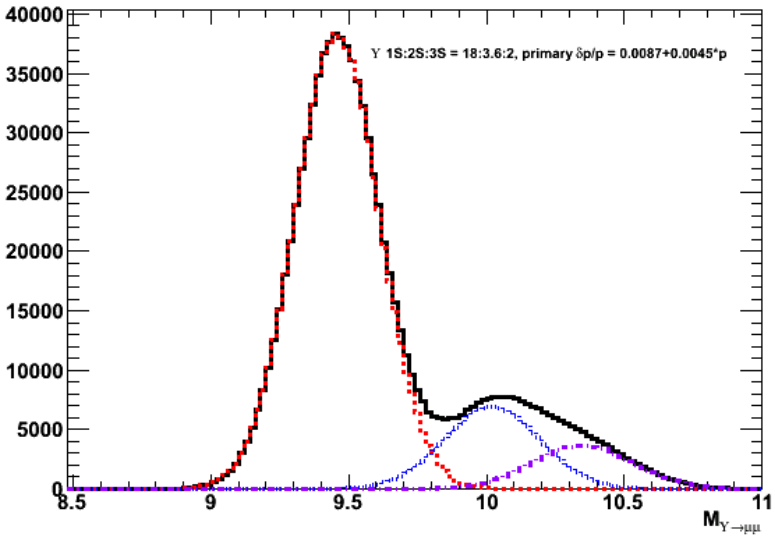

Figure 6.13: Di-muon invariant mass distribution assuming a nominal TPC primary track momentum resolution of $\delta p/p = 0.0087 + 0.0045p$, and a ratio of 1S:2S:3S=9:1.8:1 for 3 states of Υ from CDF.

A more realistic simulation is performed to confirm the toy model result. One MC Υ of a specific state is embedded into each of 10^4 central HIJING events, with flat p_T distribution of $0 < p_T < 20$ GeV/c. So 3×10^4 events in total are analyzed for three states. The reconstructed primary muon tracks in the TPC are used to calculate the

invariant mass. Here we assume that all muon tracks fire the MTD trigger. This assumption does not affect the result but only helps increase the efficiency, because what really matters is the TPC momentum resolution. The numbers of particles from the Υ(2S) and Υ(3S) are scaled down according to the ratio used in the toy model. The results of the simulation are shown in Figure 6.14. The invariant mass peaks are broader at higher p_T, because the TPC momentum resolution becomes worse there. At p_T bins of $0 < p_T < 5$ GeV/c and $5 < p_T < 10$ GeV/c, the contributions from 2S+3S can be clearly separated from 1S, while at higher p_T it becomes difficult. If the individual invariant mass peaks of different states at $0 < p_T < 5$ GeV/c are fit using a gaussian function and re-drawn using the fitting results, we obtain the lower right figure, which looks very similar to the toy model result. The simulation confirms the result obtained from the toy model, and indicates that different states of Υ can be separated via the di-muon channel using muon tracks reconstructed by the TPC and MTD.

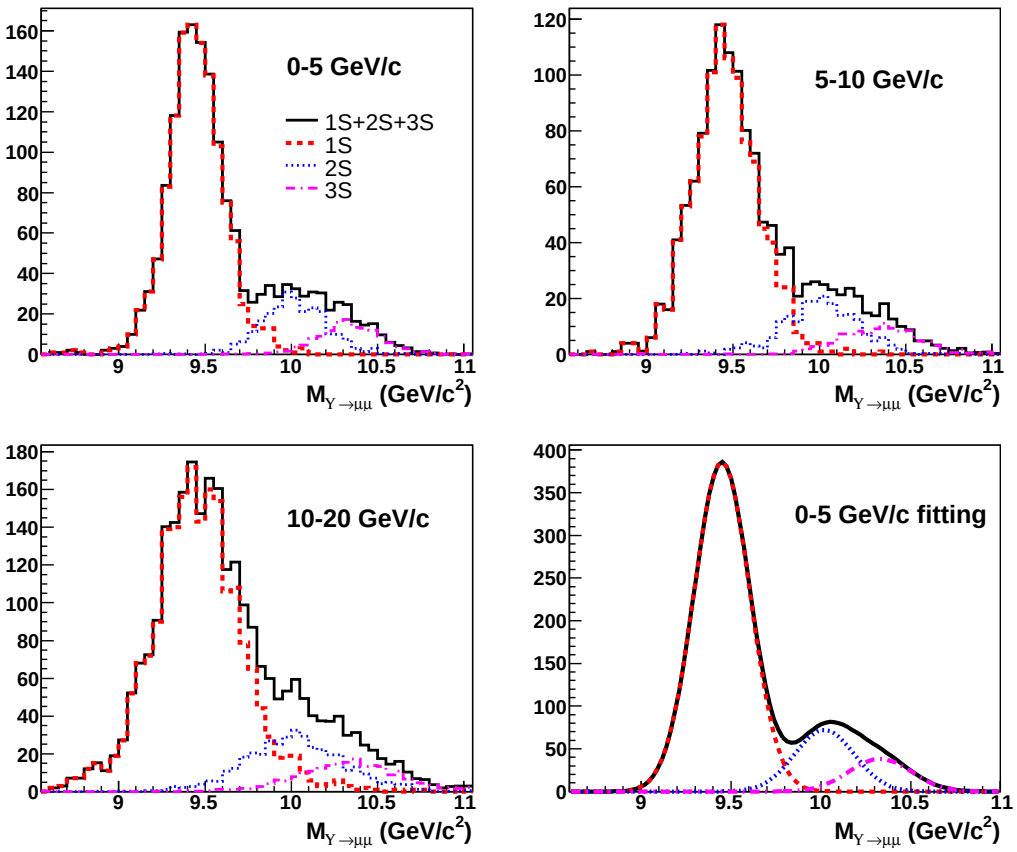

Figure 6.14: Di-muon invariant mass distributions at different p_T ranges from Υ simulation. The lower right figure shows the Υ invariant mass peaks using the fitting results (gaussian peak positions and widths) at $0 < p_T < 5$ GeV/c, and the ratio of states used in the toy model.

6.2 Long-MRPC beam test at FNAL

In this section the Long-MRPC technology is briefly discussed. The performance of Long-MRPC prototypes was tested in a three-week beam test at Fermi National Accelerator Laboratory (FNAL), and the results including timing and spatial resolutions are presented.

6.2.1 Long-MRPC

Figure 6.15 shows the schematic layout of a Long-MRPC module [87, 88]. Each Long-MRPC module consists of two stacks of resistive glass plates with ten uniform gas gaps with gap widths of 250 μm. High voltage is applied to electrodes on the outer surfaces of the outer plates of each stack. A charged particle traversing a module generates avalanches in the gas gaps which are read out by six copper pickup strips with strip dimensions of 870×25 mm^2. The Long-MRPC modules operate at 12.6 kV with a working gas of mixture of 95% $C_2H_2F_4$ and 5% iso-butane at 1 atmosphere.

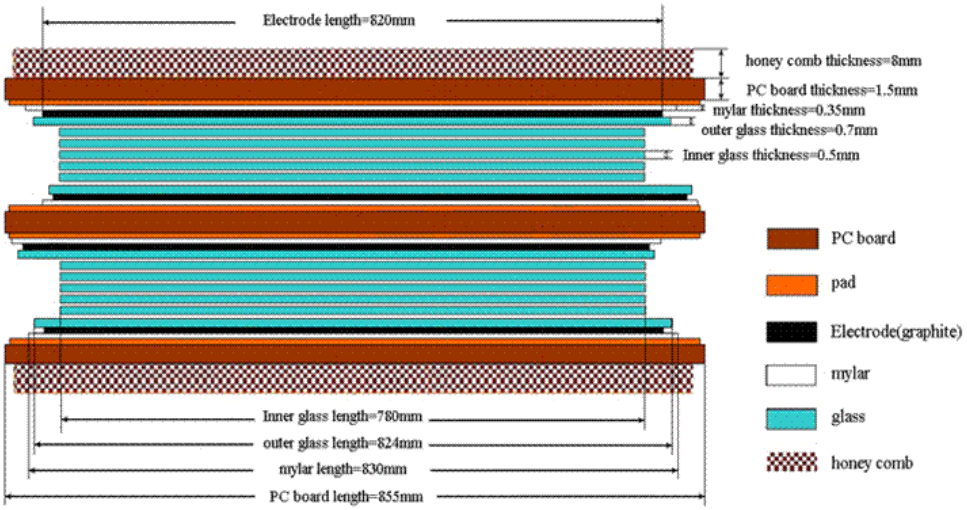

Figure 6.15: Schematic layout of a Long-MRPC module.

The MRPC technology has been successfully implemented in the TOF detectors in STAR [57]. It has the advantage of good timing resolution of less than 100 ps, high efficiency of greater than 95%, high granularity and low cost. Unlike the smaller

MRPC	length	width	height	HV	gas	strip
MTD	850 mm	255 mm	12 ×0.25 mm	±6.3 ∼ 7.3 kV	95% Freon 5% Iso-butane	6
TOF	210 mm	94 mm	6 ×0.22 mm	±7.0 kV		

Table 6.2: The comparison between MRPC modules used in the TOF and MTD.

MRPC modules used in the TOF, the MTD takes advantage of a long strip, two end read-out MRPC module with double the number of gas gaps. A comparison of MRPCs used in the TOF and MTD is shown in Table 6.2. The larger granularity used in the MTD is due to the fact that the MTD operates in a much lower multiplicity environment than the TOF. Using the Long-MRPC significantly reduces the number of read-out channels and therefore simplifies the electronics and lowers the cost.

6.2.2 Beam test setup

The two Long-MRPC modules being tested in the beam test were produced by USTC and Tsinghua University in China. Before the beam test, the USTC module had been tested at USTC and BNL using cosmic rays. The results indicate that the efficiency reaches 95% at the working high voltage, the timing resolution can be as good as 60 ps, the signal propagating velocity is about 60 ps/cm, and therefore the spatial resolution is about 1 cm. Results of the cosmic ray and the beam test at FNAL have been published at Ref. [87].

The beam test named T963 was performed at FNAL on May 2-15, 2007 by the MTD group, which consists of 22 people from 8 institutes or universities. The spokesperson of the T963 experiment is Dr. Zhangbu Xu from BNL. The experiment setup of the beam test is shown in Figure 6.16. A controllable beam comes from left to right and traverses all detectors for six seconds every minute. The beam energy, dimension, and intensity can be changed by the main control room. Most of the time, a beam with energy of 32 GeV was used. Here C1 and C2 represent two Cherenkov detectors used for particle identification. The coincidence of TOF1 and TOF2 scintillators is used as an event trigger, by indicating that a particle traverses all detectors along the beam line. The TOF3 consists of scintillators and PMTs from

BNL which provide the starting time. Four wire chambers MWPC1 to MWPC4 provided by FNAL, and three layers of GEM chambers from MIT tested along with the Long-MRPC modules are able to accurately measure the incident particle position. The two Long-MRPC modules are placed before the GEM chambers, with the Tsinghua module in the front. Two modules are secured on a platform which can move horizontally and vertically to change the beam incident position on the modules. The modules can also be adjusted to change the beam incident angle. An independent gas system is set up to supply Iso-butane and SF6 continuously, and the gas composition can be adjusted. A 1.5 m thick ion absorber can be moved in and out. When it is in, it blocks the beam line and absorbs most of the hadrons and electrons, leaving only highly penetrating particles such as muons.

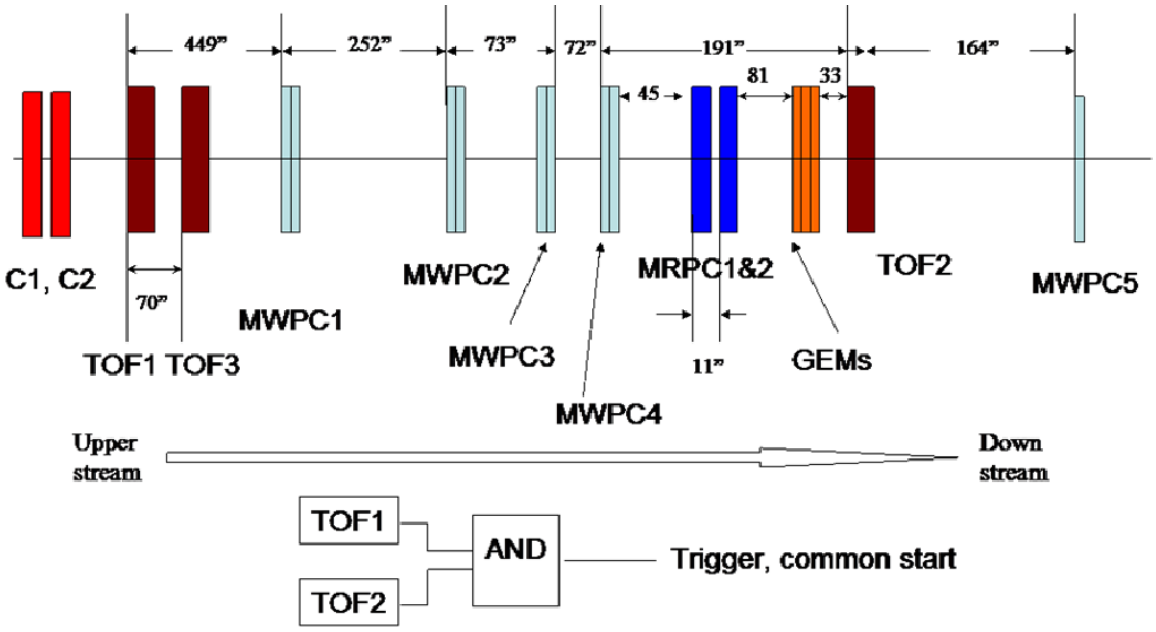

Figure 6.16: Experiment setup of the Long-MRPC beam test at FNAL.

A comprehensive series of performance tests on the two modules under various working conditions were carried out. The details of these tests can be found in Table 6.3.

Firstly, a high voltage scan was done to find the optimal working high voltage for two modules, where they reach their efficiency plateau and operate stably. Then the

Type of test	Test parameters
HV scan	6.1-7.6 kV for Tsinghua module 5.4-6.9 kV for USTC module
Position scan	X: 250-760 mm; Y: 50-210 mm
Beam energy scan	4, 8, 16, 32, 120 GeV
Gas composition scan	5% Iso-butane, 7% SF6 Mix (0-5% Iso-butane vs. 0-7% SF6)
Incident angle scan	0°, 15°, 30°
Absorber	with(out) 1.5 m iron absorber
Cherenkov PID scan	C1: 0.2-17.0; C2: 0.1-6.0 selecting protons from other particles

Table 6.3: Performance tests on two Long-MRPC modules at FNAL.

efficiency, timing and spatial resolutions as a function of high voltage, beam incident position, beam energy, working gas, and beam incident angle are calculated and studied. Moving the absorber in stops most of the particles except muons, allowing us the study the response of Long-MRPC modules to muons. The Cherenkov detectors are able to identify particles according to their velocity, and we take advantage of this to further test the timing resolution of Long-MRPC modules.

6.2.3 Beam test results

As the most fundamental part, ADC and TDC signals of the two modules are shown in Figure 6.17. Since the width of the beam is only about 3.5 cm, for a specific run, only one strip out of six of the modules is largely exposed to the beam. In this figure, ADC and TDC from the third strip of the Tsinghua module, and the second strip of the USTC module are shown. To avoid any crosstalk between neighboring strips, the ADC is accepted only if it is maximum among the six strips.

Both modules have a well defined TDC signal peak, but the ADC distributions look somewhat abnormal. Both modules have a peak at very low ADC values (ADC<50 for the Tsinghua module and ADC<100 for the USTC module), but their TDC values are similar to signals with higher ADC. Changing the integrating time window for the ADC acquisition does not help to solve the problem. The electronics of the modules need to be re-investigated to address this issue. In addition, the

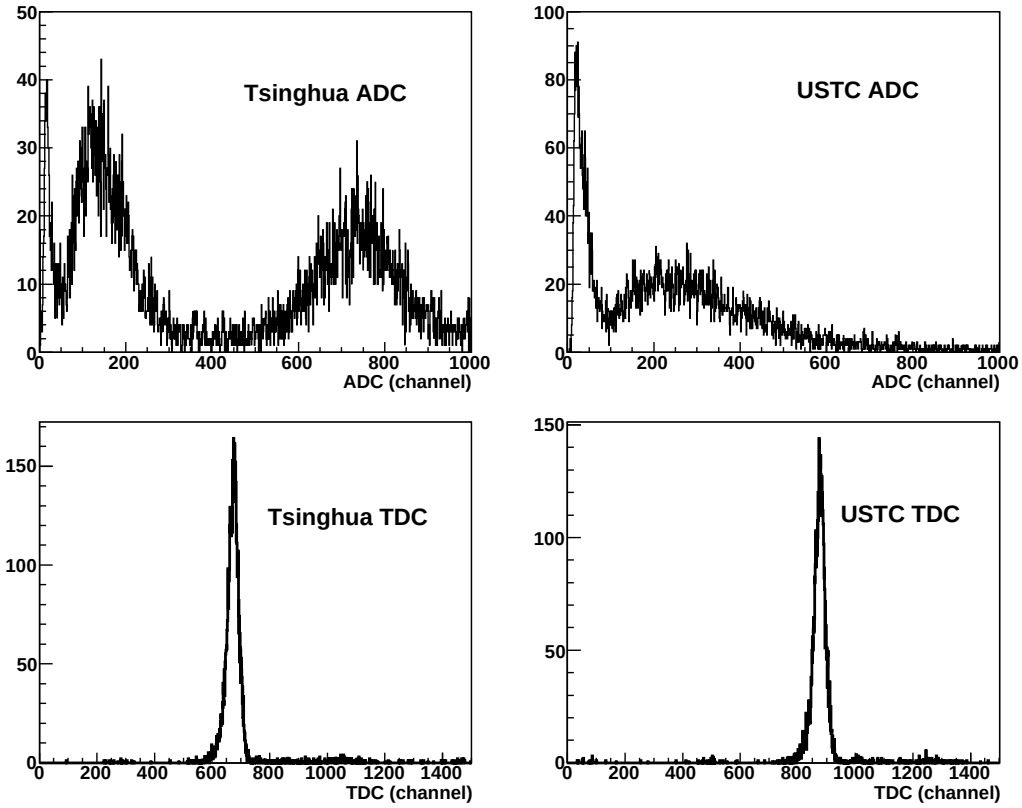

Figure 6.17: The ADC (upper panels) and TDC (lower panels) signal distributions from two Long-MRPC modules. For TDC it is 50 ps/channel.

ADC distribution for the Tsinghua module has a double broad peak structure at high ADC. The left peak represents the normal ADC signals, like the peak of the USTC module, while the right peak is believed to come from the streamer mode, in which a significantly larger amount of charges are generated. The streamer mode has worse timing resolution and is generally unwanted. This is possibly caused by a too high voltage used for the Tsinghua module to reach its efficiency plateau.

Interestingly, if we substitute 7% SF_6 for 5% Iso-butane as the working gas, the streamer mode of the Tsinghua module disappears. The ADC distribution of the Tsinghua module after using SF_6 is shown in Figure 6.18, though the peak at very low ADC values still exists. Changing the working gas does not affect the ADC distribution of the USTC module.

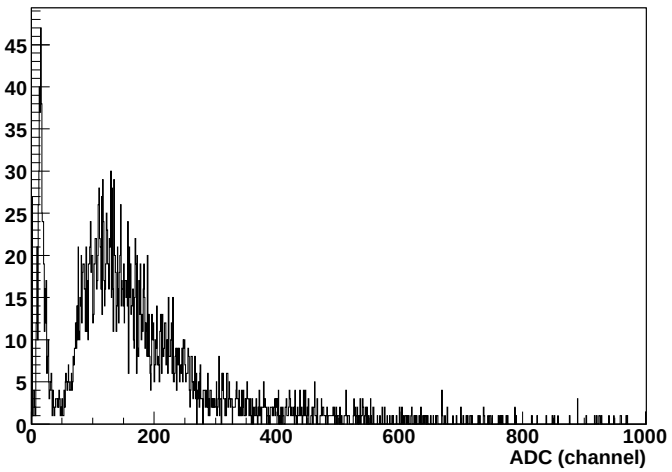

Figure 6.18: The ADC distribution of the Tsinghua module after using 7% SF_6 as working gas.

The efficiency as a function of high voltage, or strength of electric field ($E = HV/thickness$), for both modules is shown in Figure 6.19. To calculate the efficiency, the number of events recorded by a Long-MRPC module is divided by the number of triggered events. Either events triggered by the scintillators of TOF1+TOF2 or by the other Long-MRPC module can serve as the denominator.

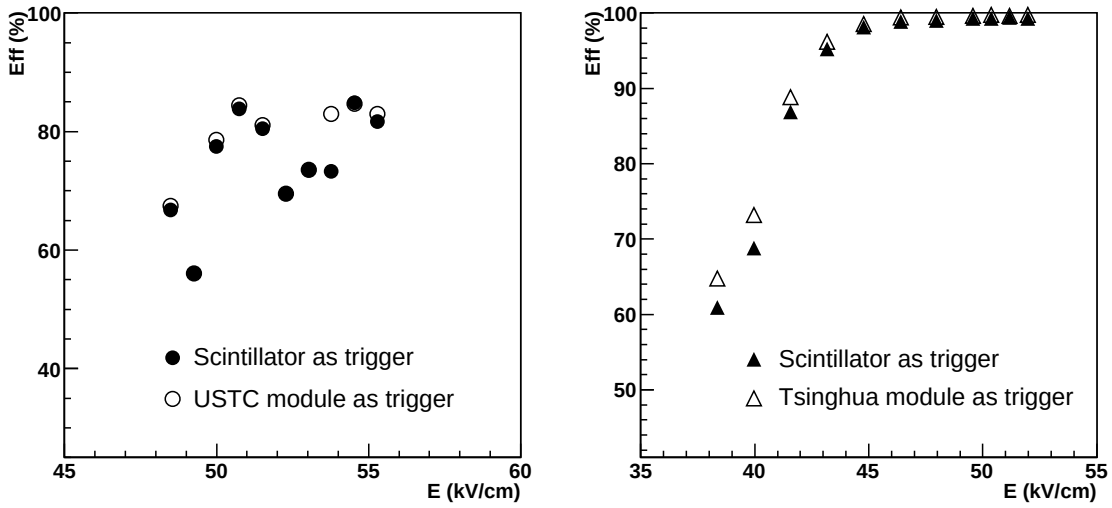

Figure 6.19: The efficiency of two Long-MRPC modules as a function of strength of electric field inside the modules. Both trigger methods using the scintillator and the other module are used.

We can see that the two trigger methods give consistent efficiency for both modules. The USTC module reaches a nearly perfect efficiency above 45 kV/cm, which corresponds to about 6.3 kV in high voltage. In contrast, the Tsinghua module appears to reach a efficiency plateau of ∼85% above 50 kV/cm (corresponding to about 7.3 kV in high voltage), but the efficiency is less stable and not as high as the USTC module. As a result, a high voltage of 7.3 kV for the Tsinghua module, and 6.3 kV for the USTC module are used as working high voltage later on. As seen in Figure 6.17, 7.3 kV seems a bit too high for the Tsinghua module and creates the streamer mode.

The timing resolution is calculated by fitting the distribution of

$$TOF_{strip} \equiv \frac{(MRPC\_TDC1 + MRPC\_TDC2) - (TOF3\_TDC1 + TOF3\_TDC2)}{2} \tag{6.1}$$

where $MRPC\_TDC1$ and $MRPC\_TDC2$ are TDCs from two end of a Long-MRPC strip; while $TOF3\_TDC1$ and $TOF3\_TDC2$ are TDCs from TOF3 serving as the starting time. For the Tsinghua module, only signals from the avalanche mode are

used. The ADC-TDC slewing effect, in which small magnitude of ADC delays the TDC, is corrected by fitting the ADC-TDC relation of $TDC = SL(ADC)$. Then an additional term of $SL(ADC)$ is subtracted from TOF_{strip} for the fitting to extract the timing resolution. Since the length of a Long-MRPC strip is fixed, $(MRPC\_TDC1 + MRPC\_TDC2)$ includes a constant time during which the particle travels from the TOF3 to the Long-MRPC module and the signal travels along the the whole strip, and it does not depend on the beam incident position. So minus the starting time and slewing correction, the distribution should reflect the sum of timing resolution from the Long-MRPC module, starting time, and other electronic jitter. The starting time resolution is obtained independently by fitting the distribution of $(TOF3\_TDC1 + TOF3\_TDC2)/2$, and is about 85 ps. Other effects such as FAN IN/OUT jitter contribute to the electronic jitter of about 30 ps. With their contributions subtracted, the timing resolution of both modules as a function of strength of electric field is shown in Figure 6.20. Both modules reach a timing resolution plateau of 60-70 ps at their working high voltage. At lower voltages the timing resolution is significantly worse for the USTC module. This resolution is consistent with the cosmic ray test, and it satisfies the requirement of the MTD.

Both the MWPC and GEM chamber can provide precise beam position information, from which we can calculate the signal propagating velocity and spatial resolution of the Long-MRPC modules. Figure 6.21 shows the correlation between the Long-MRPC two-end TDC difference (ΔTDC) and the beam position from the GEM chamber and MWPC. Both figures show clear linear correlations between the Long-MRPC module and GEM chamber/MWPC. The different signs of slope are due to the opposite definition of the horizontal axis for the GEM chamber and MWPC.

The 2-D correlation histograms are sliced along the x axis into multiple 1-D histograms, each representing the ΔTDC distribution at a specific incident position. These 1-D histograms are fit using a gaussian function, and their peak positions along with their corresponding incident positions are drawn in Figure 6.22 and fit using a linear function. Given that the unit of the ΔTDC is ps and the beam position is cm, the slope of the fit is twice the signal propagating velocity. For the ΔTDC, it is 50 ps/channel, and for the GEM chamber, it is 0.0625 cm/channel. So fitting from

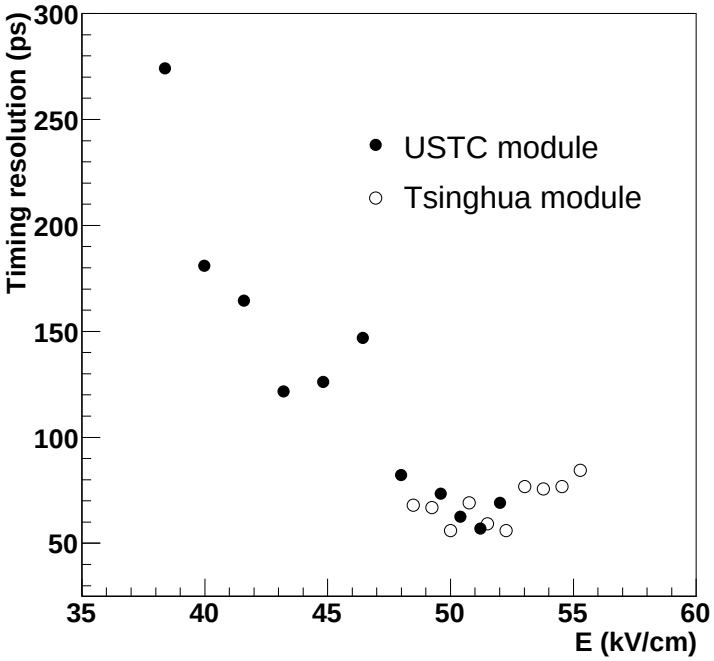

Figure 6.20: Timing resolution of both Long-MRPC modules as a function of strength of electric field.

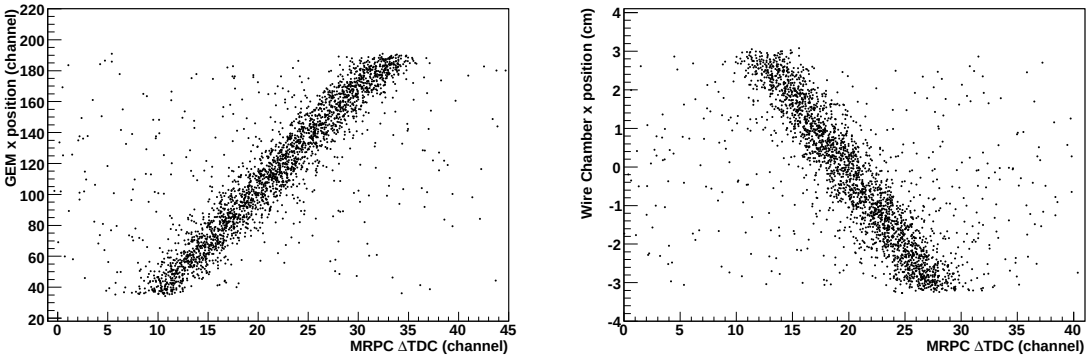

Figure 6.21: The correlation between the Long-MRPC two-end TDC difference and the beam position from the GEM chamber (left) and MWPC (right) for the Tsinghua module.

the GEM chamber gives a signal propagating velocity of 59.5 ps/cm, and fitting from the MWPC gives 63.2 ps/cm. Similar studies for the USTC module gives a velocity of 62.0 ps/cm from the GEM chamber, and 68.7 ps/cm from the MWPC. So results from two detectors are consistent, and they also agree with the cosmic ray test.

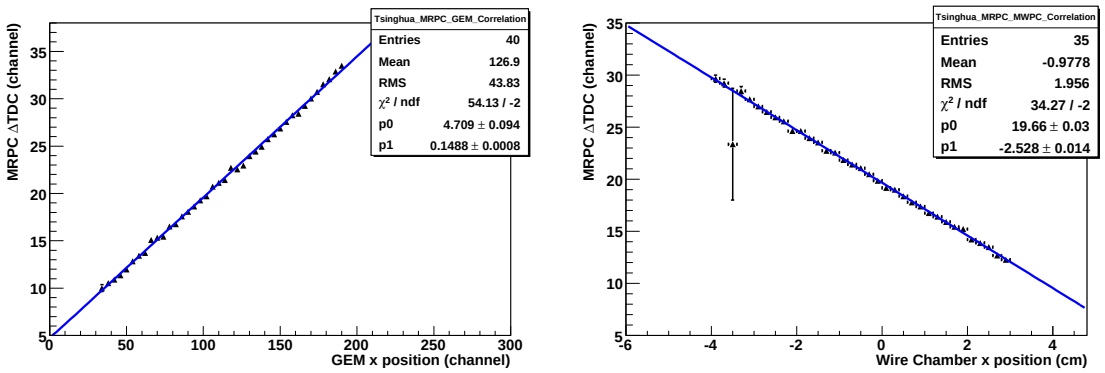

Figure 6.22: The correlation between the peak of Long-MRPC two-end TDC difference distribution and the beam position from the GEM chamber (left) and MWPC (right) for the Tsinghua module. The straight line is a linear fit.

Having the timing resolution of 60-70 ps and the signal propagating velocity of about 60 ps/cm, we expect that the spatial resolution of the Long-MRPC modules is about 1 cm. A direct measurement is done by comparing the position calculated from the ΔTDC ($\frac{\Delta TDC \times 50(ps/ch)}{2 \times 60(ps/cm)}$) and the position given by the GEM chamber or MWPC. Figure 6.23 shows the distributions of their difference and a gaussian fitting result. Here a signal propagating velocity of 60 ps/cm is used. Because the position resolutions of the GEM chamber and MWPC are much better than the Long-MRPC, any broadening of the distribution is due to the spatial resolution of the Long-MRPC. It indicates that the spatial resolution of the Tsinghua module is roughly 0.65 cm. What's presented here is the third strip of the Tsinghua module. Study of other strips shows a spatial resolution of 0.65-0.8 cm. A similar procedure indicates that the spatial resolution of the USTC module is 0.9-1.0 cm.

We also implement another method to calculate the spatial resolution. For a fixed beam incident position provided by the GEM chamber or MWPC (with bin width significantly smaller than the Long-MRPC spatial resolution), a distribution of the

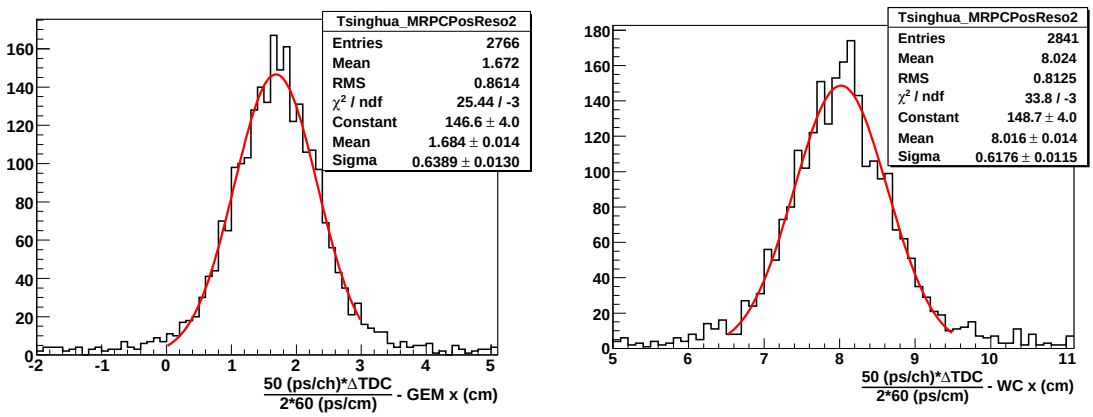

Figure 6.23: The distribution of the difference between the beam position calculated from the ΔTDC of the Long-MRPC and the position given by the GEM chamber (left) and the MWPC (right) for the Tsinghua module. The curve is a gaussian fitting.

Long-MRPC ΔTDC is drawn and fitted using a gaussian function. The width of the gaussian fit as a function of beam incident position is drawn in Figure 6.24, and it is fit to a constant number. The result of fitting indicates the averaged broadening of the ΔTDC, and the Long-MRPC spatial resolution is given by

$$\sigma_{Long-MRPC} = \frac{\sigma_{\Delta TDC} \times 50(ps/ch)}{2 \times 60(ps/cm)}. \tag{6.2}$$

The fitting in Figure 6.24 gives a resolution of 0.8-1.0 cm for the USTC module, which is consistent with results obtained from the earlier method. The situation is the same for the Tsinghua module. So both methods suggest that the Long-MRPC module has a spatial resolution of 0.6-1.0 cm, and it fits well for the requirement of the MTD.

The beam incident angle to the Long-MRPC can be adjusted, and it is interesting to test the sensitivity of the Long-MRPC to it. If we look at the correlation between the Long-MRPC and GEM chamber or MWPC, the slope of correlation should be changed for different incident angles, as demonstrated in Figure 6.25 for the USTC module. Here the actual incident angle is measured as 32.8°, and the slope increases as expected. The incident angle can be calculated as

$$\theta = \cos^{-1}(\frac{slope_{0^\circ}}{slope_{30^\circ}}), \tag{6.3}$$

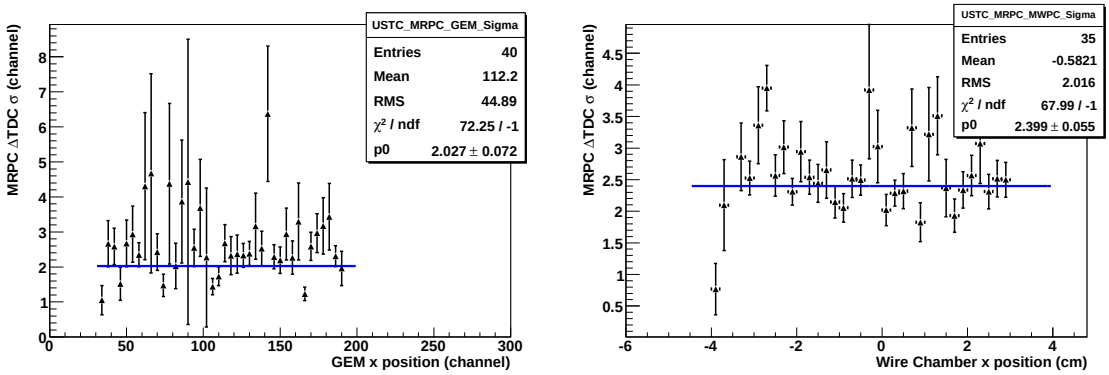

Figure 6.24: The width of ΔTDC distribution as a function of beam incident position provided by the GEM chamber (left), and the MWPC (right) for the USTC module. A constant number fit is shown as the solid lines.

which gives 35.9°, consistent with the actual value. The same analysis gives a result of 31.8° for the Tsinghua module.

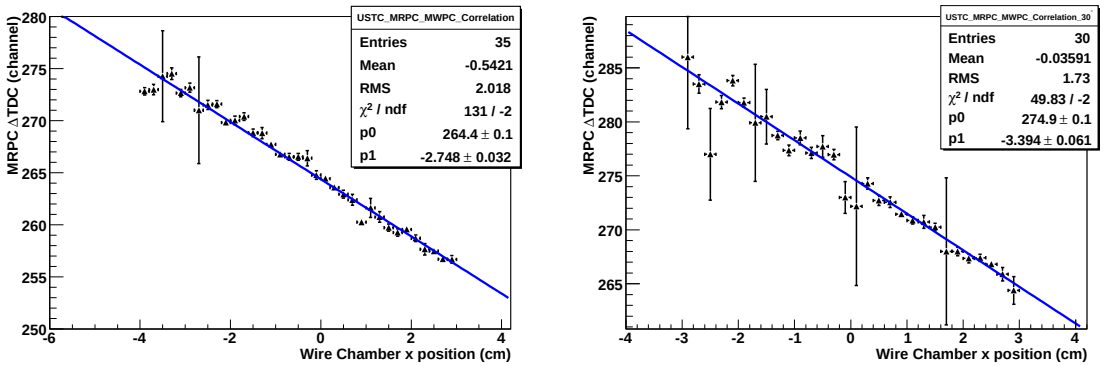

Figure 6.25: The correlation between the peak of Long-MRPC two-end TDC difference distribution and the beam position from the MWPC for the USTC module. The left panel is for incident angle of 0° and the right panel for 32.8°. The straight line is a linear fit to the data.

When the beam energy is decreased to 4 GeV, we are able to identify protons from the other particles using the Long-MRPC. Due to their heavier mass, protons have slightly smaller velocities and are expected to arrive at the Long-MRPC later than other particles by ∼2.5 ns, which is equivalent to 50 TDC channels. Having the Cherenkov detectors select samples with more protons, we draw the particle

TOF distributions from two Long-MRPC modules, as in Figure 6.26. The TOF is calculated as Equation 6.1. It is clearly seen that for both modules, a proton peak is separated from the bulk of particles. The distance between two peaks is roughly 45 channels, consistent with our expectation. Note that no slewing correction is undertaken here. It demonstrates that the Long-MRPC has good enough timing resolution to separate protons from other particles.

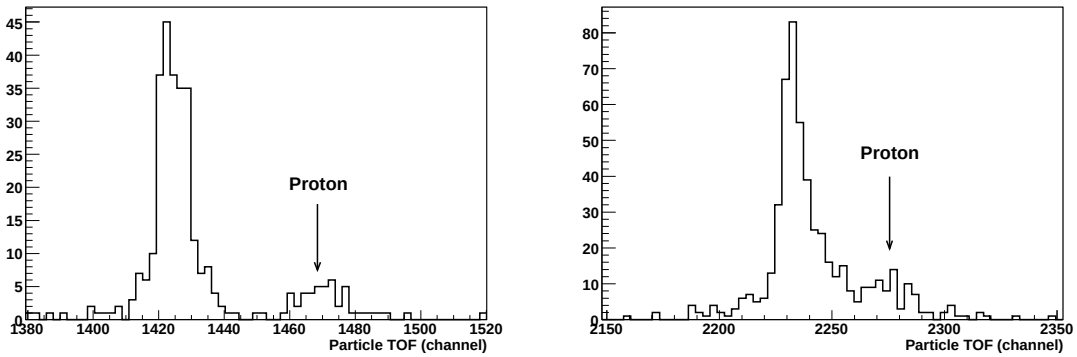

Figure 6.26: The time-of-flight distribution of proton rich sample for the Tsinghua (left) and USTC module (right).

6.2.4 Summary

In summary, the proposed muon detector performs very well in our simulations. The detection efficiency for muons within the MTD coverage reaches 80% at p_T >2 GeV/c, while the efficiency for hadrons is about 1%. Combined with the TPC and TOF, it is promising to achieve a hadron rejection factor of 150-300. Our simulations also demonstrate that the MTD can serve as an online muon trigger, rejecting background events to a di-muon trigger by a factor of 50.

The MTD utilizes the long strip, two end readout MRPC technology. Two Long-MRPC modules demonstrate that they have excellent timing resolution of 60-70 ps and spatial resolution of 0.6-1.0 cm in the beam test at FNAL. The results are consistent with the earlier cosmic ray test. They also perform well under other conditions such as different beam incident angles, beam energies, and working gases.

Two Long-MRPC modules were installed in STAR as a test and collected p+p and Au+Au data in year 2006 and 2007 RHIC run, respectively. Two more modules were added for the 2008 RHIC run. A MTD trigger was successfully implemented, requiring valid hits on the Long-MRPC modules. Preliminary studies of the MTD triggered data have shown promising results [88] for using the MTD for muon and high p_T hadron selection. We expect more comprehensive results from both the beam test and RHIC experiments to be presented in future publications.

Bibliography

[1] M. Peskin and D. Schroeder, An Introduction To Quantum Field Theory (Westview Press), 1995.

[2] R. Gupta, hep-lat/9807028.

[3] D. Gross and F. Wilczek, Phys. Rev. Lett. **30**, 1343 (1973); H. Politzer, Phys. Rev. Lett. **30**, 1346 (1973).

[4] S. Bethke, hep-ex/0211012.

[5] P. Braun-Munzinger, Nucl. Phys. A **681**, 119 (2001); F. Karsch, Nucl. Phys. A **698**, 199 (2002).

[6] J. Adams *et al.*, Nucl. Phys. A **757**, 102 (2005).

[7] F. Karsch, hep-lat/0601013.

[8] M. Harrison, T. Ludlam, and S. Ozaki, Nucl. Instrum. Methods A **499**, 235 (2003).

[9] M. Price, Nucl. Instrum. Methods A **478**, 46 (2002).

[10] M. L. Miller *et al.*, Ann. Rev. Nucl. Part. Sci. **57**, 205 (2007).

[11] D. Kharzeev *et al.*, Z. Phys. C **74**, 307 (1997).

[12] J. Adams *et al.*, nucl-ex/0311017.

[13] J. Adams *et al.*, Phys. Rev. Lett. **91** 072304 (2003).

[14] C. Y. Wong, Introduction to High-Energy Heavy-Ion Collisions (World Scientific Pub. Co. Inc.), 1994.

[15] B. I. Abelev *et al.*, Phys. Lett. B **655**, 104 (2007).

[16] S. S. Adler *et al.*, Phys. Rev. C **76**, 034904 (2007).

[17] M. Gyulassy *et al.*, Nucl. Phys. B **571**, 197 (2000); Phys. Rev. Lett. **85**, 5535 (2000); Nucl. Phys. B **594**, 371 (2001).

[18] U. A. Wiedemann, Nucl. Phys. B **588**, 303 (2000); C. A. Salgado and U. A. Wiedemann, Phys. Rev. D **68** 014008 (2003); N. Armesto *et al.*, Phys. Rev. D **69** 114003 (2004).

[19] P. Arnold *et al.*, JHEP **0206**, 030 (2002); S. Jeon and G. D. Moore, Phys. Rev. C **71**, 034901 (2005); S. Turbide *et al.*, Phys. Rev. C **72**, 014906 (2005).

[20] X. F. Guo and X. N. Wang, Phys. Rev. Lett. **85**, 3591 (2000); Nucl. Phys. A **696**, 788 (2001); B. W. Zhang and X.-N. Wang, Nucl. Phys. A **720**, 429 (2003); A. Majumder et. al., Phys. Rev. Lett. **99**, 152301 (2007).

[21] C. Adler *et al.*, Phys. Rev. Lett. **90**, 082302 (2003).

[22] C. Adler *et al.*, Phys. Rev. Lett. **89**, 202301 (2002).

[23] S. Eidelman *et al.*, Phys. Lett. B **592**, 315 (2004).

[24] S. Turbide, R. Rapp, and C. Gale, Phys. Rev. C **69**, 014903 (2004).

[25] R. J. Fries, B. Müller, and D. K. Srivastava, Phys. Rev. Lett. **90**, 132301 (2003); S. Turbide, C. Gale, S. Jeon, and G. D. Moore, Phys. Rev. C **72**, 014906 (2005).

[26] S. S. Adler *et al.*, Phys. Rev. Lett. **94**, 232301 (2005).

[27] R. Hanbury-Brown and R. Q. Twiss, Philos. Mag. **45**, 663 (1954).

[28] F. M. Marques *et al.*, Phys. Rept. **284**, 91 (1997).

[29] D. Peressounko, Phys. Rev. C **67**, 014905 (2003).

[30] C. Slotta and U. Heinz, Phys. Lett. B **391**, 469 (1997).

[31] S. Pratt, Phys. Rev. Lett. **53**, 1219 (1984); G. F. Bertsch, M. Gong, M. Tohyama, Phys. Rev. C **37**, 1896 (1988).

[32] U. Heinz and B. V. Jacak, Ann. Rev. Nucl. Part. Sci. **49** 529 (1999).

[33] J. Adams *et al.*, Phys. Rev. C **71**, 044906 (2005); Phys. Rev. Lett. **91**, 262302 (2003); S. S. Adler *et al.*, Phys. Rev. Lett. **93**, 152302 (2004).

[34] M. M. Aggarwal *et al.*, Phys. Rev. Lett. **93**, 022301 (2004).

[35] D. Peressounko, in Proceedings of Quark Matter 2006, arXiv:0704.0852v1.

[36] A. M. Poskanzer and S. A. Voloshin, Phys. Rev. C **58**, 1671 (1998).

[37] C. Adler *et al.*, Phys. Rev. C **66**, 034904 (2002).

[38] B. I. Abelev *et al.*, Phys. Rev. C **77**, 054901 (2008).

[39] N. Borghini, P. M. Dinh, and J.-Y. Ollitrault, Phys. Rev. C **64**, 054901 (2001).

[40] R. S. Bhalerao, N. Borghini, and J.-Y. Ollitrault, Phys. Lett. B **580**, 157 (2004).

[41] J. Adams *et al.*, Phys. Rev. C **72**, 014904 (2005); S. S. Adler *et al.*, Phys. Rev. Lett. **91**, 182301 (2003).

[42] P. Huovinen, P. F. Kolb, U. W. Heinz, P. V. Ruuskanen, and S. A. Voloshin, Phys. Lett. B **503**, 58 (2001); P. F. Kolb and U. Heinz, nucl-th/0305084.

[43] D. Molnar and S. A. Voloshin, Phys. Rev. Lett. **91**, 092301 (2003).

[44] P. Arnold, G. D. Moore, and L.G. Yaffe, J. High Energy Phys. **0112**, 009 (2001).

[45] S. Turbide, C. Gale, and R. J. Fries, Phys. Rev. Lett. **96**, 032303 (2006).

[46] R. Chatterjee, E. S. Frodermann, U. Heinz, and D. K. Srivastava, Phys. Rev. Lett. **96**, 202302 (2006).

[47] K. MIKI, in Presentation of Quark Matter 2008; M. J. Tannenbaum, arXiv:0707.1706.

[48] R. Rapp and J. Wambach, Adv. Nucl. Phys. **25** 1 (2000).

[49] B. Alessandro *et al.*, Eur. Phys. J. C **39**, 335 (2005).

[50] G. Ascoli *et al.*, Nucl. Instrum. Methods A **268**, 33 (1988); V. M. Abazov *et al.*, Nucl. Instrum. Methods A **565**, 463 (2006); H. Akikawa *et al.*, Nucl. Instrum. Methods A **499**, 537 (2003).

[51] S. S. Adler *et al.*, Phys. Rev. D **76**, 092002 (2007).

[52] A. Adare *et al.*, Phys. Rev. Lett. **98**, 232002 (2007); **98**, 232301 (2007); arXiv:0801.0220.

[53] B. I. Abelev *et al.*, arXiv:0805.0364.

[54] H. Hahn *et al.*, Nucl. Instrum. Methods A **499**, 245 (2003).

[55] P. Jacobs and X.-N. Wang, Prog. Part. Nucl. Phys. **54**, 443 (2005).

[56] K. H. Ackermann *et al.*, Nucl. Instrum. Methods A **499**, 624 (2003).

[57] J. Wu and M. Xu, J. Phys. G **34**, S729 (2007).

[58] M. Shao *et al.*, Nucl. Instrum. Methods A **558**, 419 (2006).

[59] W.-M. Yao *et al.*, J. Phys. G **33**, 1 (2006).

[60] C. A. Whitten, AIP Conf. Proc. **980**, 390 (2008).

[61] STAR Trigger Definitions, STAR Internal Documents.

[62] X.-N. Wang and M. Gyulassy, Comput. Phys. Commun. **83**, 307 (1994).

[63] Private Communication with A. Chikanian.

[64] A. Wetzler, Ph.D. thesis, Lawrence Berkeley National Laboratory, 2006.

[65] I. Johnson, Ph.D. thesis, University of California, Davis, 2002

[66] J. Adams *et al.*, Phys. Rev. C **70**, 044902 (2004).

[67] D. LHote, Nucl. Instrum. Methods Phys. Res. A **337**, 544 (1994); D. Drijard, H. G. Fischer, and T. Nakada, Nucl. Instrum. Methods Phys. Res. A **225**, 367 (1984).

[68] P. Nevski, in Proceedings of the International Conference on Computing in High Energy and Nuclear Physics, Padova, Italy, 2000.

[69] PDSF web page at http://www.nersc.gov/nusers/systems/PDSF/.

[70] B. B. Back *et al.*, Phys. Rev. Lett. **91**, 052303 (2003).

[71] B. I. Abelev *et al.*, Phys. Rev. Lett. **97**, 152301 (2006).

[72] I. Vitev, Phys. Lett. **B639**, 38 (2006).

[73] B. I. Abelev *et al.*, to be published; F. Simon, AIP Conf. Proc. **915**, 343 (2007).

[74] I. Vitev and M. Gyulassy, Phys. Rev. Lett. **89**, 252301 (2002).

[75] A. Dainese, C. Loizides, and G. Paic, Eur. Phys. J. C **38**, 461 (2005); C. Loizides, Eur. Phys. J. C **49**, 339 (2007).

[76] B. I. Abelev *et al.*, Phys. Rev. Lett. **98**, 192301 (2007).

[77] J. Sandweiss, STAR Collaboration, Internal STAR analysis meeting 2005.

[78] A. Chikanian, E. Finch, R. Majka, and J. Sandweiss, photon converter proposal in STAR, http://hepwww.physics.yale.edu/star/converter-proposal.pdf

[79] C. Adler *et al.*, Phys. Rev. C **66**, 034904 (2002).

[80] J. Adams *et al.*, Phys. Rev. Lett. **93**, 252301 (2004).

[81] Private Communication with A. Hamed.

[82] M. Bourquin and J.-M. Gaillard, Nucl. Phys. B **114**, 334 (1976).

[83] S. S. Adler *et al.*, Phys. Rev. C **75**, 024909 (2007).

[84] Private Communication with Z. Xu.

[85] M. Anderson *et al.*, Nucl. Instrum. Methods A **499**, 659 (2003).

[86] D. Acosta *et al.*, Phys. Rev. Lett. **88**, 161802 (2002); F. Abe *et al.*, Phys. Rev. Lett. **75**, 4358 (1995).

[87] Y. J. Sun *et al.*, Nucl. Instrum. Methods A **593**, 307 (2008).

[88] L. J. Ruan *et al.*, to be submitted to Nucl. Instrum. Methods A.